

Charge transport properties of spin-orbit coupled materials in different correlation regimes

THIS IS A TEMPORARY TITLE PAGE

It will be replaced for the final print by a version
provided by the service academique.



Thèse n. 1234 2011
présenté le 12 Mars 2018
à la Faculté des Sciences de Base
laboratoire SuperScience
programme doctoral en SuperScience
École Polytechnique Fédérale de Lausanne
pour l'obtention du grade de Docteur ès Sciences
par

Soudabeh Mashhadi

acceptée sur proposition du jury:

Prof Name Surname, président du jury
Prof Name Surname, directeur de thèse
Prof Name Surname, rapporteur
Prof Name Surname, rapporteur
Prof Name Surname, rapporteur

Lausanne, EPFL, 2018

Acknowledgements

I am very grateful to my thesis advisor Prof. Klaus Kern, for giving me the possibility to work in his group and for his continuous support throughout my PhD studies.

I am grateful to Dr. Marko Burghard for his help and scientific input. I would like to thank my (former) group members, Pascal Gehring, Roberto Urcuyo, Loc Duong, Kristina Vaklinova and Junhong Na for their help and support.

Finally, I thank the Nanostructuring Lab team, Ulli, Thomas, Achim and Marion for their help in sample fabrication and process development and also appreciate the technical support I received from Wolfgang Stiepany and Marko Memmler.

Abstract

From recent advances in solid state physics, a novel material classification scheme has evolved which is based on the concept of topology and provides an understanding of different phenomena ranging from quantum transport to unusual flavors of superconductivity. Spin-orbit coupling is a major term in defining the topology of materials, and its interplay with electron-electron correlations yields novel, intriguing phenomena. In the weak to intermediate correlation regime, spin-orbital entanglement leads to the emergence of topological insulators, which constitute Dirac materials with two dimensional spin-polarized helical edge or surface states and an insulating bulk. The concept of topology has led to a more general view of phenomena which previously seemed unrelated. In the specific case of topological insulators, theory predicts that their unique band structure leads to a high thermoelectric performance, which is of practical relevance for energy conversion applications.

In the strong correlation regime, the spin-orbit coupling removes the orbital degeneracy, thereby enhancing quantum fluctuations of the spin-orbit entangled states. This in turn can lead to the emergence of novel phases such as quantum spin liquids and unconventional superconductivity. The Kitaev quantum spin liquid (QSL) is a topological state of matter that exhibits fractionalized excitations in the form of Majorana fermions. The fractionalization refers to the ability to describe the electrons as two well-defined independent quasiparticles. The exotic Majorana particles may find future applications in robust quantum computation. The main aim of this thesis was to study these novel states of matter in the form of two different materials that fall in the weak and strong correlation regime, respectively. On this basis, it should furthermore be explored whether benefit can be taken of their properties by combining them with other quantum materials into heterostructures.

In the first part of this thesis, nanoplatelets of bismuth chalcogenide-based 3D topological insulators were grown by chemical vapor deposition, and characterized by magnetotransport experiments. Having established charge transport characteristics of the single components, in the aim to exploit their high thermoelectric efficiency, the lateral heterostructures of them are fabricated. Their investigation by scanning photocurrent microscopy revealed strong

photocurrent generation at the p-n junction, which could be explained by heating effects due to the laser illumination. The obtained results demonstrate that such type of hybrid heterostructure is a promising route to enhance the thermoelectric performance in nanostructured devices.

In the second part of this thesis, the Kitaev spin liquid candidate, α -RuCl₃, a spin-orbit coupled material in the strong correlation regime, was studied. Raman spectroscopy on exfoliated α -RuCl₃ revealed a broad magnetic continuum at low energies which according to its particular deviation from bosonic character is assigned to the fractionalized excitations. Furthermore, in complementary charge transport experiments, it was found that the magnetic fluctuations and structural changes in this material are highly entangled, and influence the emergence of the fractionalized excitations.

Finally, it was investigated whether the magnetic insulator character of α -RuCl₃ can be exploited to alter the graphene band structure through a proximity effect in vertical graphene/ α -RuCl₃ heterostructures. Measurements of their low-temperature, nonlocal resistance confirmed the possibility to induce pure spin currents in this manner. At the same time, the charge transport through the graphene served as a probe of the magnetic ordering in α -RuCl₃, although the complex magnetic behavior in this material necessitates further experimental and theoretical studies.

Key words: Spin-orbit coupling, electron-electron correlations, topological insulators, Kitaev spin liquid, photothermoelectricity, fractionalized excitations, Mott insulator, van der Waals heterostructures.

Zusammenfassung

In dieser Doktorarbeit wurden zwei Arten von Materialien mit starker Spin-Bahn-Kopplung untersucht. Dabei handelte es sich zum einen um dreidimensionale (3D) topologische Isolatoren, die in das schwache Korrelationsregime fallen, und zum anderen um den magnetischen Isolator α - RuCl_3 , der sich im starken Korrelationsregime befindet. Die starke Spin-Bahn-Kopplung in topologischen Isolatoren als ein Beispiel für Dirac-Materialien führt zur Bildung von topologisch geschützten Oberflächen- oder Randzuständen. Die unterdrückte Rückstreuung von Ladungsträgern in diesen Zuständen macht solche Materialien vielversprechend für neuartige Anwendungen in der Spinelektronik. Dazu gehören faszinierende Perspektiven für die Optospinelektronik, da mittels zirkular polarisiertem Licht Spin-polarisierte Ströme in topologischen Isolatoren erzeugt werden können. Letztere sind darüber hinaus aufgrund ihrer besonderen Bandstruktur von großem Interesse für thermoelektrische Anwendungen. Bismutchalkogenid-basierte 3D topologische Isolatoren gehören zu den effektivsten thermoelektrischen Materialien, im Zusammenhang mit beispielsweise Graphen, in welchem unter optischer Anregung die elektronische Temperatur über der des Gitters liegt, wodurch es für die Erzeugung heißer Ladungsträger z.B. im Rahmen der Thermoelektrik in Betracht kommt.

Im schwachen Korrelationsregime haben Materialien wie das α - RuCl_3 Interesse auf sich gezogen, insbesondere aufgrund ihrer niederenergetischen Anregungen wie zum Beispiel den ladungsfreien, auf Spin-Fraktionalisierung beruhenden Spinonen. α - RuCl_3 ist besonders attraktiv in diesem Zusammenhang, da sein auf dem hexagonalen Gitter basiertes Kitaev-Modell exakt lösbar ist und somit die eingehende Untersuchung von topologischen Spinflüssigkeiten und fraktionalen Quasipartikeln gestattet. Von quantisierten Spinflüssigkeiten wird zudem vermutet, dass sie eine wichtige Rolle in der Hochtemperatur-Supraleitung einnehmen. Der Einbau dünner Schichten aus solchen Materialien in van der Waals-Heterostrukturen könnte ferner zur Untersuchung neuartiger Kopplungsphänomene an den Grenzflächen dienen.

Der erste Teil dieser Arbeit beschäftigte sich mit der Herstellung und Charakterisierung von Nanoplättchen aus $\text{Bi}_2\text{Te}_2\text{Se}$ (BTS) als n-dotiertem bzw. Sb_2Te_3 als p-dotiertem dreidimensionalen topologischen Isolator. Basierend auf ihrem erfolgreichen CVD Wachstum wurden einzelne BTS und Sb_2Te_3 Nanoplättchen insbesondere auf ihre Magnetotransporteigenschaften hin untersucht. Für das zusätzliche Ziel, eine hohe Ladungsträgermobilität und verringerte

Ladungsträgerkonzentration im Volumen zu erreichen, wurden die beiden Verbindungen auf hBN Nanoschichten anstatt auf der Si/SiO₂ Oberfläche gewachsen.

Auf Basis obiger Resultate zu den Einzelkomponenten-Bauelementen wurden dann auch Heterostrukturen aus BTS und Sb₂Te₃ untersucht. Da die thermoelektrische Charakteristik von Bauelementen durch die thermoelektrische Kraft ihrer Komponenten bestimmt ist, kommt der Entwicklung und dem Einbau von weiter entwickelten Materialien eine wichtige Bedeutung zu. Hierfür wurden laterale BTS/Sb₂Te₃ Heterostrukturen gewachsen, wobei die CVD Wachstumsparameter gezielt eingestellt wurden, um die relativen lateralen Abmessungen sowie Schichtdicken zu kontrollieren. Das kontrollierte Wachstum der lateralen Heterostrukturen aus topologischen Isolatoren ermöglichte es, die thermoelektrischen Eigenschaften der Bauelemente einzustellen. In Untersuchungen des elektrischen Verhaltens unter Lichteinfluss mittels Rasterphotostrommikroskopie wurden ausgeprägte Photoströme in der Größenordnung von mehreren hundert μA gefunden. Die Größe dieses Signals übertrifft dasjenige von elektrostatisch definierten, lateralen p-n Übergängen in Graphen um ca. drei Größenordnungen. Zudem zeigen die lateralen Heterostrukturen aus topologischen Isolatoren ein verstärktes photothermoelektrisches Ansprechen mit Seebeck-Koeffizienten über 230 $\mu\text{V/K}$. Weitere Verbesserungen könnten durch das Wachstum verfeinerter Heterostrukturen auf hBN als Isolator, oder durch parallele Integration mehrerer solcher thermoelektrischen Bauelemente erzielt werden.

Der zweite Teil dieser Arbeit fokussierte auf die elektrischen Eigenschaften des Kitaev-Materials $\alpha\text{-RuCl}_3$. Theoretischen Studien zufolge sollte dieses aufgrund seiner ideal hexagonalen, zweidimensionalen (2D) Gitterstruktur Kitaev-Wechselwirkungen beinhalten. Überzeugende Belege für das Vorhandensein fraktionalisierter Anregungen in $\alpha\text{-RuCl}_3$ wurden zuvor durch Neutronenbeugung und Ramanspektroskopie erhalten. Im letzteren Fall handelt es sich um eine ungewöhnliche Temperaturabhängigkeit der Breite bestimmter Ramanmoden, welche sich vom konventionellen bosonischen Verhalten unterscheidet. Ein Ziel der vorliegenden Arbeit war es, dieses Phänomen in mechanisch exfoliierten, ultradünnen $\alpha\text{-RuCl}_3$ Schichten eingehend zu untersuchen. Die erhaltenen Ramanspektren beinhalteten dieselben Hinweise auf fraktionalisierte Anregungen, wie sie zuvor an makroskopischen Proben beobachtet wurden. Allerdings trat die Abweichung vom bosonischen Verhalten bereits bei etwas höheren Temperaturen in Erscheinung.

Weiterhin wurde eine zuverlässige Methode zur elektrischen Kontaktierung einzelner, ultradünner $\alpha\text{-RuCl}_3$ Schichten entwickelt, welche es ermöglichte, Änderungen in deren elektrischem Widerstand in Abhängigkeit der Temperatur zu detektieren. In Übereinstimmung mit der Theorie wurde das typische Verhalten eines Mott-Isolators beobachtet, wobei im Hüpfverhalten bei ungefähr derselben Temperatur eine Änderung auftrat, wie für das Einsetzen der Spin-Phonon Wechselwirkungen in den Ramanspektren. Diese Beobachtungen deuten auf die Verknüpfung von Kristallstruktur und Magnetismus im $\alpha\text{-RuCl}_3$ hin. Die verlässliche Kontaktierung dieses Materials eröffnet die Möglichkeit, es in nanostrukturierte Bauelemente einzubauen, um die zugrundeliegenden fraktionalisierten Spinon auszunutzen. Als weitere Perspektive könnte das Wechselspiel zwischen Spin-Bahn-Kopplung und elektronischer Korrelation Zugang zu einer ungewöhnlichen Art von Supraleitung in $\alpha\text{-RuCl}_3$

bieten. Diese Option wird gestützt durch die kürzlich beschriebene Beobachtung einer supraleitenden Phase in Sr_2RuO_4 , welches ebenfalls ein viel versprechender Kandidat für einen Spinflüssigkeit-Grundzustand ist. Für $\alpha\text{-RuCl}_3$ könnte dies durch Einstellen der Elektronenkorrelationslänge über den elektrostatischen Gate-Effekt erreicht werden. In zukünftigen Experimenten ließe sich eine ausreichend große Änderung der Ladungsträgerkonzentration mithilfe eines Polymerelektrolyt-Gates erzielen, um somit das $\alpha\text{-RuCl}_3$ in die Nähe des Spinflüssigkeit-Grundzustands zu bringen.

Die ultradünnen $\alpha\text{-RuCl}_3$ Schichten wurden schließlich mit Graphen kombiniert, um eine neue Art von vertikaler van der Waals Heterostruktur zu realisieren. Das Hauptziel bestand hierbei darin, festzustellen, ob eine magnetische Austauschwechselwirkung an der Grenzfläche zum Graphen erzeugt werden kann. Solch ein Effekt konnte tatsächlich in Magnetotransportuntersuchungen an einzelnen Graphen/ $\alpha\text{-RuCl}_3$ Heterostrukturen beobachtet werden. Er zeigt sich in der Erzeugung von Spinströmen selbst in Abwesenheit eines äußeren magnetischen Felds. Dieser Erfolg öffnet die Tür für neuartige spinelektronische Bauelemente, in welchen die Spinerzeugung auf rein elektrischem Weg erfolgt, ohne auf ein angelegtes Magnetfeld angewiesen zu sein. Eine weitere Motivation zur Untersuchung der Graphen/ $\alpha\text{-RuCl}_3$ Heterostrukturen bestand darin, über das Magnetotransportverhalten entsprechender Bauelemente Informationen über die Spinorientierung nicht im Volumen des $\alpha\text{-RuCl}_3$, sondern speziell an seiner 2D Oberfläche zu gewinnen. An Heterostrukturen bestehend aus entweder CVD-gewachsenem oder exfoliertem Graphen wurde beobachtet, dass die Stärke der magnetischen Austauschwechselwirkung sensitiv von der Qualität der Grenzfläche abhängt. Der Nachweis, dass der magnetische Isolator $\alpha\text{-RuCl}_3$ beachtliche Spineffekte in Graphen auszulösen vermag, schafft eine nützliche Grundlage für die Untersuchung eines ähnlichen Effekts in Kombination mit anderen 2D Quantenmaterialien. Eine hochinteressante Option für die Zukunft wäre es, eine starke Spin-Bahn-Kopplung über Graphen/ $\alpha\text{-RuCl}_3$ Grenzfläche zu erzeugen. Auf diese Weise könnte es gelingen, die extrem kleine Bandlücke im Graphen zu vergrößern, und somit seine eindimensionalen Randzustände robust zu machen. Die erfolgreiche Überführung von Graphen in einen robusten Quanten-Spin-Hall-Isolator würde weitreichende Perspektiven für Anwendungen in der Spinelektronik eröffnen.

Stichwörter: Spin-Bahn-Kopplung, Elektronenkorrelation, topologische Insulatoren, Kitaev Spinflüssigkeit, Photothermoelektrizität, Mott-Isolator, van der Waals Heterostrukturen.

Contents

Acknowledgements	i
Abstract (English/Deutsch)	ii
List of figures	ix
1 Introduction	1
Introduction	1
2 Theory of Topological Insulators	5
2.1 Topology and Band Theory	5
2.1.1 Topology	5
2.1.2 The Insulating State	6
2.1.3 Integer Quantum Hall Effect	6
2.2 Polarization and Charge Pump	8
2.3 Berry Phase and the Chern Number	11
2.3.1 Quantum Hall Effect and Band Theory	11
2.3.2 Edge States and Bulk Boundary Correspondence	12
2.3.3 Quantum Spin Hall Effect	14
2.4 3D Topological Insulators	14
2.4.1 Weak and Strong Topological Insulators	17
3 Kitaev Physics	19
3.1 Spin Orbit Assisted Mott Insulators	19
3.1.1 Bond-Directional Interactions	21
3.1.2 Kitaev-Heisenberg Model	22
3.1.3 Kitaev Honeycomb Model	22
3.1.4 Honeycomb Kitaev Materials	24
4 Experimental Techniques	26
4.1 Chemical Vapor Deposition	26
4.2 Growth of $\text{Bi}_2\text{Te}_2\text{Se}$ and Sb_2Te_3	28
4.3 Growth of Topological Insulator Heterostructures	29
4.4 Raman Spectroscopy	31

Contents

4.5	Scanning Photo Current Microscopy	32
4.6	Cryogenic Charge Transport Measurements	33
4.7	Atomic Force Microscopy	33
4.8	Kelvin Force Probe Microscopy	33
4.9	Nanostructure Patterning by E-beam Lithography	34
4.10	Electrical Measurement Geometries	35
4.11	Magnetoresistance Measurements	36
5	Electronic Transport Study of Topological Insulators	38
5.1	Growth of Single Component Topological Insulators	38
5.2	Magnetotransport of Single Component Topological Insulators	39
5.3	Magnetotransport of TIs Grown on hBN	40
5.3.1	Shubnikov-de Haas Oscillations	41
5.3.2	Magnetotransport of BTS on hBN	43
5.3.3	Magnetotransport of Lateral Heterojunctions	45
6	Scanning photocurrent microscopy of lateral TI heterostructures	47
6.1	Structural and Compositional Analysis	50
6.2	Electrical Characterization	52
6.3	Photothermoelectric Measurements	54
6.3.1	SPCM on Single Components	54
6.3.2	SPCM on TI Lateral Heterojunctions	55
7	Electronic and Magnetic Studies of α-RuCl₃	61
7.1	Background on α -RuCl ₃	61
7.1.1	Experimental Evidence	62
7.1.2	Structure and Magnetism	62
7.2	Inelastic Light Scattering of α -RuCl ₃ Nanosheets	63
7.2.1	Laser heating and substrate background	63
7.2.2	Temperature Evolution of the Raman Spectrum	65
7.3	Electrical Transport Measurements of α -RuCl ₃ Nanosheets	69
7.3.1	Contact resistance	69
7.3.2	Temperature Dependent Resistance Measurements	70
8	Interfacial Exchange Field in Graphene/α-RuCl₃ Heterostructures	74
8.1	Nonlocality Near Graphene's Dirac Point	76
8.1.1	Zeeman Spin Hall Effect in CVD Grown and Exfoliated Graphene	77
8.2	Magnetic Exchange Field	78
8.3	Graphene/ α -RuCl ₃ Heterostructures	79
9	Summary and Outlook	84
	Curriculum Vitae	97

List of Figures

1.1	Schematic diagram of electronic materials in dependence of the electron-electron correlation energy U/t and spin orbit coupling λ/t . The materials studied in this thesis belong to the right side of the phase diagram where spin orbit interaction is intermediate or strong. Figure from [1].	2
2.1	(a,d) Schematic of the insulating state and the corresponding band structure, respectively. (b,e) Schematic of the quantum Hall state and the corresponding band structure. The energy gap between the energy levels resembles that of a trivial insulator. (c) The electronic density of states in the presence of a magnetic field and scattering events. (f) Longitudinal and Hall resistance arising from such a density of states of electrons in a B-field.[2]	7
2.2	(a) A two dimensional cylinder threaded with a magnetic flux which can be changed adiabatically. The magnetic flux resembles the edge crystal momentum when the circumference has the same value as a single lattice constant. (b) The time reversal invariant fluxes $\Phi = 0$ and $\Phi = h/2e$ correspond to edge time reversal invariant momenta Λ_1 and Λ_2 . (Figure adapted from [3])	8
2.3	For a periodic or infinite lattice polarization can not be uniquely defined and it depends on the choice of the unit cell.	10
2.4	(a) The edge chiral mode at the interface of a quantum Hall state and a normal insulator. (b) Energy band diagram of the system showing the electronic structure of the semi infinite stripe described by Haldane.	13
2.5	(a) and (c) Interface between a QSHI and a normal insulator and schematic of the band diagram for the SHI.(b) Hall resistance for a HgTe/(Hg,Cd)Te quantum well at different gate voltages showing a transition from n-type to p-type by decreasing the gate voltage. The sample undergoes an insulating phase for $-1.9V < V_g < -1.4V$. (d) Experimental observation of the 2D QSHE in HgTe/(Hg,Cd)Te quantum wells. In the insulating regime in the presence of a small magnetic field samples III and IV show quantized conductance associated with edge states. (Adapted from König et al [4])	15
2.6	(a) Generalized cylinder in 3D can be visualized as a corbino donut, with two fluxes corresponding to the two components of the crystal surface momentum. (b) The four time reversal invariant fluxes Φ_1 and $\Phi_2 = 0, h/2e$ corresponding to four 2D surface momenta Λ_a	16

List of Figures

2.7	(a) ARPES intensity for Bi_2Se_3 as a function of energy and momentum revealing surface states with a single spin polarized Dirac cone. (b) The Fermi surface as a function of k_x and k_y showing a chiral spin texture.[5]	17
2.8	Fermi arcs in the surface Brillouin zone for (a) a weak topological insulator and (b) a strong topological insulator. (c) In the simplest form of a strong topological insulator the Fermi arc is a circle and encloses a single Dirac point.	18
3.1	(a) An illustration of the octahedral geometry of a transition metal. (b) Formation of t_{2g} and e_g orbitals in the presence of the crystal field. The t_{2g} state in the presence of spin orbit coupling splits into $j = 1/2$ and $j = 3/2$ states. In the presence of a strong electron-electron correlation such a $j = 1/2$ state is localized, leading to an insulating behavior. (c) The composition of the $j = 1/2$ states with spin up or down configuration as a result of the spin orbit coupling.	20
3.2	Illustration of possible geometric orientation of neighboring IrO_6 octahedra (a) corner sharing like Sr_2IrO_4 (b) edge sharing like Na_2IrO_4 , $\alpha - Li_2IrO_3$ and $\alpha - RuCl_3$. (c) parallel edge sharing.	21
3.3	(a) Kitaev interactions on the honeycomb lattice, the grey circles show the Ru^{+3} ions while the red ones indicate the position of Cl^{-1} ions. (b) Phase diagram of the Kitaev model. The phase diagram depicts a plane $K_x + K_y + K_z = c$ in which around the point of equal Kitaev exchange terms, a gapless spin liquid is formed.	23
3.4	Phase diagram of Kitaev Heisenberg model, parametrized as $J = \cos\phi$ and $K = \sin\phi$.	24
4.1	The schematic of the steps occurring in a CVD growth mechanism.	27
4.2	The schematic of the CVD set up. The cold trap serves merely as a trap for heavy elements for the protection of the pump.	28
4.3	(a) and (c) Atomic force microscopy image of two exemplary BTS flakes. (b) and (d) line profile across the white line in the AFM image showing the thickness of the nanoflakes.	29
4.4	(a,d) AFM image and the corresponding height profile across a Sb_2Te_3/Bi_2Te_2Se lateral heterostructure, (b,e) AFM image and height profile of another heterostructure with pronounced lateral growth, (c,f) AFM image and height profile of the same heterostructure as in panel (b) after dry Ar etching to better visualize the two components.	30
4.5	(a) The basic parts of a Raman spectroscopy system. (b) Schematic of Rayleigh and Raman scattering processes. m state indicated the vibrational ground state and n the first excited state.	31
4.6	Schematic of a scanning photocurrent microscopy set-up. The system is comprised of different laser lights and a piezo-electric stage used to scan the sample with confocal laser. The electronic set up is added to measure the generated photocurrent in the sample.	32
4.7	(a) Schematic of an AFM set up. (b) The diagram of the potential between the tip and the sample as a function of distance.	34

4.8	Working principle for a KFP measurement, (a) sample and tip are far away, (b) in contact and (c) the compensation DC voltage is applied.	35
4.9	electron beam lithography steps (a) spin coating the substrate (b) defining the electrode area using EBL and developing (c) evaporation of metals and (d) lift off of the metal evaporated.	36
4.10	(a) and (b) Two terminal configuration and its equivalent electrical circuit including the contact resistances, respectively. (c) and (d) four terminal configuration excluding the contact resistances and measures the resistance of the channel between the voltage electrodes.	36
4.11	(a) Hall bar geometry for measuring R_{xx} and R_{xy} , (b) Van der Pauw geometry for measuring R_{xx} and R_{xy} of a non geometric sample.	37
5.1	(a) and (d) AFM images (b) and (e) the height profile across the blue line in indicated in AFM image (c) and (f) the Raman spectrum taken using a 532 nm laser light at ambient conditions for typical BTS and Sb_2Te_3 nanosheets, respectively.	39
5.2	(a) and (d) Hall resistance (b) and (e) the relative magnetoresistance (c) and (f) $\Delta\sigma_{xx}$ vs magnetic fields for BTS and Sb_2Te_3 nanosheets respectively.	40
5.3	(a) Landau fan diagram, showing the energy levels for electrons in a magnetic field and (b) density of states for electrons in a magnetic field, broadened in the presence of the scattering centers.	42
5.4	(a) Sheet resistance of BTS/hBN nanosheet revealing prominent Shubnikov de Haas oscillations at $B = 10$ T, (b) the ΔR_{xx} vs inverse of the magnetic field indicating the periodic nature of this oscillation.	43
5.5	(a). The indices of magnetoresistance minima are plotted on the horizontal axis, the corresponding values of $1/B$ are plotted on the vertical axis. The slope of the line $2 e /hn$ determines the electron density. (b) Ando plot for different temperatures at 11 T, (c) the Dingle plot, yielding a quantum scattering time of 80 fs.	44
5.6	(a) Hall (R_{xy}) and (b) longitudinal (R_{xx}) resistance vs magnetic field of BTS/hBN nanoflakes for different gating values.	45
5.7	(a) Hall (R_{xy}) and (b) relative longitudinal $(R_{xx}(B) - R_{xx}(0))/R_{xx}(0)$ resistance vs. magnetic field of Sb_2Te_3 /hBN nanoflakes, showing a pronounced WAL cusp.	45
5.8	The magnetoresistance of the same heterostructure measured in two different electrode arrangements.	46
6.1	(a) and (b) schematic of photocurrent generation mechanism in a semiconductor junction and a thermoelectric material. (c) and (d) Schematic of simple devices working with photovoltaic and thermoelectric concepts respectively.	48

List of Figures

- 6.2 (a) Topographic AFM image of a lateral $\text{Bi}_2\text{Te}_2\text{Se}/\text{Sb}_2\text{Te}_3$ heterostructure, obtained by two consecutive vapor solid growth steps. The central $\text{Bi}_2\text{Te}_2\text{Se}$ nanoplatelet is surrounded by a significantly higher frame of Sb_2Te_3 . (b) Cross-sectional profile along the white line in the AFM image of panel a. (c) Overview TEM image of a $\text{Bi}_2\text{Te}_2\text{Se}/\text{Sb}_2\text{Te}_3$ nanoplatelet. (d) Corresponding EDX profiles for Sb, Bi, Te, and Se, taken across the $\text{Bi}_2\text{Te}_2\text{Se}/\text{Sb}_2\text{Te}_3$ interface along the white line in panel c. 50
- 6.3 (a) Raman map of a lateral $\text{BTS}/\text{Sb}_2\text{Te}_3$ heterostructure, displaying the scattered intensity at $\sim 71\text{ cm}^{-1}$ associated with the A_1g^1 mode of Sb_2Te_3 . (b) Raman spectrum recorded at the position marked in panel a, which lies within the Sb_2Te_3 region at the periphery. The blue line is the Lorentzian fit of the lowest energy peak. (c) Raman map of the same nanoplatelet as in panel a, displaying the scattered intensity at $\sim 65\text{ cm}^{-1}$ belonging to the A_1g^1 mode of $\text{Bi}_2\text{Te}_2\text{Se}$. (d) Raman spectrum collected from the center of $\text{Bi}_2\text{Te}_2\text{Se}$ region of the heterostructure (open circle). The blue line is a Lorentzian fit of the lowest energy peak. All of the above maps and spectra were acquired under ambient conditions with $\lambda = 514\text{ nm}$ 51
- 6.4 (a) Kelvin probe force microscopy image of the periphery of a $\text{Bi}_2\text{Te}_2\text{Se}/\text{Sb}_2\text{Te}_3$ nanoplatelet. The image was taken under ambient conditions. (b) Corresponding surface potential profile along the white line in panel a. The starting point belongs to the right end of the line. 52
- 6.5 (a) Current–voltage characteristics of a $\text{Bi}_2\text{Te}_2\text{Se}/\text{Sb}_2\text{Te}_3$ nanoplatelet at 1.4 and 290 K. The current was measured across the interface between the two components, using separate electrical contacts on the central $\text{Bi}_2\text{Te}_2\text{Se}$ region and the Sb_2Te_3 frame at the periphery. The inset shows the resistance of the same heterostructure nanoplatelet as a function of the magnetic field recorded at $T = 1.4\text{ K}$. The B-field is oriented perpendicular to the sample plane. 53
- 6.6 (a) Reflection image of the Sb_2Te_3 device (b) photocurrent map of the device using two electrodes (c) the photocurrent profile across the line line indicated in the PC map. 54
- 6.7 (a) Reflection image of the BTS device (b) photocurrent map of the device using two electrodes (c) the photocurrent profile across the line line indicated in the PC map. 55
- 6.8 Schematic depiction of a scanning photocurrent microscopy (SPCM) measurement, where a confocal laser spot is scanned across a $\text{Bi}_2\text{Te}_2\text{Se}/\text{Sb}_2\text{Te}_3$ device. . 55
- 6.9 (a) SPCM map of a $\text{Bi}_2\text{Te}_2\text{Se}/\text{Sb}_2\text{Te}_3$ nanoplatelet device with separate contacts on the two different components. The inset shows an optical image of the device. The dashed lines are drawn based on the overlap of the reflection and photocurrent image. The map was recorded under ambient conditions using $\lambda = 514\text{ nm}$. (b,c) the PC line profile across the black line and the gray line, respectively. 56

6.10	(a) Current-voltage curves of $\text{Bi}_2\text{Te}_2\text{Se}/\text{Sb}_2\text{Te}_3$ nanoplatelets, acquired in the dark (black curve) and under laser illumination ($\lambda = 514\text{nm}$) of the interfacial region (red curve). The curves were measured using Sb_2Te_3 as the drain contact. All measurements were performed under ambient conditions. The inset is a plot of photocurrent vs laser power ($\lambda = 514\text{nm}$) for local illumination of the p–n junction.	57
6.11	Sheet resistance of a BTS nanoribbon measured over a temperature range of 1.4 to 300 K. The red line is the fitting curve as described in the text.	59
6.12	(a) and (c) Density of states (b) and (d) Seebeck coefficient for Sb_2Te_3 and BTS.	60
7.1	(a) Schematic depiction of the in-plane $\alpha\text{-RuCl}_3$ crystal structure in C2/m space group symmetry, (b) ABAB stacking along the c direction, perpendicular to the honeycomb in-plane structure. The blue dashed lines indicate slight shift of the layers occurring after the orange dashed line. Figure adapted from [6]	62
7.2	(a) Raman spectra of a thin sheet (10 nm) of RuCl_3 measured using different laser powers, the table show the peak positions of the three Lorentzian peaks. b) Raman spectrum of the same nanosheet measured using $530\text{ }\mu\text{W}$ laser power at 70 K.	64
7.3	(a,b) Schematic depiction of the crystal structure of $\alpha\text{-RuCl}_3$ along the [010] and [001] direction respectively, (c) polarized Raman response of $\alpha\text{-RuCl}_3$ thin sheet , (d) detail of the low energy regime of the Raman spectrum, with the blue shading added to highlight the low energy background continuum.	65
7.4	(a) Comparison of the Raman spectra of $\alpha\text{-RuCl}_3$ bulk and a 10 nm thick nanoflake at high (bottom) and low (top) temperatures, (b) Temperature dependent Raman spectra of the nanoflake from 283 to 123 K.	65
7.5	(a) Raman spectrum and corresponding Fano function fit of the low energy range, (b) , (c) and (d) temperature evolution of the energy, linewidth and the Fano asymmetry parameter of the 20 meV peak, respectively.	67
7.6	Temperature dependent evolution of frequency and FWHM of the (a) 14 (b) 34 (c) 37 and (d) 38 meV Raman modes of $\alpha\text{-RuCl}_3$ nanoflake of 10 nm thickness with substrate subtraction.	68
7.7	Change of the integrated Raman intensity I_T relative to $I_{T=283\text{K}}$ of the E_g peaks at 14, 20, 33 and 36 meV as well as the A_{1g} peak at 38 meV in the nanoflake.	69
7.8	(a) AFM image of a typical device (b) height profile of the $\alpha\text{-RuCl}_3$ sheet in the device, (c) Resistivity ρ vs. T of a nanoflake with a thickness of 14 nm; the inset shows full temperature cycles for two different rates, (d) Semi-logarithmic plot of the resistivity ρ vs. $T^{-1/3}$ with linear fits (red lines) of a typical heating/cooling cycle, based on the VRH model.	70
8.1	(a) Honey comb lattice of graphene displaying zigzag and armchair edges. (b) lattice structure of graphene made out of two interpenetrating triangular lattices. (c) Electronic dispersion in graphene, the zoom shows the dispersion close to one of the Dirac points, (d) the corresponding Brillouin zone.	75

List of Figures

8.2	Spin Hall effect in graphene and nonlocal transport mediated by spin diffusion. (a) Schematic of the device configuration and flow of current with different spin orientation in two different directions, (b) Zeeman spin Hall effect lifts the spin degeneracy by producing two packets of electrons and holes with different spin orientations, (c) nonlocal resistance measured in graphene.	77
8.3	Comparison of SHE in CVD grown and exfoliated graphene. (a) Schematic of the device configuration, (b),(c) Nonlocal resistance in CVD and exfoliated graphene, respectively, in a magnetic field and in the absence of a magnetic field, (d) comparison of the nonlocal resistances.	78
8.4	(a) The nonlocal resistance of both CVD graphene and G/α -RuCl ₃ Hall bars at 27 K. The onset shows the device configuration for both Hall bars. (b) The nonlocal resistance in CVD graphene and G/α -RuCl ₃ at 1.3 K, below the RuCl ₃ magnetic transition temperature.	79
8.5	(a) The normalized R_{NL} and R_{xx} of a G/α -RuCl ₃ at 1.3 K and in the presence of a 2 T magnetic field. (b) The nonlocal resistance evolution in the presence of an external magnetic field at base temperature.	80
8.6	(a) The nonlocal resistance of exfoliated graphene and G/α -RuCl ₃ Hall bars at 1.3 K. (b) The schematic of the device and the nonlocal resistance for both Hall bars at 30 K.	81
8.7	The magnetic field evolution of the nonlocal resistance of the G/α -RuCl ₃ at the Dirac point for CVD and exfoliated graphene.	81
8.8	(a) Longitudinal resistance (R_{xx}) of exfoliated graphene at different magnetic fields. (b) R_{xx} of G/α -RuCl ₃ at $T=1.3$ K for different magnetic fields.	82
8.9	(a) Magnetic field evolution of the R_{xx} at the Dirac point for both pristine graphene and G/α -RuCl ₃ . In the case of graphene the nonlocal resistance at the Dirac point continues to increase while for G/α -RuCl ₃ at about 7 T decreases, (b) schematic of valley and (c) spin polarization of the Dirac cone.	83

1 Introduction

The recent discovery of new phases of matter has profoundly changed the way we interpret manifestations of quantum physics in materials. The details of atomic bonding and the interactions of the electrons fundamentally determines the macroscopic behavior of a material. In particular, two aspects of quantum mechanics have forged a whole new ranges of quantum materials. The first important aspect of quantum mechanics is the topological nature of the wave function of a quantum system.[7] As an intriguing example of the manifestation of this effect are topological insulators which are materials with insulating bulk which host Dirac like surface states. Another familiar example is the existence of quantized vortices in superconductors. Here the quantization arises because the superconducting condensate phase can wind around a vortex only by an integer multiple of 2π . [8] In general, the topological nature of the wave function, supports a broad range of phenomena which enable the study of fractionalized excitations with possible applications like dissipationless charge transport and quantum computation.

Another relevant feature of quantum mechanics is entanglement of the quantum states as exemplified by quantum teleportation experiments involving two photons. In principle, even the wavefunctions of two electrons in a singlet state are entangled. Considering that a bulk piece of metal contains a huge number of electrons on the order of 10^{23} electrons, it becomes evident how complicated the whole system will be. However, based upon the Fermionic statistics, it is often sufficient to take only the electrons at the Fermi surface which have access to the available states into account. Even this will leave a massive number of electrons which have entangled states.[8]

Combination of topology and entanglement will cause the emergence of new classes of particles. For example in strongly correlated systems the existence of fractionalized excitations has been predicted and signs of it has been detected in different experiments.[9, 10] Further examples are Bogoliubov quasiparticles in superconductors, and the emergence of composite fermions in quantum Hall conductors. Composite fermions [11] are known to be quasiparticles which obey the fractional exchange statistics proposed by Laughlin.[12]

Chapter 1. Introduction

High quality samples, providing materials with low amount of scattering centers together with recent advances in measurement techniques has enabled the discovery and detection of these novel states of matter.

How the above described effects determines material properties can be gleaned from the interplay of the correlations between electrons due to coulomb interaction and spin orbit (SO) interaction (see Figure 1.1).

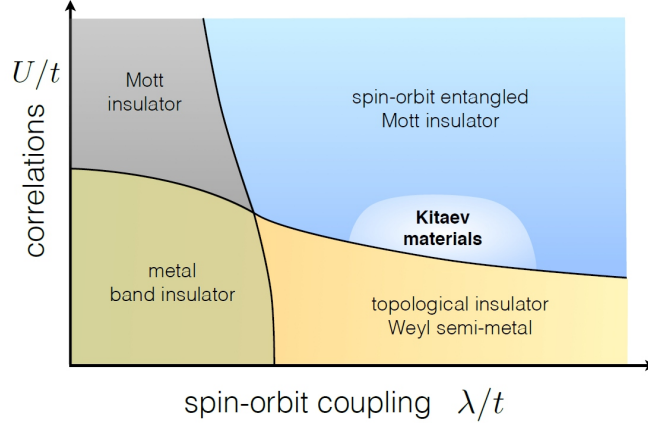


Figure 1.1 – Schematic diagram of electronic materials in dependence of the electron-electron correlation energy U/t and spin orbit coupling λ/t . The materials studied in this thesis belong to the right side of the phase diagram where spin orbit interaction is intermediate or strong. Figure from [1].

Transition metal oxides with partially filled 4d and 5d shells exhibit an intricate interplay between spin orbit coupling (SOC), electron-electron correlations and crystal field effects. The presence of strong spin orbit coupling in these materials, in the weak correlation regime leads to the emergence of topological insulators including compounds like Bi_2Te_3 , Sb_2Te_3 and $\text{Bi}_2\text{Te}_2\text{Se}$. [1] By comparison, the Coulomb interactions in Mott insulators in the strong correlation regime are so strong that the electrons are localized at atomic sites. Mott insulators with 4d or 5d orbitals show very different characteristics from corresponding materials with 3d orbitals. [13] In the former, the comparable relativistic spin orbit interaction and Coulomb interactions lock the spin and orbital degrees of freedom, resulting in highly frustrated magnets. Such a frustration will prohibit the formation of classical magnetic ordering, thus leading to called spin liquid systems in analogy with liquid Helium. Among the materials which are predicted to show spin liquid phase is $\alpha\text{-RuCl}_3$ as a promising candidate to manifest Kitaev physics and spin liquid phase. [14, 15] Since these materials are predicted to host Majorana quasiparticles with non-Abelian statistics, they may find application in novel types of electronic devices.

Apart from investigating the materials in order to study new physical phenomena, implementing them in device geometries introduces a whole new realm of challenges.

The main aim of this thesis was to fabricate and characterize novel types of heterostructures comprised of SO materials. A major emphasis was on exploring the suitability of the heterostructures as components of novel (in particular, thermoelectric or spintronic) devices, as well as to identify possible new electronic features arising from the combination of two differently doped TIs, or of a 2D quantum material (i.e., graphene) with a magnetic insulator (i.e., α -RuCl₃). The content of this thesis is divided into the following chapters:

Chapter 2 provides the necessary theoretical background related to the region in the phase diagram where SOC is strong and the electron-electron correlations are weak. These two effects in the presence of time reversal symmetry lead to the emergence of topological insulators. In this context, a closer look will be taken at the materials physics in this regime, and the principles underlying the specific properties of topological insulators explained.

Chapter 3 addresses the physics of materials in the phase diagram where electron-electron correlations gain relevance. It is described how SO interactions lead to enhanced quantum fluctuations and as a result highly nontrivial magnetic ordering can emerge.

Chapter 4 outlines the experimental methods employed in this thesis and describes the implementation principles of the experiments in combination with device geometries and device fabrication techniques.

In **Chapter 5** the general electrical transport properties of the investigated topological insulators are described, including the influence of external magnetic fields. Furthermore, the fabrication methodology and characterization of lateral as well as vertical TI heterostructures are described.

The focus of **Chapter 6** is on the use of scanning photocurrent microscopy to investigate the photocurrent generation mechanism in the topological insulator heterostructures. After introducing the principles underlying the photocurrent measurements, the obtained experimental results are interpreted on the basis of the photo-thermoelectric effect.

Chapter 7 is devoted to the description and study of α -RuCl₃, a newly emergent material as a suitable candidate for the study of the Kitaev physics and spin liquid systems. We start with the inelastic photon experiments and further investigate the material through electric transport experiments.

Chapter 8 deals with the electrical behavior of graphene in proximity with the magnetic insulator α -RuCl₃. The obtained data indicate the presence of significant magnetic exchange field coupling at the graphene/ α -RuCl₃ interface. At the same time, the graphene within these heterostructures serves as a suitable probe for the magnetic properties and spin orientation of α -RuCl₃, which are the subject of intense current research.

Chapter 1. Introduction

Finally **Chapter 9** summarizes the work done in this thesis. In addition we will discuss about the possible future experiments which according to the experiments done in this thesis and conclusions driven could provide more information about the materials and ideas investigated in this work.

2 Theory of Topological Insulators

Spin-orbit coupling (SOC) is a relativistic effect which links the spin and angular momentum of an electron. The fine structure suppresses this effect however the atoms with large number of protons can have significant SOC. In weakly correlated materials, SOC entangles the crystal momentum and spin of the electron, locking the kinetic and internal degrees of freedom together leading to a whole new material phase.[5] The concept of topological order was introduced to describe the quantum Hall effect (more precisely fractional quantum Hall states) which requires a many body approach.[16] However, the simpler case of the integer quantum Hall effect (IQHE) can also be explained by the topological order.[7] The quantum Hall state has properties, such as quantized Hall conductivity and the number of conducting edge states, which are insensitive to smooth changes of the system. In order to change these properties, the system would have to pass through a phase transition. Accordingly these properties can be interpreted in the topological order formalism. Reaching the quantum Hall state requires applying a magnetic field, whereby the time reversal symmetry of the system is broken. However, the emergence of topologically robust states does not necessarily require a symmetry breaking. Spin orbit interactions can alternatively lead to topological insulating electronic phases. The bulk of a TI in a time reversal symmetric case like an ordinary insulator has an energy gap, induced by spin orbit coupling, separating conduction and valence band, whereas the surface or edge (in the case of 2D TI) features conducting states protected by time reversal symmetry.[17] This chapter introduces the concept of topology first as an alternative explanation for the integer quantum Hall effect, and subsequently as an independent framework to classify materials.

2.1 Topology and Band Theory

2.1.1 Topology

Topology in a mathematical point of view is the study of geometrical properties of objects that are invariant under smooth deformations. For example, a Möbius stripe is a geometrical object which has only one surface and one edge. Another facet of topology becomes evident through the distinction between a sphere and a doughnut. A sphere can be smoothly deformed to

many shapes but not shapes with holes in them, such as a doughnut. The relevant quantity in this respect is genus which is essentially the number of holes in an object. Genus is an integer topological invariant, and as a result surfaces with different genus can not transform into each other smoothly. The Gauss-Bonnet theorem states that the integral of the Gaussian curvature, K over a surface defines an integer topological invariant called the Euler characteristic,

$$\chi = \frac{1}{2\pi} \int_S K dA \quad (2.1)$$

How the concept of topological invariance has evolved in physics, in particular regarding its role in band theory, will be described in the following.

2.1.2 The Insulating State

Electronic band theory provides a language to describe the electronic structure of solids. One of the simplest forms of electronic state occurs when electrons are strongly confined to the atom they belong such that there is only very weak interactions with neighboring atoms. In an insulator, a finite amount of energy is required to make an electron mobile. However covalent bonding between atoms in some materials loosens the confinement of electrons to one atom. In this case, the Bloch theorem provides Bloch states as a function of the crystal momentum $|U(K)\rangle$ which are the eigenstates of the Bloch Hamiltonian $H(K)$ to describe such states and their differences. The eigenenergies of these states $E_n(K)$ define the energy band that collectively form the band structure. In an insulator there is a large gap between conduction and valence band. Although in semiconductors this gap is smaller than in insulators, they share the same band structure characteristic and hence belong to the same phase. In other words, their band structure is interconvertible through smooth and continuous tuning of the Hamiltonian, without closing the gap and any phase transition. In the TI language, there is a topological equivalence between these states.

In the topological classification scheme, all conventional insulators are equivalent to each other, and in turn equivalent to vacuum. Vacuum, according to relativistic quantum theory, has a gap for pair production. [7] However, not all states with an energy gap are equivalent to vacuum, as explained below by taking a look at the integer quantum Hall effect.

2.1.3 Integer Quantum Hall Effect

The Hall effect was discovered by H. Hall in 1879, upon the measurement of a voltage arising from charge accumulation at the boundaries of the current-carrying sample subjected to a perpendicular magnetic field. The ratio of the voltage drop to the electric current is called Hall resistance:

$$R_H = \frac{V_H}{I} = \frac{B}{q\rho_e} \quad (2.2)$$

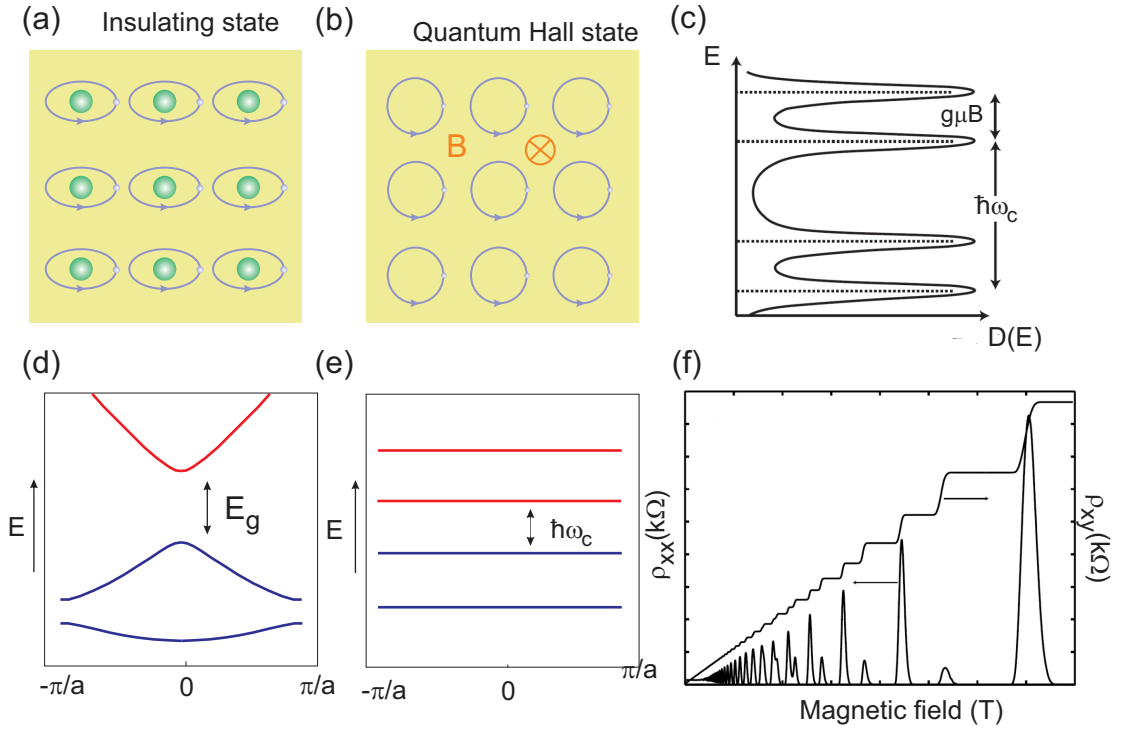


Figure 2.1 – (a,d) Schematic of the insulating state and the corresponding band structure, respectively. (b,e) Schematic of the quantum Hall state and the corresponding band structure. The energy gap between the energy levels resembles that of a trivial insulator. (c) The electronic density of states in the presence of a magnetic field and scattering events. (f) Longitudinal and Hall resistance arising from such a density of states of electrons in a B-field.[2]

In practice, the Hall effect is used for determining either of the three quantities in the equation (2.2). Von Klitzing, Dorda and Pepper discovered in 1980 that a strong magnetic field applied to a 2D electron gas leads to zero longitudinal resistance while the Hall resistance displays quantum plateaus at ne^2/h , where n is an integer called filling factor.[2] The integer quantum Hall effect is the quantum version of Hall effect and can be understood in a simplified picture base upon the cyclotron orbits of electrons in a strong magnetic field. A magnetic field introduces a cyclotron gap between Landau levels, which can be viewed as energy band in the magnetic Brillouin zone (Fig. 2.1 b and e).

However, in contrast to a normal insulator in the presence of an electric field the electrons in the quantum Hall system will drift. By now, it is realized that n is actually a topological invariant which underlies the robustness of the quantized conductance values. The key feature of the quantum Hall effect is that while the bulk electrons are localized, the edge electrons form conducting edge channels as a characteristic of a topological phase. Figure 2.1f shows the experimental Hall resistivity measured by von Klitzing, with Hall resistivity plateaus due to the formation of discrete Landau levels.

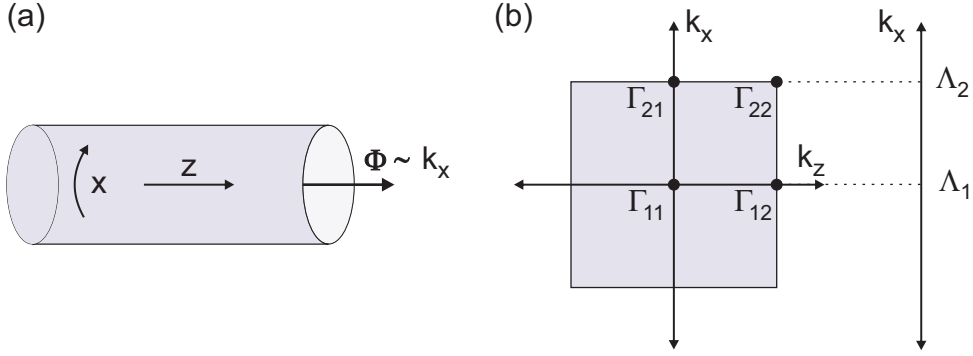


Figure 2.2 – (a) A two dimensional cylinder threaded with a magnetic flux which can be changed adiabatically. The magnetic flux resembles the edge crystal momentum when the circumference has the same value as a single lattice constant. (b) The time reversal invariant fluxes $\Phi = 0$ and $\Phi = h/2e$ correspond to edge time reversal invariant momenta Λ_1 and Λ_2 . (Figure adapted from [3])

To illustrate the connection to topology, Laughlin has argued that the quantum Hall state can be described in analogy to a charge pump.[18] A charge pumped across a one dimensional insulator is always an integer and can be defined as a topological invariant attributed to the polarization. In the next section the relation between polarization and a charge pump will be discussed. A 2D electron gas can be rolled into a cylinder along the y direction as depicted in Figure 2.2a. The surface of the cylinder is one unit cell in the reciprocal lattice. A magnetic flux threading through the cylinder can be considered as k_x . As the magnetic flux is changed by the unit of magnetic flux ($\Phi_0 = h/2e$) one charge will be transferred to the other side of the cylinder (i.e., the edge of the 2D system). Figure 2.2 b shows the relation between the fluxes $\Phi = 0$ and $\Phi = h/2e$ corresponding to the edge time reversal momenta Λ_1 and Λ_2 . Calculating the charge pumping rate using the polarization operator yields the Hall conductivity of $\sigma_{xy} = n \frac{e^2}{h}$, with n as the Chern number. The relation between the Chern number and topology will be discussed later in this chapter.

2.2 Polarization and Charge Pump

The electric polarization \mathbf{P} of an infinite crystal or a crystal with periodic boundary conditions is inherently ill-defined. This is because in a periodic solid, the polarization depends on the choice of the unit cell. For example for covalently bonded atoms no natural unit cell can be defined, and therefore the polarization cannot be uniquely defined, as illustrated in Figure 2.3. An important observation made by R. Resta is that although polarization by itself is not well defined, the changes of the polarization is. Considering a 1D lattice with Bloch states $\psi_{nk} = e^{ikx} u_{nk}$, there are N lattice points at $R_\ell = \ell a$ where a is the lattice constant. The trick for solving the problem is to define localized orbitals via Fourier transformation of the Bloch

state.[19] Thus Wannier state,

$$|nR\rangle = \frac{1}{\sqrt{L}} \sum_{k=-\pi}^{\pi} e^{-ikR_L} |\psi_{nk}\rangle \quad (2.3)$$

is localized near a lattice point R. As can be intuitively seen, in an insulator the polarization is related to the charge center of the Wannier function,

$$P = q \sum_{filledn} \langle n0|x|n0\rangle, q = -e \quad (2.4)$$

$$= \frac{q}{L} \sum_n \sum_{k,k'} \langle u_{nk'}| e^{i(k-k')x} i \frac{\partial}{\partial k} |n_{nk}\rangle \quad (2.5)$$

It can be shown that,

$$\langle u_{nk'}| e^{i(k-k')x} i \frac{\partial}{\partial k} |n_{nk}\rangle = N \delta_{k,k'} \langle u_{nk}| i \frac{\partial}{\partial k} |u_{nk}\rangle_{cell} \quad (2.6)$$

$$= \delta_{k,k'} \langle u_{nk}| i \frac{\partial}{\partial k} |u_{nk}\rangle \quad (2.7)$$

By substituting equation 2.7 into the equation 2.5, one obtains

$$P = \frac{q}{L} \sum_n \sum_k \langle u_{nk}| i \frac{\partial}{\partial k} |u_{nk}\rangle = q \sum_n \int_{-\pi}^{\pi} \frac{dk}{2\pi} A_n(k) \quad (2.8)$$

In order to represent a real physical phenomenon, the polarization needs to be gauge invariant. Under a gauge transformation $|u_{nk}\rangle' = e^{i\chi_{nk}} |u_{nk}\rangle$, the polarization contribution from band n is given by,

$$P_n' = P_n - q \frac{\chi_{n\pi} - \chi_{n-\pi}}{2\pi} \quad (2.9)$$

However, since the wavefunctions are periodic, $\chi_{nk+2\pi} = \chi_{nk} + 2\pi m$, hence,

$$P_n' = P_n - qm \quad (2.10)$$

From this result, it follows that the polarization can change by qm under the gauge transformation. That leads to the conclusion that only the fractional part of p_n is physical.

The integral in the equation 2.8 is the Berry phase which will be introduced in the next section. The Berry phase of a 1D Bloch state was first studied by Zak in 1989 and is accordingly called the Zak phase.[20] If a lattice has inversion symmetry, then

$$A_n(-k) = -A_n(k) \quad (2.11)$$

and if we apply the inversion,

$$P_n \rightarrow P_n' = \int_{-\pi}^{\pi} \frac{dk}{2\pi} A_n(-k) = -P_n \quad (2.12)$$

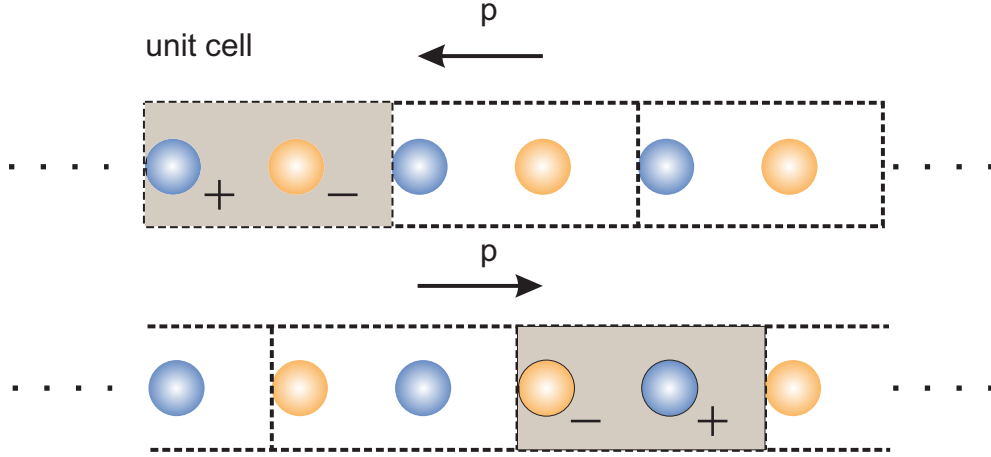


Figure 2.3 – For a periodic or infinite lattice polarization can not be uniquely defined and it depends on the choice of the unit cell.

Considering that P_n can change by qm the constraint given by the inversion symmetry is

$$P_n = (-P_n \bmod q) \rightarrow = 0 \text{ or } q/2 \bmod q \quad (2.13)$$

Correspondingly, in a lattice with inversion symmetry the charge center defined by Wannier functions in a unit cell can only be at 0 or 1/2. As changes of the polarization are well defined under an adiabatic deformation, it is convenient to introduce the parameter λ for the degree of the ion displacement. It varies from 0 to 1 as the ion shift adiabatically from an initial point to a final position. The difference in the polarization according to the control parameter λ is,

$$P(\lambda_2) - P(\lambda_1) = \int_{-\pi}^{\pi} \frac{dk}{2\pi} [A(k, \lambda_2) - A(k, \lambda_1)] \quad (2.14)$$

The change in the polarization can be written as a counter-clockwise line integral,

$$\Delta P = -\frac{q}{2\pi} \oint d\mathbf{k} \cdot A(\mathbf{k}), \mathbf{k} \equiv (k, \lambda) \quad (2.15)$$

$$= -\frac{q}{2\pi} \int d^2k F_z(\mathbf{k}) \quad (2.16)$$

where $F_z = \partial_k A_\lambda - \partial_\lambda A_k$ and $A_\lambda = i \langle u_{\mathbf{k}} | \partial_\lambda | u_{\mathbf{k}} \rangle$. If the control parameter λ is periodic, then the opposite edges have the same states, and hence,

$$\Delta P = qC_1 \quad (2.17)$$

This equality indicates that under a periodic parametric variation the charge transport is quantized. The resulting quantized charge pump was first suggested by Thouless et al. in 1982 for adiabatic conditions.[19] Interestingly, the value C_1 is a Chern number, which will be

introduced in a general term in the following section.

2.3 Berry Phase and the Chern Number

In the Schrödinger equation the choice of $|u_{n,\mathbf{k}}\rangle$ is not unique. In fact, the Berry phase arises due to the intrinsic ambiguity of the quantum mechanical wave function. For example, there is always a $U(1)$, i.e., a phase uncertainty,

$$|u_{n,\mathbf{k}}\rangle \rightarrow e^{i\Phi(\mathbf{k})} |u_{n,\mathbf{k}}\rangle \quad (2.18)$$

which keeps the Schrödinger equation invariant. A definite phase choice in the Brillouin zone is called a definite gauge. For a time reversal invariant system there always exists a continuous gauge throughout the Brillouin zone. Analogous to the electromagnetic gauge transformation, the Berry curvature is defined as following:[21]

$$\mathbf{A} = \nabla_{\mathbf{k}} \langle u(\mathbf{k}) | i \nabla_{\mathbf{k}} | u(\mathbf{k}) \rangle \quad (2.19)$$

and the Berry phase is defined as the integral of the Berry connection in the Brillouin zone:

$$\gamma_c = \int_{BZ} d\mathbf{k} \cdot \langle u(\mathbf{k}) | i \nabla_{\mathbf{k}} | u(\mathbf{k}) \rangle \quad (2.20)$$

The Chern invariant is the total Berry flux in the Brillouin zone,

$$n_m = \frac{1}{2\pi} \int d^2k F_m. \quad (2.21)$$

which is an integer quantized number. The total Chern number, summed over all occupied states $n = \sum_{m=1}^N n_m$ is invariant, provided that the gap remains finite.

A mathematical analogy of the Chern number is genus. 2D surfaces can be classified by genus which counts the number of the holes. For instance a sphere has genus 0 while a donut has $g=1$. The Gauss and Bonnet theorem in mathematics states that the integral of the Gaussian curvature over a closed surface is a quantized topological invariant proportional to its genus. The Hall conductance in a two dimensional band insulator can be expressed in terms of the Berry curvature:

$$\sigma_{xy} = \frac{e^2}{h} \int_{BZ} \frac{d\mathbf{k}}{(2\pi)^2} \Omega_{k_x, k_y} = n \frac{e^2}{h} \quad (2.22)$$

where the integer n is again the Chern number.[19, 21]

2.3.1 Quantum Hall Effect and Band Theory

In 1988 Haldane proposed that the integer quantum Hall effect can be realized in a lattice system of spinless electrons in a periodic magnetic flux. Under this condition, the total

magnetic flux is zero, while the electrons form conducting edge channels. Since in this model no net magnetic field is considered the edge channels arise from the band structure the electrons are in and not from the formation of Landau levels.[22] The system studied in the Haldane's model was graphene. In this 2D material, the conduction and valence band touch at two distinct points in the Brillouin zone. Near these two points, the electronic band structure resembles that of massless relativistic particles described by the Dirac equation:

$$H(\mathbf{k}) = \mathbf{h}(\mathbf{k}) \cdot \vec{\sigma} \quad (2.23)$$

where $\vec{\sigma} = (\sigma_x, \sigma_y, \sigma_z)$ are Pauli matrices and $\mathbf{h}(\mathbf{k}) = (h_x(\mathbf{k}), h_y(\mathbf{k}), 0)$. Considering that inversion symmetry takes $(h_z(\mathbf{k}))$ to $(-p_z(-\mathbf{k}))$ and time reversal symmetry takes it to $(+p_z(-\mathbf{k}))$, the third component of Hamiltonian has to be zero. In graphene the zeros of $(h_z(\mathbf{k}))$ occur at two points, \mathbf{K} and $\mathbf{K}' = -\mathbf{K}$. For wave vectors close to the zero points of $p(\mathbf{k})$ (\mathbf{q}) the Hamiltonian has the form of a 2D massless Dirac Hamiltonian:

$$H(\mathbf{k}) = \hbar v_f \mathbf{q} \cdot \vec{\sigma} \quad (2.24)$$

The degeneracy of the Dirac points is protected by both the time reversal symmetry and inversion symmetry. If any of these two symmetries is broken then the Hamiltonian would be that of a massive Dirac Hamiltonian:

$$H(\mathbf{k}) = \hbar v_f \mathbf{q} \cdot \vec{\sigma} + m \sigma_z \quad (2.25)$$

where $m = h_z(\mathbf{K})$. Time reversal symmetry requires that $m' = h_z(\mathbf{K}')$ has the same magnitude and sign as m , and hence this state represents a trivial insulator. The dispersion relation $E_q = \pm \sqrt{|\hbar v_f \mathbf{q}|^2 + m^2}$ indicates an energy gap of $2|m|$.

Haldane assumed lifting the time reversal symmetry by an oscillating magnetic field which is zero on average over the surface and has the symmetry of the lattice. This perturbation allows a nonzero $(h_z(\mathbf{k}))$ and as a result introduces a mass to the Dirac equation.[17] However inversion symmetry requires that the masses at \mathbf{K} and \mathbf{K}' have opposite signs. Haldane showed that this state is not an ordinary insulator but a quantum Hall state with each Dirac point contributing $\sigma_{xy} = \frac{e^2}{2h}$ to the conductivity.

2.3.2 Edge States and Bulk Boundary Correspondence

A fundamental consequence of the topological classification is the existence of gapless edge states at the interface where topological invariant changes. As already described above, a well known example of such robust edge states occurs at the interface of an integer quantum Hall state and vacuum (an ordinary insulator). A common simplification is to picture these states to form when electron trajectories at the edges bounce off the edge. This motion is chiral, meaning that along the edge electrons move in a certain direction. Backscattering is forbidden due to the absence of available states which in turn accounts for the accuracy of quantized electronic transport across the edge. The origin of the edge states is intimately related to

the topology of the bulk of the quantum Hall state. Specifically when a system undergoes a continuous interfacial transition between a quantum Hall state ($n = 1$) and a trivial insulator ($n=0$), somewhere the energy gap has to close, in order to change the topological invariant. A simple theory of the chiral edge states based on the Jackiw and Rebbi approach can be developed using a band Dirac model. Assuming that mass is a function of y , $m = m(y)$, so that for a fixed positive m' , $m > 0$ for $y > 0$ and $m < 0$ for $y < 0$. [19] The Schrödinger equation for this condition has an exact solution, with the following dispersion relation:

$$E(q_x) = \hbar v_f q_x \quad (2.26)$$

The Fermi level intersects this energy band with a positive group velocity $\frac{dE}{dq_x} = \hbar v_f$, thus defining a right moving chiral edge mode.

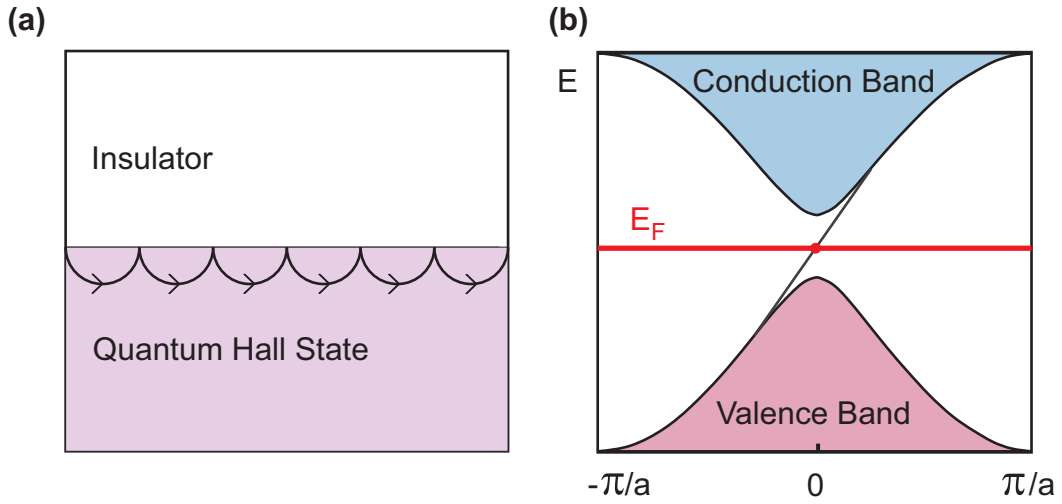


Figure 2.4 – (a) The edge chiral mode at the interface of a quantum Hall state and a normal insulator. (b) Energy band diagram of the system showing the electronic structure of the semi infinite stripe described by Haldane.

Such a chiral edge state is shown in figure 2.4. In the corresponding band diagram of figure 2.4b the edge state connects the bulk valence band to the bulk conduction band with a positive group velocity. By tuning the Hamiltonian the dispersion of the edge state can be modified, for instance to add a kink so that the Fermi level intersects the edge states three times, two times with positive velocity and one time with negative velocity. At the same time, however, the difference between the number of left and right moving modes is protected and must remain unchanged. This condition is called the bulk-boundary correspondence: [23]

$$N_R - N_L = \Delta n \quad (2.27)$$

where Δn is the difference in the Chern number across the interface, which is governed by the bulk topology.

2.3.3 Quantum Spin Hall Effect

In the following year after the discovery of Hall effect, the anomalous Hall effect was discovered which is the Hall resistance in a ferromagnetic or even paramagnetic metal.[24] The Hall resistance in ferromagnets typically has a linear term and a term arising from the intrinsic magnetization (M):

$$R_H = R_0 B + R_A M \quad (2.28)$$

The explanation for the origin of this effect took almost one century and is being related to the topology of band structure in solids. The anomalous quantum Hall effect (AQHE) can have either an extrinsic origin arising from disorder-related spin-dependent scattering or an intrinsic origin arising from spin orbit coupling of the electrons which can be expressed in terms of the Berry phase in the momentum space.

Although the absence of magnetic flux and magnetization leads to the absence of the Hall effect, the spin dependent deflection of motion can lead to measurable effects. This leads to the accumulation of oppositely oriented spins in the two opposite boundaries of a current-carrying sample. Actually the role of the periodic magnetic flux in the Haldane model can be replaced by spin orbit coupling. The resulting quantum spin Hall effect is a spin version of the quantum Hall effect and can be considered as a combination of the two quantum anomalous Hall effect of spin-up and spin-down electrons with opposite chirality.

In the SQHE, while no net charge transport occurs, there is a nonzero spin Hall conductance. As illustrated in Figure 2.5a the spin and orbital directions are locked, which is known as helicity. In terms of band theory, in the bulk gap region of the dispersion diagram the two edge states with locked spin directions are crossing[25] (Figure 2.5c).

After its theoretical prediction by Bernevig, Hughes, and Zhang in 2006[26], the QSHE was experimentally realized in CdTe/HgTe/CdTe quantum wells by König et al. They showed that in the absence of an external magnetic field and in high mobility CdTe/HgTe/CdTe quantum wells the insulating regime features a residual conductance plateau of $2e^2/h$, as depicted in Figure 2.5 b and d.

2.4 3D Topological Insulators

Since in three dimensions electrons are not constrained to a surface there is no quantum Hall effect. The QSHE cannot be extended to three dimensions by simply generalizing the transverse transport of electron charge or spin from 2D to 3D. Instead it is the evolution of the bound states near the system boundary based on the intrinsic bulk band structure. The one dimensional helical edge states in a 2D quantum spin Hall system evolve into 2D surface states surrounding the 3D topological insulator.[19] The simplest form of the Hamiltonian describing such states can be considered as, $h = v\sigma \cdot \mathbf{p}$ where the particle momentum is represented by a

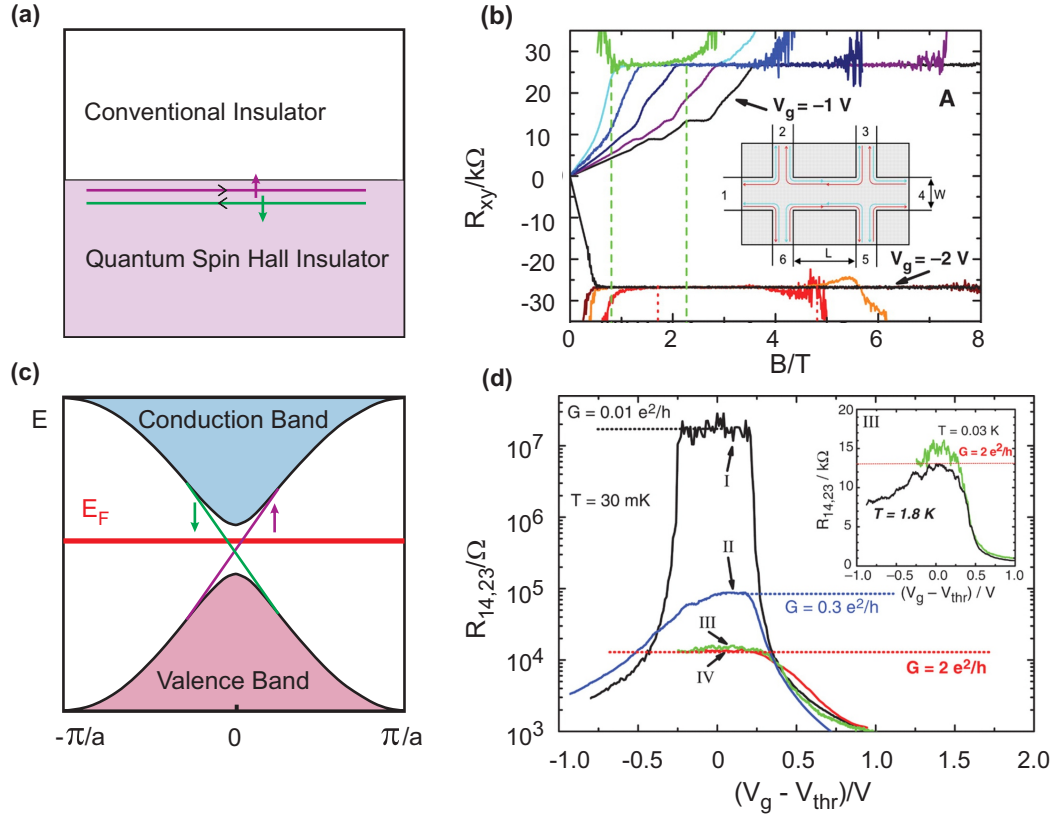


Figure 2.5 – (a) and (c) Interface between a QSHI and a normal insulator and schematic of the band diagram for the SHI. (b) Hall resistance for a HgTe/(Hg,Cd)Te quantum well at different gate voltages showing a transition from n-type to p-type by decreasing the gate voltage. The sample undergoes an insulating phase for $-1.9V < V_g < -1.4V$. (d) Experimental observation of the 2D QSHE in HgTe/(Hg,Cd)Te quantum wells. In the insulating regime in the presence of a small magnetic field samples III and IV show quantized conductance associated with edge states. (Adapted from König et al [4])

two-dimensional vector on the surface:

$$\mathbf{p} = (p_x, p_y, 0) \quad (2.29)$$

The surface Hamiltonian can then be written as a 2×2 matrix,

$$h = v(\sigma_x p_x + \sigma_y p_y) \quad (2.30)$$

The energy E_p of a surface state with momentum \mathbf{p} is obtained by solving the eigenvalue equation,

$$v\sigma \cdot \mathbf{p}\psi = E_p\psi, \psi = \begin{pmatrix} \psi_{\uparrow} \\ \psi_{\downarrow} \end{pmatrix} \quad (2.31)$$

Chapter 2. Theory of Topological Insulators

where ψ is a spinor with two components for spin up and spin down. Solving the equation 2.31 for E_p yields,

$$E_p = \pm v |\mathbf{p}| \equiv \pm v \sqrt{p_x^2 + p_y^2} \quad (2.32)$$

This dispersion relation has the form of a cone with the signs \pm referring to positive and negative energy branches. The conical energy spectrum is reminiscent of an ultra-relativistic Dirac electron and accordingly the surface states in 3D TIs are often called Dirac fermions.

In analogy to the charge pump cylinder in the 2D case, a 3D system can be generalized to a torus as depicted in Figure 2.6a with two magnetic fluxes corresponding to the two components of the surface crystal momentum (Figure 2.6b). There are eight time reversal

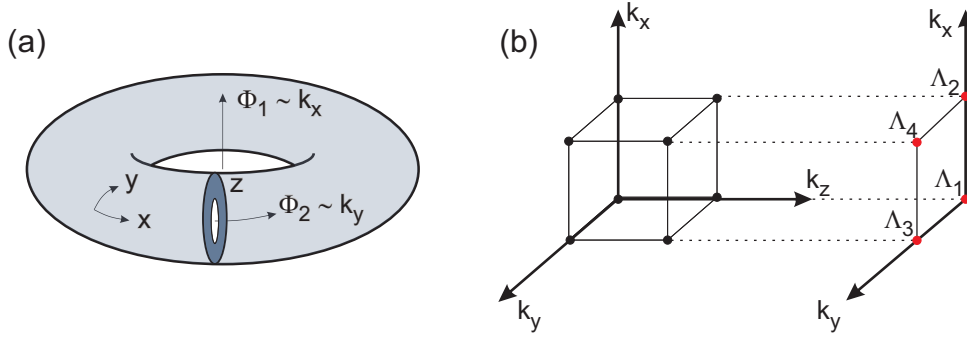


Figure 2.6 – (a) Generalized cylinder in 3D can be visualized as a corbino donut, with two fluxes corresponding to the two components of the crystal surface momentum. (b) The four time reversal invariant fluxes Φ_1 and $\Phi_2 = 0, h/2e$ corresponding to four 2D surface momenta Λ_a .

invariant momenta for 3D systems and the projections of pairs of these points reside within the 2D BZ, whereby the problem is reduced to a 2D Brillouin zone. Kane and Mele proposed a Z_2 index to classify the materials with time reversal invariance into strong and weak topological insulators[19, 17] (as described in further detail in section 3.3.1).

Among the four possible Z_2 topological invariants ($\nu_0; \nu_1 \nu_2 \nu_3$), ν_0 generally determines whether an odd or even number of pair of Kramer points are enclosed in a Fermi arc. The four time reversal symmetry protected points $\Lambda_{1,2,3,4}$ in the surface Brillouin zone are degenerate due to Kramers theorem. Away from these points spin orbit coupling lifts the degeneracy. These Kramer degenerate points form 2D Dirac points in the surface band structure, and the way these points are connected determines whether the state is trivial or topologically protected. The first experimentally proven 3D TI to be reported was $Bi_{1-x}Sb_x$ whose surface states were mapped in an angle-resolved photoemission spectroscopy (ARPES) experiment (Figure 2.7a). Later on, many other 3D topological insulators including Bi_2Te_3 , Bi_2Te_2Se and Sb_2Te_3 were documented.[27]

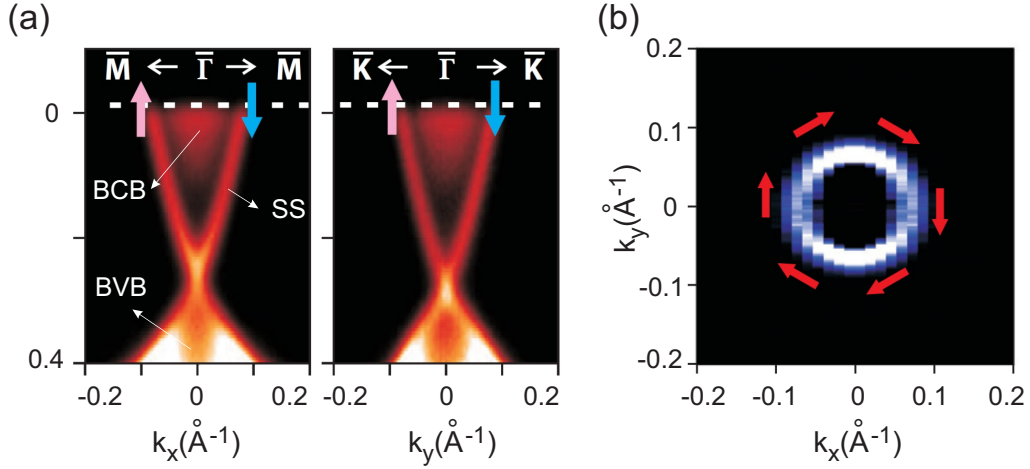


Figure 2.7 – (a) ARPES intensity for Bi_2Se_3 as a function of energy and momentum revealing surface states with a single spin polarized Dirac cone. (b) The Fermi surface as a function of k_x and k_y showing a chiral spin texture.[5]

2.4.1 Weak and Strong Topological Insulators

In a 2D system there are four time reversal invariant moments in the first Brillouin zone (Figure 2.2).[3] In this case the Z_2 invariant is given by

$$(-1)^\nu = \prod_{i=1}^4 \delta_i \quad (2.33)$$

δ_i is generally determined by:

$$\delta_i = \frac{\sqrt{\det[w(\Gamma_i)]}}{Pf[w(\Gamma_i)]} \quad (2.34)$$

where the function w is a $2N \times 2N$ unitary matrix which is closely related to the time reversal operator, Θ , and is given by:

$$w_{mn}(k) \equiv \langle u_{m,-\mathbf{k}} | \Theta | u_{n,\mathbf{k}} \rangle \quad (2.35)$$

For a 2D system, there is only one value for ν which determines whether the system is topologically invariant or not. A 3D TI has eight time-reversal invariant points which leads to four independent Z_2 topological invariants $(\nu_0; \nu_1 \nu_2 \nu_3)$. Among these, ν_0 is the product over all eight points $(-1)^{\nu_0} = \prod_{i=1}^8 \delta_i$ while the other three are given by the products of four δ_i for which Λ_i reside in the same plane. Depending on the value of the ν_0 the 3D TIs can be divided into weak and strong TIs. The four time reversal symmetry protected points $\Lambda_{1,2,3,4}$ in the surface Brillouin zone are degenerate due to Kramers theorem. Away from these points spin orbit coupling lifts the degeneracy. These Kramer degenerate points form 2D Dirac points in the surface band structure and the way these points are connected determines whether the state is trivial or topologically protected.[3, 7, 17] Figure 2.8 compares the two simplest

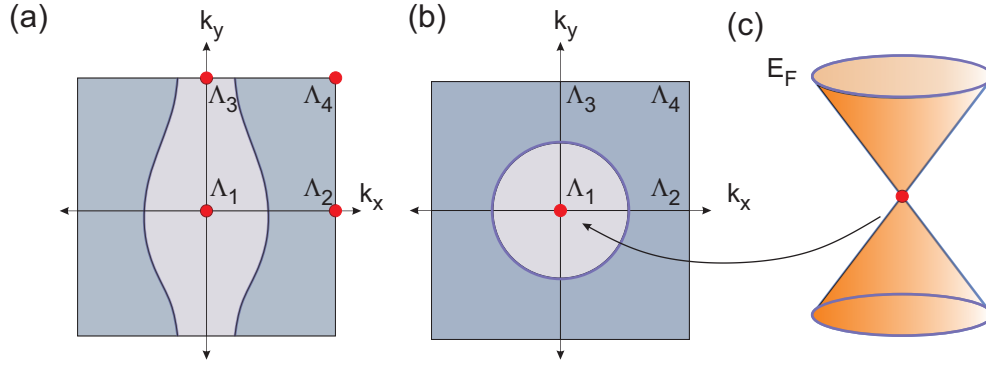


Figure 2.8 – Fermi arcs in the surface Brillouin zone for (a) a weak topological insulator and (b) a strong topological insulator. (c) In the simplest form of a strong topological insulator the Fermi arc is a circle and encloses a single Dirac point.

cases of 3D weak and strong topological insulators labeled according to $\nu_0, \nu_1 \nu_2 \nu_3$. In the case of weak TIs, the Fermi arc contains an even number of Dirac points, whereas strong TIs feature only one Dirac point. For a weak TI the surface states are not stable against disorder or impurities. The simplest weak TI may be built by stacking 2D quantum spin Hall insulators on each other. In comparison, strong TIs are closely related to the quantum spin Hall effect and their surface states are robust as they are protected by time reversal symmetry against disorder.

3 Kitaev Physics

As discussed in the introduction the combined influence of electron-electron correlations and spin-orbit coupling (SOC) leads to emergent quantum phases and transitions in heavy transition metal compounds with $4d$ and $5d$ elements. Especially the effects of spin-orbit entanglement introduced by SOC influence the electronic and magnetic characteristics of these materials.[1] In the weak correlation regime this leads to the emergence of nontrivial band structures like that of topological insulators. In the strong correlation regime, in contrast, spin-orbit entanglement partially or fully removes the orbital degeneracy, which can lead to enhanced quantum fluctuations, highly nontrivial magnetic structures as well as possible realization of spin liquid systems. The increasing interest in this field has been driven by several motivations. Not only the realization of the spin liquid systems with Majorana fermions as their quasi-particle can be an effective candidate for the fault-tolerant topological quantum computation, it has also deeply invoked the pursuit of physics of such systems. To name a few it has thrived the pursuit of the synthesis of spin liquid materials, the discovery of Majorana fermions and a direct probe of underlying Z_2 S gauge physics.[28] In this chapter we briefly introduce the concept of spin-orbit entangled Mott insulators and its connections to Kitaev physics, complemented with an overview of the thus far most experimentally investigated materials.

3.1 Spin Orbit Assisted Mott Insulators

Referring to the phase diagram in chapter 1 (Figure 1.1), in the strong SOC regime by increasing the electron-electron correlation above the topological insulator phases, spin-orbit assisted Mott insulators can be realized. The transition metal materials with d shells have stronger spin-orbit interactions, making them suitable building blocks for the aforementioned phases. Several energy scales are to be considered in such materials, specifically atomic interactions U , Hund's coupling J_H , the SOC λ , the crystal field Δ and the electron kinetic energy described by hopping integral t . [1, 28, 13] Theoretical and experimental studies of $3d$ shell transition metals have focused on high temperature superconductor cuprates, as well as manganites and vanadium oxides. In $3d$ shell materials the atomic interactions, kinetic energy and crys-

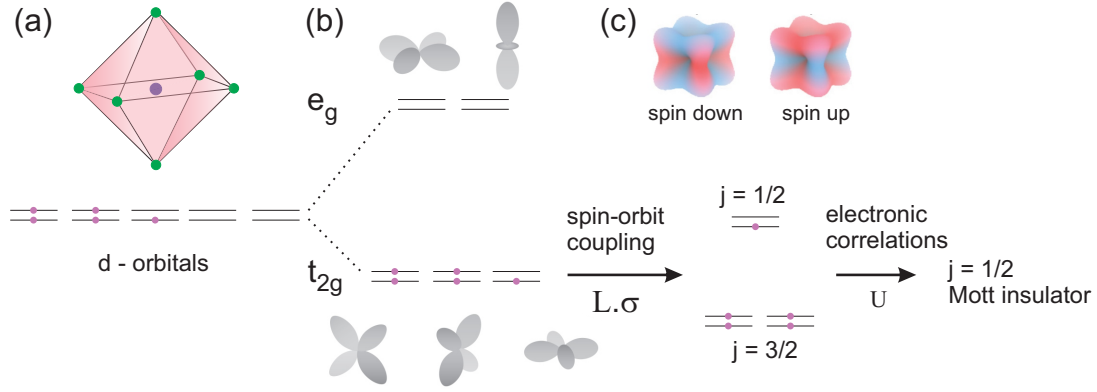


Figure 3.1 – (a) An illustration of the octahedral geometry of a transition metal. (b) Formation of t_{2g} and e_g orbitals in the presence of the crystal field. The t_{2g} state in the presence of spin orbit coupling splits into $j = 1/2$ and $j = 3/2$ states. In the presence of a strong electron-electron correlation such a $j = 1/2$ state is localized, leading to an insulating behavior. (c) The composition of the $j = 1/2$ states with spin up or down configuration as a result of the spin orbit coupling.

tal field can compete while the SOC remains relatively small. In contrast to $3d$ transition metal materials, in the $4d$ and $5d$ materials SOC is strong as well, and depending on the slight tilt toward the strength of any of the competing energy scales, can drive the system to another phase, leading to the existence of a rich phase diagram. In the solids of interest here, the d orbitals are split into a t_{2g} triplet and an e_g singlet due to the octahedral crystal field potential.[29] As depicted in Figure 3.1 b, the degeneracy of the t_{2g} orbitals is further lifted due to the SOC, which splits the t_{2g} multiplet to a $j = 3/2$ quartet and $j = 1/2$ doublet orbitals with an energy gap of $3\lambda/2$. The interactions of the $j = 1/2$ electrons are governed by the atomic interactions of the t_{2g} orbitals and the associated hopping terms. It is only because of an enhanced spin-orbit term that the effective electronic band width of these materials is reduced to such an extent that the largely suppressed electronic correlations can still drive the system to a Mott insulating regime. Accordingly, these $j = 1/2$ Mott insulators are called "spin orbit assisted Mott insulators".[28, 1] The perovskite materials such as Sr_2IrO_4 where the first to be experimentally realized as spin-orbit assisted Mott insulators.[30] Remarkably, Sr_2IrO_4 is an isostructure of La_2CuO_4 which is the parent compound of the cuprate superconductors. The ground state of Sr_2IrO_4 resembles the cuprate superconductors, including the formation of long-range antiferromagnetic order. This compound comprises corner-shared octahedra with tetragonal distortions and octahedral rotations. Owing its resemblance to the superconductor cuprates, there is currently an intense study searching for superconductivity in this material.

There is also increasing interest in the study of $j = 1/2$ Mott insulators with strong bond-

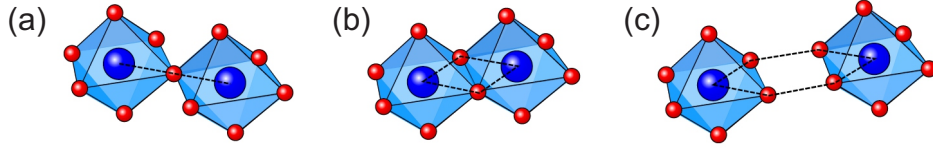


Figure 3.2 – Illustration of possible geometric orientation of neighboring IrO_6 octahedra (a) corner sharing like Sr_2IrO_4 (b) edge sharing like Na_2IrO_4 , $\alpha - Li_2IrO_3$ and $\alpha - RuCl_3$. (c) parallel edge sharing.

directional exchange interactions. It has been suggested that these materials exhibit unconventional forms of magnetism such as the emergence of spin liquid systems. However despite tremendous efforts the realization of a quantum spin liquid remains unresolved. Significant attempts have been directed toward geometrically frustrated antiferromagnets, such as those on Kagome or triangular lattices. However, most of thus far investigated materials show Heisenberg-like exchange interactions with geometrical distortions, leading to experimental and theoretical ambiguities. A promising approach to deal with the latter has been the exactly solvable Kitaev model. It is a highly anisotropic compass model where frustration arises not from the geometry of the lattice, but from the intertwining of spatial and orbital degrees of freedom.

3.1.1 Bond-Directional Interactions

A major assumption of the Kitaev model is the presence of the bond-directional exchange interactions. This means that Ising-like exchange terms with the exchange easy axis depending on the spatial orientation of the bond which dominates in coupling strength over all other exchange types. Khaliullin and Jackeli in their pioneering work realized that the geometric orientation of neighboring IrO_6 octahedra plays a crucial role in determining the exchange term associated with the Ir atom located at the center.[31] Three general scenarios regarding the exchange are possible. As illustrated in Figure 3.2a in the case of corner sharing geometry there is only one Ir-O-Ir exchange path available. This geometry, which is also referred to as '180° bond', leads to a dominant Heisenberg exchange coupling between two spin-orbit entangled $j = 1/2$ moments. Conversely, in the case of edge sharing geometry (Figure 3.2b) two Ir-O-Ir exchange paths with 90° bond angles are available. The existence of two possible exchange paths turns out to be crucial as these two symmetric Heisenberg interactions destructively interfere and cancel each other. The effective Kitaev interaction for this type of bond-directional coupling is given by:

$$\sim -\frac{8t^2 J_H}{3U^2} J_1^\gamma J_2^\gamma \quad (3.1)$$

where t is the hopping term mediated by oxygen ions, J_H is the Hund's coupling and U is the strength of the electron electron interactions. The third type of geometry in Figure 3.2 c, has been realized in triangular Kitaev materials such as $\text{Ba}_3\text{IrTi}_2\text{O}_9$.

However, finding a system that exactly fulfills the Kitaev honeycomb model is challenging since no symmetry principle prohibits other interaction terms such as symmetric Heisenberg exchange terms. The generic Hamiltonian describing the interactions between $j = 1/2$ spin-orbit entangled moments takes the form:

$$H = - \sum_{\gamma\text{-bonds}} J \mathbf{S}_i \mathbf{S}_j + K S_i^\gamma S_j^\gamma + \Gamma (S_i^\alpha S_j^\beta + S_i^\beta S_j^\alpha) \quad (3.2)$$

where α and β indicate the two spin directions distinct from the edge type γ . The first term in this Hamiltonian is the isotropic Heisenberg coupling with the strength J , and the bond-directional interactions are (i) the Kitaev term with strength K that couples the component of the spins along the bond γ , and (ii) a symmetric off-diagonal exchange term that couples the two orthogonal spin terms α and $\beta \perp \gamma$. The common characteristic of Kitaev materials is the dominance of the Kitaev exchange term over the other terms, $K > J, \Gamma$. [31]

3.1.2 Kitaev-Heisenberg Model

Experimental evidence suggests that in order to gain an understanding of the physics of Na_2IrO_3 and $\alpha\text{-Li}_2\text{IrO}_3$, large Kitaev interactions should be considered. However, the low energy physics of these materials crucially depends on the details of the distortions which takes it away from a pure Kitaev model. In this case they are best described by the Kitaev-Heisenberg (KH) model with the Hamiltonian:[32]

$$\sum_{\langle ij \rangle} \mathbf{J}_i \mathbf{J}_j + K J_i^\gamma J_j^\gamma. \quad (3.3)$$

This model has attracted strong attention since it describes well the stability of the spin liquid phase and its neighboring phases. The model can be reliably understood in terms of Klein duality which maps the HK model into itself upon a change of the parameters, $J' = -J$ and $K' = K + 2J$ as depicted in Figure 3.4. The phase diagram is parametrized with $J = \cos\phi$ and $K = \sin\phi$. [33] It comprises five phases encompassing all the phases in the KH model. The stripy phase at $K = -2J < 0$ is dual to the ferromagnet and the zigzag phase at $K = 2J > 0$ is dual to the antiferromagnetic phase. The spin liquid phase, on the other hand, is stable and under the Klein duality maps to itself.

3.1.3 Kitaev Honeycomb Model

The Kitaev honeycomb model is one of the most important examples of a \mathbb{Z}_2 quantum spin liquid. The pure Kitaev model, in which there is no symmetric Heisenberg term, is described only by the first term of Hamiltonian as:

$$H_{\text{Kitaev}} = - \sum_{\gamma\text{-bonds}} K_\gamma S_i^\gamma S_j^\gamma \quad (3.4)$$

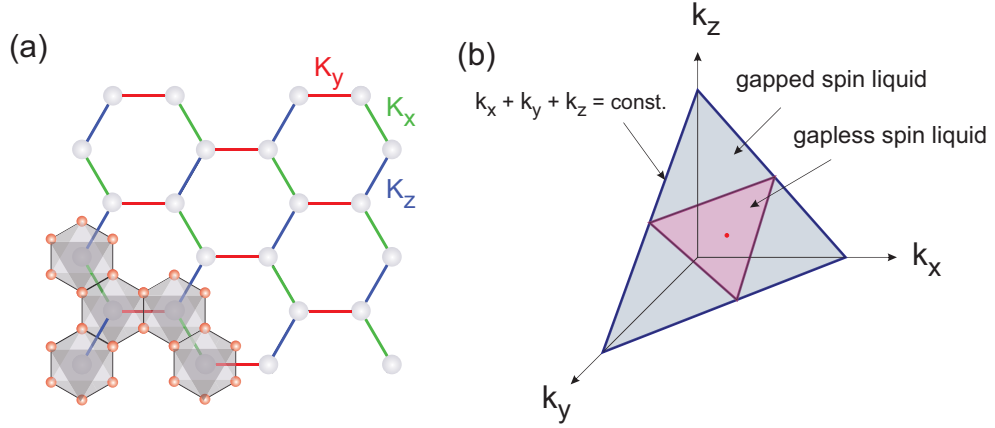


Figure 3.3 – (a) Kitaev interactions on the honeycomb lattice, the grey circles show the Ru^{+3} ions while the red ones indicate the position of Cl^{-1} ions. (b) Phase diagram of the Kitaev model. The phase diagram depicts a plane $K_x + K_y + K_z = c$ in which around the point of equal Kitaev exchange terms, a gapless spin liquid is formed.

The solution of this model is accomplished through representation of the spin operators in terms of four types of Majorana fermions, specifically b_i^x, b_i^y, b_i^z, c_i , such that $S_i^\gamma = \frac{i}{2} b_i^\gamma c_i$. Since bonds of any given type are disconnected from other bonds of the same type, the b^γ fermions are local identities. On this basis, it can be shown that, $u_{ij} = i b_i^\gamma b_j^\gamma = \pm 1$ is a constant of motion and hence the Hamiltonian can be written in the form of a quadratic Hamiltonian as:[29, 28, 31]

$$H = \frac{-i}{4} \sum_{ij} \langle u_{ij} \rangle c_i c_j \quad (3.5)$$

The states in this representation are therefore defined by the configuration of "flux" variables u_{ij} and "matter" c fermions. By fixing the gauge, the system effectively reduces to a non-interacting Majorana hopping Hamiltonian in a static background \mathbb{Z}_2 gauge field. Figure 3.3 depicts the bond-directional dependent Kitaev interactions and the resulting phase diagram for the plane of $K_x + K_y + K_z = \text{const.}$ If one of the three couplings dominates, the system will be in a gapped spin liquid phase. For approximately equal strength of the exchange interactions, a gapless spin liquid emerges. In case of a honeycomb lattice this state is a semimetal with Dirac cone dispersion, referred to as Majorana metal. The Kitaev interactions along neighboring bonds can not be satisfied simultaneously, giving rise to "exchange frustration" and driving the system into a QSL phase. It is noteworthy that Kitaev model is one of the few Hamiltonians that can be exactly solved. Therefore, it allows one to describe and monitor the fractionalization of the original spin-orbit entangled degrees of freedom into a fermionic degree of freedom, corresponding to a Majorana fermion and a \mathbb{Z}_2 gauge field.[1]

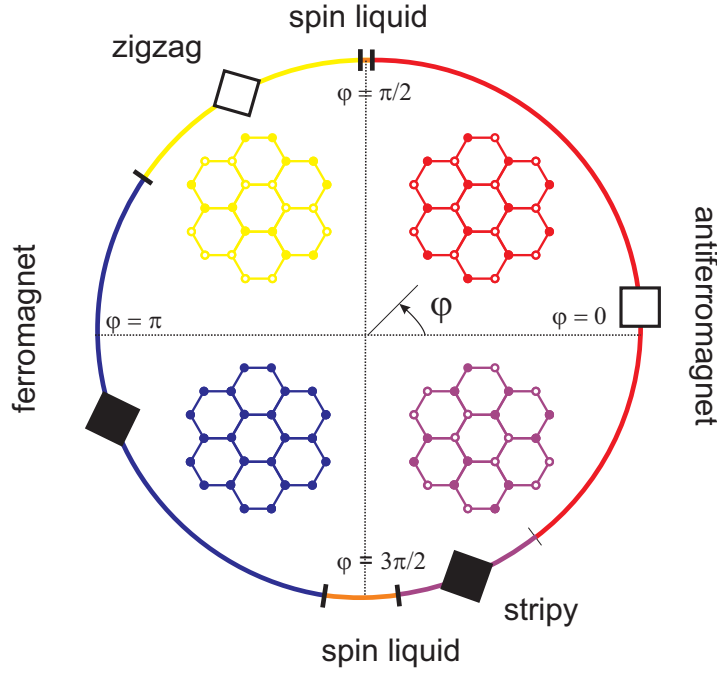


Figure 3.4 – Phase diagram of Kitaev Heisenberg model, parametrized as $J = \cos\phi$ and $K = \sin\phi$.

3.1.4 Honeycomb Kitaev Materials

The pioneering work of Jackeli and Khaliullin in 2009 in precise terms laid out the necessary criteria for identifying materials which can be considered as Kitaev materials.[31] They specially proposed iridates of the form $A_2\text{IrO}_3$ such as $\alpha\text{-Li}_2\text{IrO}_3$ or Na_2IrO_3 as promising Kitaev material candidates.[34, 9] Promising candidates thought to be proximate to the Kitaev physics are the honeycomb iridates Na_2IrO_3 and $\alpha\text{-Li}_2\text{IrO}_3$ and more recently $\alpha\text{-RuCl}_3$. [35, 34] In their ground states these materials however won't reach spin liquid phase but they rather magnetically order. However they show proximity to Kitaev physics with different degrees, making Kitaev interactions as primary interactions to understand their properties.

Experimental Status

Na_2IrO_3 was first synthesized by the groups of Takagi et al. and Gegenwart et al. with the aim of studying the associated Kitaev physics.[36, 37] To date, numerous experimental evidences suggest that Na_2IrO_3 is a Mott insulator with an insulating gap of $\Delta = 340\text{meV}$ as determined by optical transmission measurements.[38, 39] Moreover, evolution of the magnetic susceptibility has confirmed the effective $s = 1/2$ picture with the magnetic moment of $\sim 1.82\mu_B$ with a high antiferromagnetic Curie-Weiss temperature of $\Theta_{CW} \sim -116\text{K}$. [40, 37, 41] The low temperature antiferromagnetic ordering transition seen at $T_N \sim 15\text{K}$ suggests substantial frustration.[37] Neutron scattering and X-ray scattering experiments identified this ordered phase as a zigzag

ordering.[42] Although the applicability of inelastic neutron scattering is limited by the large absorption by Ir atoms, two key features below the Neel temperature could be observed. In particular, scattering near the magnitude of the zigzag ordering wave vector is present down to 2 meV while there is no scattering at smaller wave vectors and energy.[43] In addition, diffuse magnetic X-ray scattering in the paramagnetic phase has revealed an experimental confirmation of dominant Kitaev interactions, validating the theoretical predictions. Several strategies have been devised to bring Na_2IrO_3 closer to a spin liquid phase including the fabrication of thin films and integrating them in heterostructure. However the most practical scheme has been to replace Na with a lighter atom such as Li.[28]

For $\alpha\text{-Li}_2\text{IrO}_3$ an antiferromagnetic transition is seen at ~ 15 K, similar to Na_2IrO_3 , although the Currie-Weiss temperature is lower, $\Theta_{CW} \sim -33$ K. [41] Further analysis of these compounds has proved to be challenging since the synthesis of bulk single crystals is not straightforward. One of the most promising materials that recently entered the spotlight is $\alpha\text{-RuCl}_3$ which crystalizes in a close-to-perfect honeycomb lattice. It consists of very weakly bounded layers of edge sharing RuCl_6 octahedra with central Ru^{3+} ions. While originally thought to be a semiconductor, following the spectroscopic measurements in mid 1990s it was found to be a Mott insulator.[44] Optical spectroscopy experiments revealed an optical gap of 200 meV and a SOC strength of $\lambda \sim 100$ meV.[11, 45] Although the SOC strength in 4d elements is in general weaker than in 5d elements, calculations have shown that the ratio of SOC strength and electronic bandwidth (though smaller than iridate) still suffices to realize a spin-orbit entangled $j = 1/2$ Mott insulator.[1] Two successive magnetic ordering transitions at 7 K and 15 K have been experimentally observed, albeit further investigations resolved the latter one as a consequence of stacking faults in the single crystals. What sets $\alpha\text{-RuCl}_3$ apart from other Kitaev material candidates is its closer proximity to a spin liquid phase and its unusual excitations above the magnetic ordering transition. In inelastic light and neutron scattering measurements on the bulk of this material, fractionalized excitations associated with the Kitaev interactions have been observed.[34, 10] In chapter 6, the study of thin sheets of $\alpha\text{-RuCl}_3$ using Raman spectroscopy and electrical transport measurements is described.

4 Experimental Techniques

4.1 Chemical Vapor Deposition

For the topological insulator experiments, first high quality materials needed to be prepared. A major issue in studying the TIs is the elimination of the bulk contribution to the conductance. One possibility to achieve this is to reduce the thickness (i.e., to increase the surface-to-volume ratio) of the material. An alternative is electrostatic gating; however, when only a back gate is available, the gating efficiency is often too low. Another method relies on suitable doping to compensate for the unwanted extra carriers that are introduced by lattice defects. Established techniques to fabricate TI thin sheets include mechanical exfoliation, molecular-beam epitaxy (MBE), chemical vapor deposition (CVD), solvothermal synthesis and metal-organic chemical vapor deposition (MOCVD). Among them, the CVD technique combines ease of use with access to sheets of reasonable quality. The development of the CVD method dates back to the 1880s when it was used to coat the incandescent lamps with carbon or metal to improve the strength of the filaments. Since then it has advanced significantly, although some challenges still remain, such as the precise control of the stoichiometry and the crystal structure of the deposited compounds. The CVD method finds main application in the semiconductor and so-called metallurgical coating industries.

Fundamentals of Chemical Vapor Deposition

CVD is a synthesis process involving some chemical constituents which react in the vapor phase near or on a heated substrate to result in a solid deposit on it. Its mechanism is governed by aspects of several scientific disciplines like thermodynamics, kinetics and chemistry. The theoretical description of this process involves the (i) chemistry of the reaction including intermediate steps and by-products, (ii) the reaction mechanism (iii) composition of the deposit and finally (IV) the lattice structure of the deposit. A CVD reaction is controlled by thermodynamics and kinetics. Thermodynamics determines the direction in which the

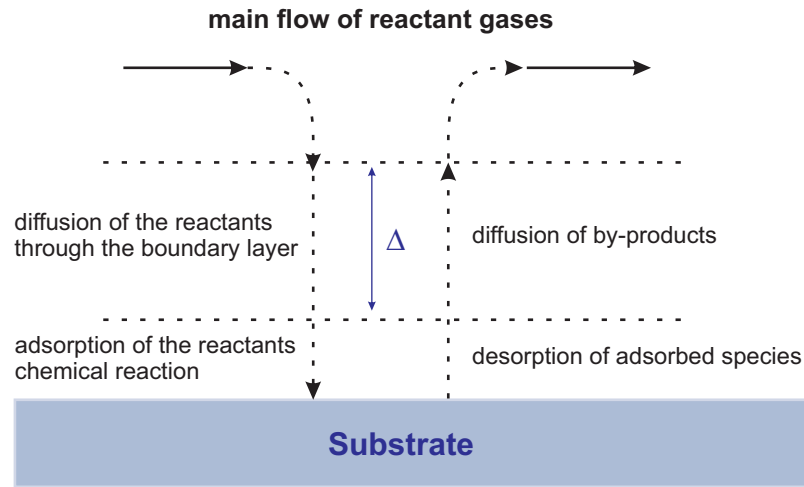


Figure 4.1 – The schematic of the steps occurring in a CVD growth mechanism.

reaction is going to proceed and kinetics defines the transport process and determines the rate control mechanism meaning how fast the reaction is going to take place. Thermodynamics is concerned with the interrelation of various energy terms for a given chemical system, in the framework of the first and second laws of thermodynamics. In particular the transfer energy which is the free energy change of the reaction ΔG_r should be negative. The free energy of a reaction (also known as Gibbs free energy) is given by:[46]

$$\Delta G_r = \sum \Delta G_f products - \sum \Delta G_f reactants \quad (4.1)$$

The free energy is not a fixed value and varies as a function of several parameters such as type of reactants, the molar ratio of the reactants, the process temperature and the process pressure. Once the thermodynamic feasibility of a reaction is ensured, the next question is how these reactants reach the deposition surface. This mass transport mechanism determines the reaction rate of the deposition process. In fact CVD process involves a complicated fluid dynamics. The fluid, comprised of a gas mixture is forced through pipes and valves, and experiences variations in temperature and pressure. The basic steps of a CVD process are illustrated in Figure 4.1. After introducing the reactant gases to the chamber (reactor), they diffuse through the boundary layer and reach the substrate surface, where then the deposition takes place. In the last step, the gaseous by-products are diffused away from the surface through the boundary layer. The relevant (dimensionless) parameter that characterizes the fluid flow is the Reynolds number, Re . [47] To good approximation, it can be assumed that the gas flow is laminar, meaning that the gaseous layers flow parallel to each other without disturbance. For laminar flow the velocity of the gas in contact with the substrate is zero. The

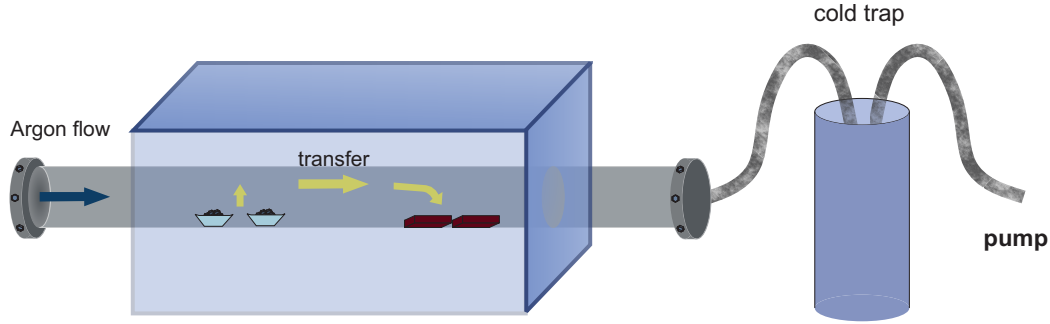


Figure 4.2 – The schematic of the CVD set up. The cold trap serves merely as a trap for heavy elements for the protection of the pump.

boundary layer as depicted in Figure 4.1 represents the region where the gas velocity changes from the main bulk flow to zero. The reactant gases flowing over this layer have to diffuse through it in order to reach the surface of the substrate. The thickness of this boundary layer is inversely proportional to the square root of the Reynolds number:

$$\Delta = \sqrt{\frac{x}{Re}} \quad (4.2)$$

where $Re = \frac{\rho u x}{\mu}$ and ρ is the mass density, u the flow density, x the distance from the inlet in the flow direction, and μ the viscosity. [48] Most importantly, the thickness of the boundary layer increases with lower gas-flow velocity and with the increased distance from the tube inlet.

4.2 Growth of $\text{Bi}_2\text{Te}_2\text{Se}$ and Sb_2Te_3

We have used the CVD method to prepare thin films of the two different 3D TIs like $\text{Bi}_2\text{Te}_2\text{Se}$ (BTS) and Sb_2Te_3 . The schematic of the CVD growth set up used in thesis is depicted in Figure 4.2. It consists of a glass tube wherein the carrier gas flows and the longitudinal temperature profile is controlled by surrounding furnace. The sources and substrates are placed in the hot and cold zone of the tube, respectively. Argon serves as carrier gas to transport the evaporated compounds along the tube. For the growth of BTS, the powder-like sources of Bi_2Te_3 and Bi_2Se_3 were placed in the hot zone of the tube, with a final growth temperature of about 580°C . The distance between the sources is about 6 cm, and the substrates are located in the colder zone, about 12 cm distance from the sources. The furnace heats the tube during different ramping stages to a final temperature distribution. The Argon flow was adjusted to 150 sccm and the pressure constantly held at about 60 mbar. Once the final stage was reached, the temperature was kept constant, and depending on the final desired geometry

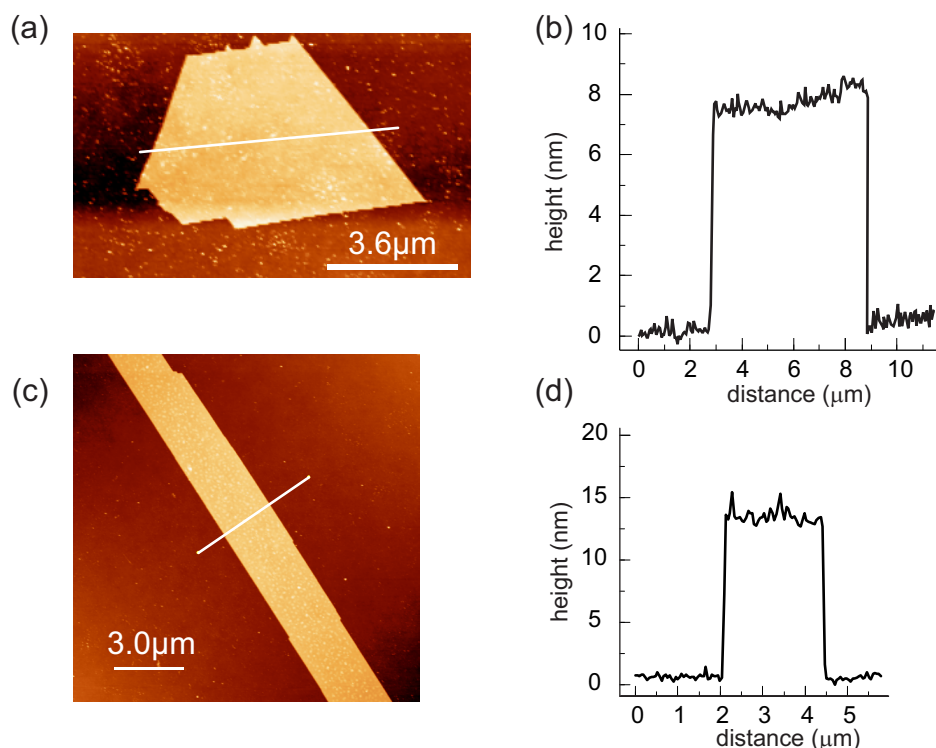


Figure 4.3 – (a) and (c) Atomic force microscopy image of two exemplary BTS flakes. (b) and (d) line profile across the white line in the AFM image showing the thickness of the nanoflakes.

and thickness of the BTS nanostructures, growth time was chosen. Figure 4.3 shows some of obtained nanoplatelet geometries, along with the corresponding AFM cross-sectional profiles.

4.3 Growth of Topological Insulator Heterostructures

For the CVD growth of lateral TI heterostructures, BTS was chosen as n-type and Sb_2Te_3 as the p-type component. The available CVD set-up only allows for an ex-situ process, as after the growth of the first compound, the sample has to be exposed to air before its transfer to a second CVD furnace. The growth order is determined by the fact that BTS has a higher melting point, and thus needs to be grown first, in order to minimize thermal evaporation of the material during the growth of the second material. The BTS/ Sb_2Te_3 nanoplatelets were synthesized through two consecutive steps of vapor-solid growth. In the first step, BTS nanoplatelets were grown on a Si/SiO₂ substrate, as this compound has a higher melting point than Sb_2Te_3 , and is hence able to sustain the growth conditions required for the latter compound. The BTS growth was performed using a source temperature of 582°C with the deposition substrate kept at 480°C. After cooling to room temperature, the substrate was transferred into another furnace where Sb_2Te_3 was grown using a source temperature of 570°C

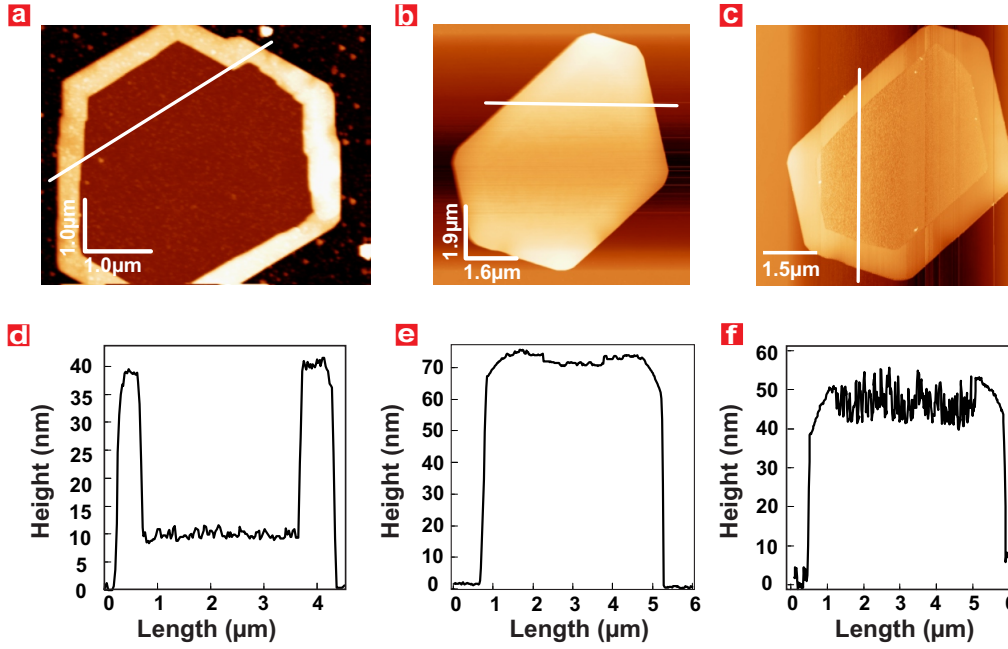


Figure 4.4 – (a,d) AFM image and the corresponding height profile across a $\text{Sb}_2\text{Te}_3/\text{Bi}_2\text{Te}_2\text{Se}$ lateral heterostructure, (b,e) AFM image and height profile of another heterostructure with pronounced lateral growth, (c,f) AFM image and height profile of the same heterostructure as in panel (b) after dry Ar etching to better visualize the two components.

and a deposition substrate temperature of 420°C . For shorter Sb_2Te_3 deposition times, lateral heterostructures were obtained, while prolonged deposition yielded vertical heterostructures wherein a closed Sb_2Te_3 film completely covers the underlying BTS nanoplatelets. Figure 4.4 shows various examples of grown heterostructures with different height and lateral extent ratios. The thickness ratio between the central BTS nanoplatelet and the Sb_2Te_3 frame at the periphery could be adjusted by the growth parameters. The respective n- and p-type doping character of the single-component BTS and Sb_2Te_3 nanoplatelets could be confirmed by Hall measurements on individual platelets (see chapter 3). In the growth experiments, it proved possible to favor lateral over vertical growth during the second growth step. By optimizing the growth parameters, lateral BTS- Sb_2Te_3 heterostructures with a smooth transition between the two different regions could be obtained. In order to clearly visualize the boundary between the two materials by AFM, argon etching was performed with the aim of exploiting the different etching rates of the two materials. The lateral extension of the peripheral Sb_2Te_3 region could be further increased through optimization of the growth time. While a growth time of 3 min resulted in 260 nm of lateral growth, a growth time of 5 min yielded an extension by 880 nm, which is sufficient for reliably positioning electrical contacts by e-beam lithography.

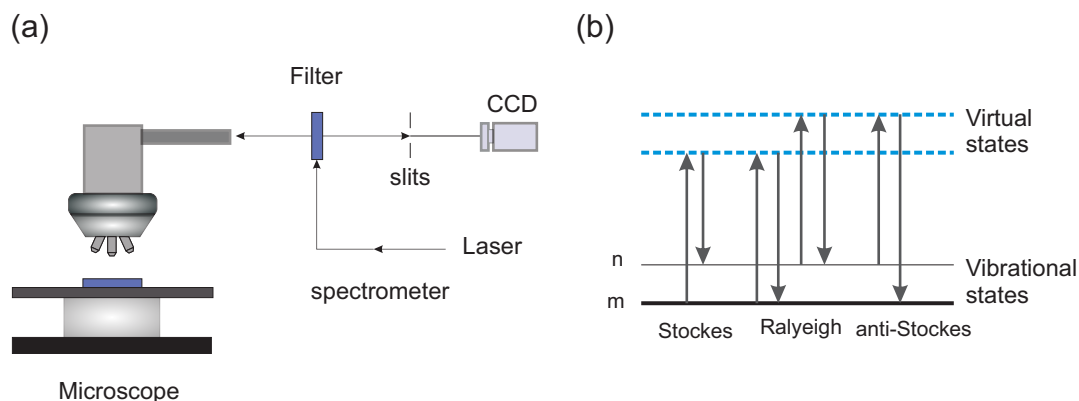


Figure 4.5 – (a) The basic parts of a Raman spectroscopy system. (b) Schematic of Rayleigh and Raman scattering processes. m state indicated the vibrational ground state and n the first excited state.

4.4 Raman Spectroscopy

Raman and infrared spectroscopy are two widely used techniques to gather information about the vibrational properties of substances, from which indirect conclusions about their chemical composition and structure can be drawn. Samples can be examined in the form of solids, liquids or vapors. The main principle of these spectroscopy techniques is based on the interaction of light with matter. The incoming light can interact with the investigated sample in two different manners. In the first case, the photons have the exact difference in energy between the ground state and an excited state. In this case light will be absorbed and the amount of absorbed light plotted in dependence of the incoming light energy yields the infrared spectrum. However this may not be the case and there can be a mismatch between energies, as a result the light only scatters from the matter. The second scenario comprises elastic or inelastic light scattering as the processes which underlie Rayleigh scattering and Raman spectroscopy, respectively. In Raman spectroscopy, the incoming photons excite a short-lived (virtual) electronic state, and are then re-emitted with an energy that has decreased or increased by one unit of vibrational energy difference. The scattered photons with decreased (increased) energy give rise to the Stokes (anti-Stokes) line, respectively, (see Figure 4.5b). In general, Rayleigh scattering has a larger cross-section than the Raman process and is hence dominant in the spectrum.

The Raman scattering intrinsically is weak since generally only one in 10^6 to 10^8 photons will be scattered inelastically.[49] The relative intensities of the Stokes and anti-Stokes scatterings depend on the population of the vibrational ground state and vibrational excited states. However at room temperature it is expected to have a higher population of ground states as a

result stronger Stokes scattering than anti-Stokes. Regarding the instrumentation, visible lasers are commonly used for excitation. The scattered light is usually collected in one of two possible configurations (i.e., 90° and 180°), which can be adjusted by appropriate mirror systems. Detecting the Raman signal requires the removal of the Rayleigh scattering, which can flood the detector especially if the Raman signal is close to the laser frequency. This is achieved with the aid of notch and edge filters. A notch filter is a filter that passes most frequencies unaltered, but significantly attenuates those in a specific, narrow range. After passing through the filter, the scattered light is focused into a monochromator which separates out the different photon energies. In this thesis Raman spectroscopy was used to characterize the CVD grown materials, and furthermore to spatially resolve the material characteristics of the TI heterostructures. Moreover, Raman measurements were used to study the unconventional magnetic excitations in α -RuCl₃ as described in chapter 6.

4.5 Scanning Photo Current Microscopy

Scanning photocurrent microscopy (SPCM) was performed with a confocal laser microscope (Leica TCS SP2), equipped with a piezoelectric table to control the movement of the stage during scanning across the sample, as depicted in Figure 4.6. The Leica microscope can be operated with Helium-Neon (HeNe operating at 633 nm), GreNe (543 nm) or Ar/ArKr (458 nm, 488 nm and 514 nm) laser at powers in the range of 1 μ W to 430 μ W. The spatial resolution for this system is about 400 nm, which is roughly the laser spot size. Upon raster scanning the

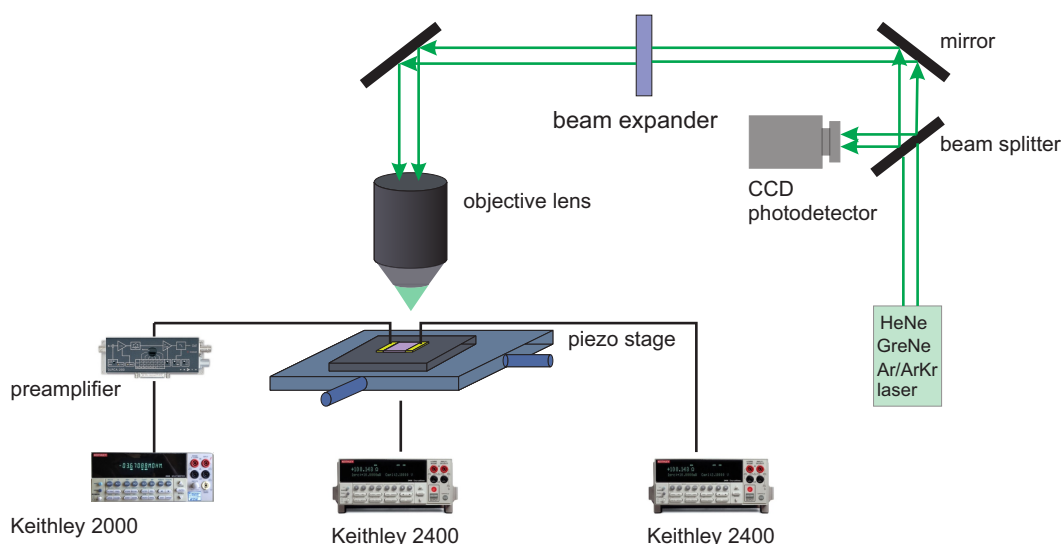


Figure 4.6 – Schematic of a scanning photocurrent microscopy set-up. The system is comprised of different laser lights and a piezo-electric stage used to scan the sample with confocal laser. The electronic set up is added to measure the generated photocurrent in the sample.

laser spot through the sample, the extra carriers generated by the incoming light are collected. In this thesis, a preamplifier is used to amplify the collected current and a Keithley to measure it. The measurements are generally carried out under zero-bias conditions.

4.6 Cryogenic Charge Transport Measurements

The electrical measurements described in chapters 4,5 and 6 were performed using an Oxford cryostat system equipped with a magnet that can provide upto 12 T magnetic field. The temperature of the sample is measured and controlled by the ITC temperature controller. This cryogenic system comprises an internal vacuum chamber (IVC) inside a ^4He bath with a temperature of 4.2 K. The IVC and bath are in contact through a needle valve, which controls the flow of ^4He to the IVC. When the IVC is continuously pumped, the boiling temperature of the ^4He is reduced and a temperature down to 1.3 K is reached. The IVC and the ^4He are surrounded by an outer vacuum chamber (OVC) to reduce the heat exchange.

4.7 Atomic Force Microscopy

In this thesis, Atomic Force Microscopy (AFM) is used mainly to study the topography of the synthesized and electrically contacted nanostructures. AFM is a versatile microscopy which not only provides information about the surface topography, but also can be used to investigate various surface properties of the nanostructure. The most common AFM operation modes are contact mode, tapping mode and noncontact mode. In the contact mode the AFM tip is in contact with the sample and the cantilever bending due to the resulting repulsive force gives information about the height of the sample. Non-contact AFM (NC-AFM) is one of the several established techniques in which an AFM cantilever is vibrated near the surface of a sample. The spacing between the tip and the sample for the NC-AFM mode is typically on the order of tens to hundreds of Ångströms. Tapping mode is an alternative technique to non-contact mode in which the cantilever oscillates just above the surface, but at a much larger oscillation amplitude. Figure 4.7 illustrates a typical AFM setup along with the different working regimes according to the potential energy-distance diagram. The bigger oscillation makes the deflection signal large enough for the control circuit, allowing for an easier control for topography feedback. It produces modest AFM results but blunts the tip's sharpness at a higher rate, ultimately speeding up the loss of its imaging resolution.

4.8 Kelvin Force Probe Microscopy

Kelvin force microscopy (KFM), an AFM-based method, allows determining the surface potential distribution of a sample, consequently acquiring information about the material composition or doping profile. The electric potential landscape of the sample surface is detected via cantilever deflection caused by an electrostatic force between the tip and the sample. The measured signal is actually the contact potential difference (CPD) between tip and sample,

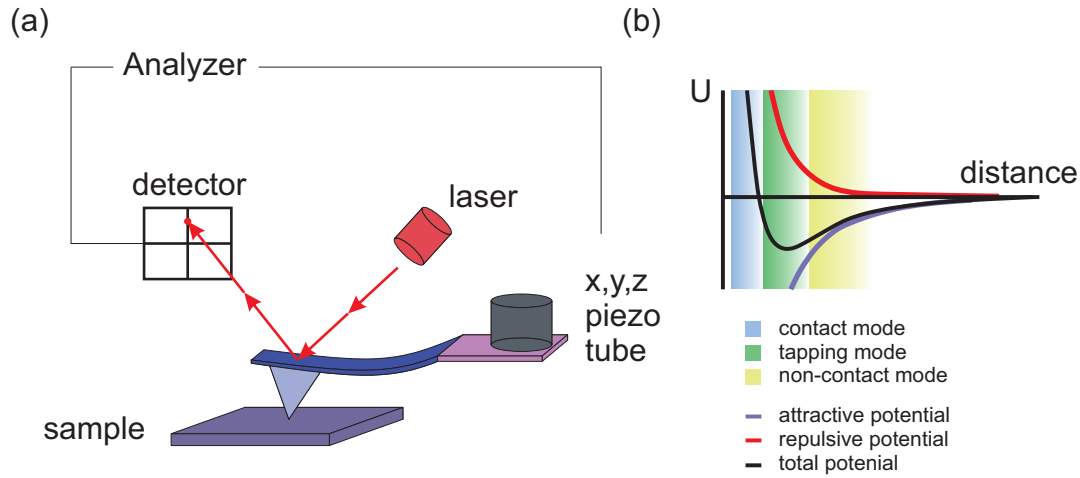


Figure 4.7 – (a) Schematic of an AFM set up. (b) The diagram of the potential between the tip and the sample as a function of distance.

i.e., the work function difference between the two. Figure 4.8 shows the operation principle of KFM method. Initially, tip and the material are far apart and hence their Fermi level have not equilibrated (Figure 4.8a). When they are brought together in contact mode, an electron flow occurs to bring the system to equilibrium (Figure 4.8b and c). The current flow is measured by the analyzer and it applies a potential to compensate for the contact potential. At the end this is this compensated contact potential that is shown in KFM image.

4.9 Nanostructure Patterning by E-beam Lithography

Electron beam lithography (EBL) is used to pattern the nanostructures under study. Compared to optical lithography, EBL offers a better spatial resolution enabled by the smaller wavelength of the electrons.

An EBL is composed of several essential parts which produce the electron beam (source-beam gun), a deflection unit to control and guide the electron beam and a laser interferometer-controlled stage. After growing the nanosheets of TIs or heterostructures of them, AFM imaging is done to estimate their thicknesses. Using a graphic software position of the electrodes is defined. The substrate is first coated by an e-beam resist (PMMA), used as a patterning mask. Two PMMA layers are subsequently coated to reduce the undercut effect due to the electron scattering of the electron beam incident on the sample. Electron beam will break the PMMA atomic chain in the exposed area defined as an electrode. Solving the broken PMMA chain using a developer (MIBK for the case of PMMA), it will be washed away and will be ready for the metal deposition. The next step is to load the sample in an evaporation chamber to deposit metallic electrodes. The best contact resistances are achieved under low base pressure of the chamber (10^{-8} mbar). The thickness of the evaporated metal has to be individually adjusted

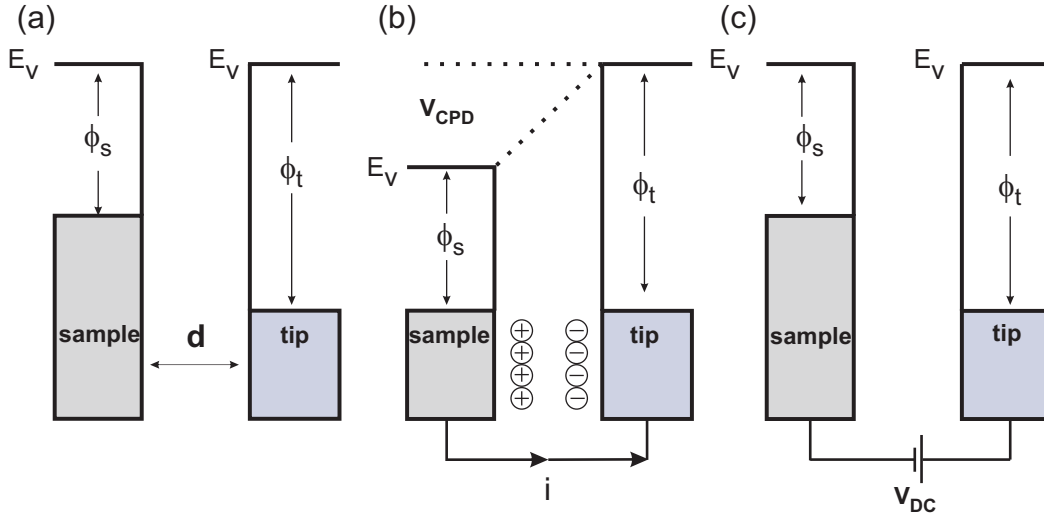


Figure 4.8 – Working principle for a KFP measurement, (a) sample and tip are far away, (b) in contact and (c) the compensation DC voltage is applied.

to the thickness of each nanosheet. Finally, the last step is lift-off, whereupon the metal film on top of the PMMA is removed with a solvent. Figure 4.9 illustrates the steps involved in patterning the nanosheets. It is necessary to mention that in contacting the TI heterostructures another lithography step had to be incorporated to bridge across one material and reach the desired material in the middle of the structure. The bridging has been done using an oxide layer, in this case SiO_2 , evaporated in a second lithography step.

4.10 Electrical Measurement Geometries

The electrical resistance of the samples was measured either in two terminal or four terminal configuration, depending on the sample geometry. A disadvantage of the two-terminal measurements is that the obtained resistance contains the contact resistance in addition to the sheet resistance:

$$R_{2T} = R_{C1} + R_{C2} + R_{sheet} \quad (4.3)$$

In order to attain the true resistance of the material it is necessary to implement four terminal measurement method to subtract the contact resistances. Since the voltage drop is measured using a voltmeter and no current is flowing through it, the contact resistances won't contribute in the resistance measurements. A simple way to estimate the contact resistances is to subtract the two-terminal from the four-terminal resistance.

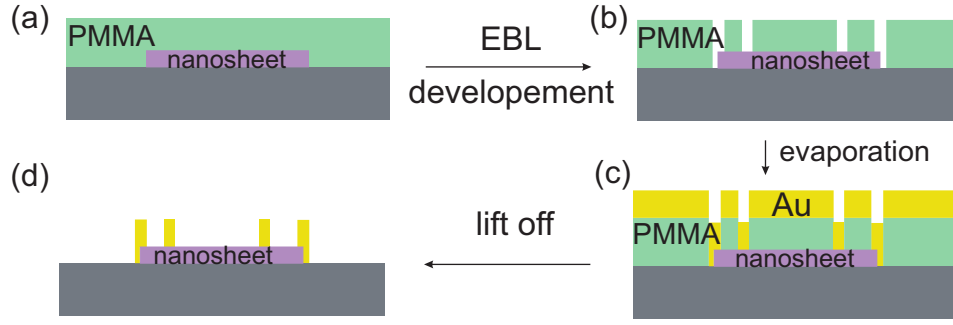


Figure 4.9 – electron beam lithography steps (a) spin coating the substrate (b) defining the electrode area using EBL and developing (c) evaporation of metals and (d) lift off of the metal evaporated.

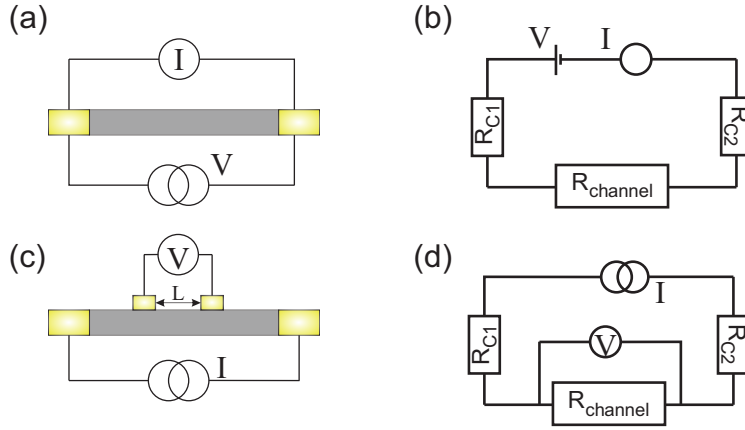


Figure 4.10 – (a) and (b) Two terminal configuration and its equivalent electrical circuit including the contact resistances, respectively. (c) and (d) four terminal configuration excluding the contact resistances and measures the resistance of the channel between the voltage electrodes.

4.11 Magnetoresistance Measurements

Valuable information about the electronic properties of a quantum material can be gained from the magnetic field-dependent resistivity. Two different contact geometries were used to measure magnetoresistance of the nanosheets under study. The first one is the standard Hall bar geometry which allows the simultaneous measurement of the longitudinal and Hall resistance of the device. The determination of the longitudinal resistance is based on the same principle as the above described four-terminal measurements, while the Hall resistance is measured with the aid of the opposite electrodes across the Hall bar, as depicted in Figure 4.11a. Accuracy of the resistivity measurements is sensitive to the geometry of the Hall bar. One

important geometrical error in Hall bar samples is the tendency of the end contacts to short out the Hall voltage. To reduce this error to less than 1%, the aspect ratio of the sample length to width should be larger than 3.[50] The Hall resistance can be calculated from the voltage measured between the opposite electrodes divided by the current passing through the bar, $R_{xy} = \frac{V_H}{I}$.

The other contact geometry widely used to probe the magnetoresistance of nanosheets is the van der Pauw geometry. The main advantage of the van der Pauw method over the Hall bar geometry is the freedom of choice over the geometry of the sample. Thus, time consuming additional etching steps can be avoided which are otherwise needed to obtain a suitable Hall bar geometry. The conductivity of the sample in van der Pauw geometry is obtained from:[51]

$$e^{-\pi R_{PQ,RS}\sigma_{xx}} + e^{-\pi R_{QR,SP}\sigma_{xx}} = 1 \quad (4.4)$$

and the Hall resistivity can be simply calculated by:

$$\rho_{xy} = \frac{R_{PR,QS}(B) - R_{PR,QS}(0) + R_{QS,RP}(B) - R_{QS,RP}(0)}{2} \quad (4.5)$$

in which the points P, Q, R and S are four arbitrary edges of the sample.

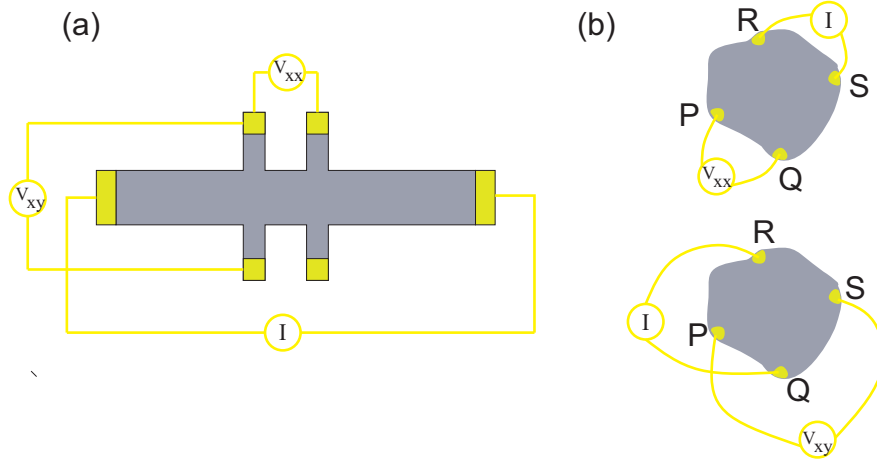


Figure 4.11 – (a) Hall bar geometry for measuring R_{xx} and R_{xy} , (b) Van der Pauw geometry for measuring R_{xx} and R_{xy} of a non geometric sample.

5 Electronic Transport Study of Topological Insulators

5.1 Growth of Single Component Topological Insulators

The surface states of TIs have been detected in angle-resolved photoemission spectroscopy (ARPES) revealing the Dirac cone of the topologically protected surface states. By contrast, probing the surface states by electrical transport experiments has remained a challenge, as the typically strong doping of the material leads to a pronounced conductivity contribution of its bulk states. Among the methods to reduce the bulk contribution are electrostatic gating, chemical doping, alloying and also increasing the surface-to-bulk ratio. In this thesis two strategies are used, one is making thin sheets of topological insulators and the other is alloying them to reduce the vacancies which have caused the extra carrier generations. The materials of choice here are $\text{Bi}_2\text{Te}_2\text{Se}$ (BTS) as n-type and Sb_2Te_3 as p-type TI. For both materials, ARPES measurements have confirmed the existence of Dirac cones.[52, 53] The CVD grown BTS and Sb_2Te_3 nanosheets were characterized by low temperature electrical transport measurements. Figure 5.1 shows exemplary AFM images and Raman spectra of as-grown BTS and Sb_2Te_3 nanoplatelets.

Depending on the growth time and conditions (see chapter 4) nanoplatelets with different thicknesses and geometries were obtained. Raman spectroscopy is a valuable tool to examine nanoplatelets' vibrational properties. Symmetry group analysis of BTS yields the following irreducible vibrational representation:[54]

$$\Gamma_{vib} = 2A_{1g} + 2E_g + 2A_{2u} + 2E_u \quad (5.1)$$

Among the allowed vibrational modes, the A_{1g} and E_g modes are Raman active, whereas the A_{2u} and E_u modes are infrared active along the c axis and the a-b planes, respectively. The Raman spectrum of BTS displays two isolated modes at 65 cm^{-1} and 109.5 cm^{-1} corresponding to A_{1g} and E_g modes, respectively. In addition, there are two overlapping peaks at 140 cm^{-1} and 155 cm^{-1} with A_g symmetry. While the origin of 140 cm^{-1} peak is somewhat controversial it is commonly attributed to anti-site defects.[55]

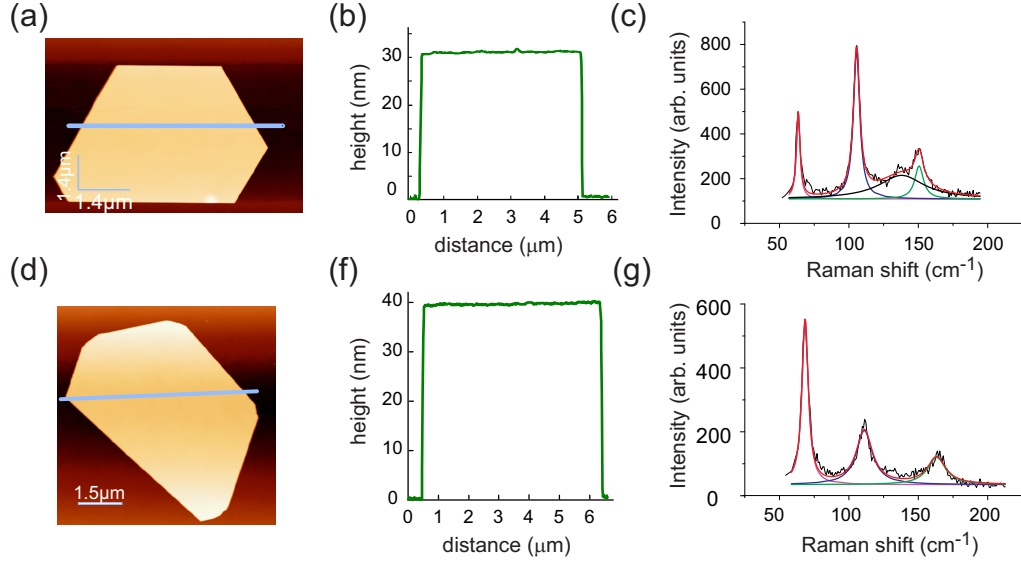


Figure 5.1 – (a) and (d) AFM images (b) and (e) the height profile across the blue line in indicated in AFM image (c) and (f) the Raman spectrum taken using a 532 nm laser light at ambient conditions for typical BTS and Sb_2Te_3 nanosheets, respectively.

5.2 Magnetotransport of Single Component Topological Insulators

The surface states of TIs can be probed by magnetotransport measurements. The topologically protected surface states are expected to give rise to the weak antilocalization (WAL) effect due to their spin orbit locking character. The magnetoresistance of BTS and Sb_2Te_3 nanoplatelets was determined using either the van der Pauw method, or Hall bar geometry whenever possible by the sample geometry. For BTS nanosheets grown on SiO_2/Si substrates a Hall mobility on the order of 100 to 200 cm^2/Vs and a carrier density on the order of 10^{-19} cm^{-3} is measured at 1.4 K. The sign of Hall resistance clearly indicates n-type doping of the grown BTS nanoplatelets. An analytical expression to describe the localization effect in 2D diffusive systems has been derived by Hikami, Larkin and Nagaoka (HLK model) as:[56]

$$\Delta\sigma(B) = \alpha \frac{e^2}{h} \left[\ln\left(\frac{B_\phi}{B}\right) - \psi\left(\frac{1}{2} + \frac{B_\phi}{B}\right) \right] \quad (5.2)$$

where ψ is the digamma function, $l_\phi = \sqrt{D\tau_\phi}$ is the phase coherence length and $B_\phi = \frac{h}{4el_\phi^2}$. The value of the constant α assumes a value of 0 in the case of strong magnetic scattering centers, 1 for the weak localization and -0.5 for the case of weak antilocalization. Figure 5.2a-c shows the magnetoresistance of a typical BTS nanoplatelet with a thickness of 10 nm. The plot of R_{xx} vs magnetic field exhibits a clear antilocalization cusp. From fits according to the HLK model, a value of -0.513 in good proximity to the value expected for a topological insulator is extracted. However, generally this value varies between -0.3 to -0.7. Magnetoresistance

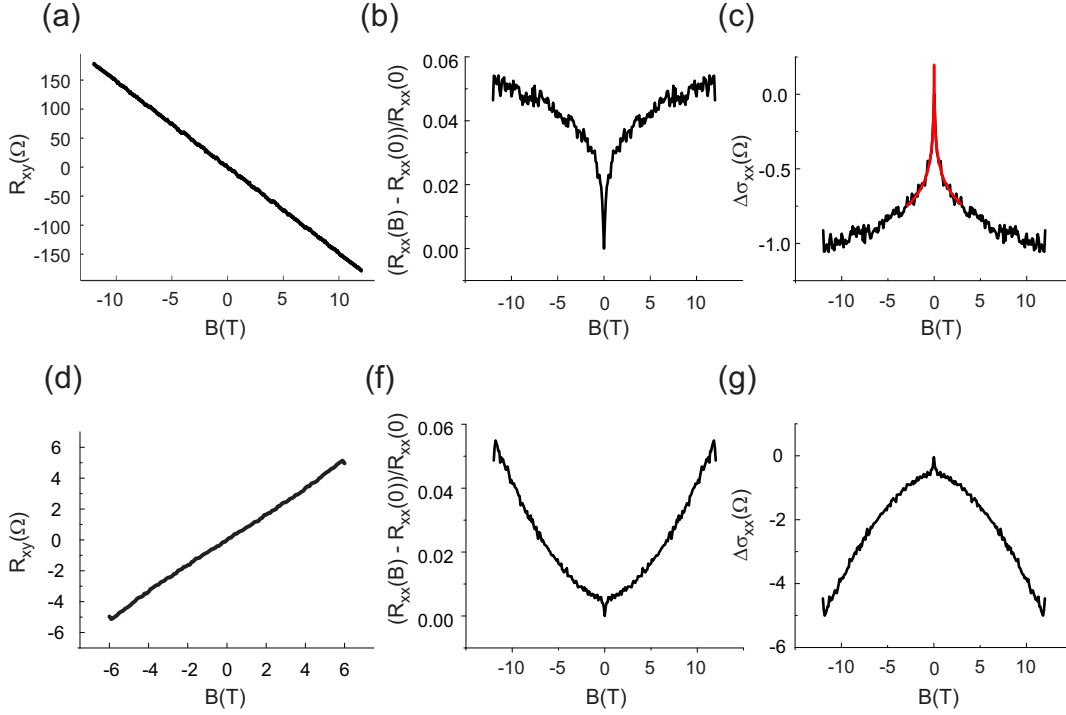


Figure 5.2 – (a) and (d) Hall resistance (b) and (e) the relative magnetoresistance (c) and (f) $\Delta\sigma_{xx}$ vs magnetic fields for BTS and Sb_2Te_3 nanosheets respectively.

measurements were also performed on the binary topological insulator Sb_2Te_3 nanoplatelets of the similar thickness of 10 nm (see Figure 5.2d-g). From the Hall measurements a carrier density of $7.1 \cdot 10^{20} \text{ cm}^{-3}$ is calculated showing higher doping of this material in comparison to ternary compound BTS. Also the mobility is substantially lower than the mobility of BTS, i.e., about $30 \text{ cm}^2/\text{Vs}$. Moreover the sign of the Hall resistance verifies the p-doping character of Sb_2Te_3 . The Hall measurements furthermore revealed a non-linear R_{xy} vs. B-field (see Figure 5.2d) pointing toward two channel contribution to the conductivity.

5.3 Magnetotransport of TIs Grown on hBN

The structural quality of the material grown by CVD is strongly dependent on the type of substrate. In complementary measurements, with the aim of reducing the defect density in BTS and Sb_2Te_3 , they are grown on the exfoliated hBN nanosheets. BTS consists of close-packed atomic layers of five atoms (quintuple layer) arranged along the c-axis. The alignment of the BTS layers on hBN layered crystal structure yields a lattice mismatch of about 1.5%. For the BTS nanoplatelets on hBN, significantly enhanced carrier mobility was found in comparison to BTS grown on SiO_x/Si . This reflects the smoother lattice match of hBN as a growth substrate. Owing to the enhanced mobility, it became possible to observe the so-called

Shubnikov de Haas oscillations in the magnetic field dependence of R_{xx} , as described in detail in the next subsection.

5.3.1 Shubnikov-de Haas Oscillations

Electrons in a 2D electron gas in the presence of a perpendicular magnetic field will have quantized cyclotron orbits. By analogy of a classical picture, the electrons can be visualized as waves that propagate around a circle and interfere with themselves, leading to quantization of the orbits. However, a proper insight can be gained by solving the Schrödinger equation. The effective mass Hamiltonian for an electron in the presence of a magnetic field reads:

$$H = \frac{(\mathbf{p} + e\mathbf{A})^2}{2m^*} + V(z) \quad (5.3)$$

where $V(z)$ is a confinement potential restraining the electrons in the volume of the material. Assuming a magnetic field in the z direction $B = (0, 0, B)$ with the vector potential $A = (-By, 0, 0)$, the Hamiltonian in the z direction will be

$$H_z = -\frac{\hbar^2}{2m^*} \frac{\partial^2}{\partial z^2} + V(z) \quad (5.4)$$

which is independent of the magnetic field. In the xy -plane the Hamiltonian has the form

$$H_{xy} = \frac{(p_x - eB_z y)^2 + p_y^2}{2m^*} \quad (5.5)$$

which contains the magnetic field and is independent of the confinement potential. The eigenvalues in the plane can be derived using the *Ansatz*[51]

$$\psi(x, y) = e^{ik_x x} \eta(y) \quad (5.6)$$

which leads to the eigenvalue equation of the form of a 1D quantum mechanical harmonic oscillator,

$$\left[\frac{p_y^2}{2m^*} + \frac{1}{2} m^* \omega_c^2 \left(y - \frac{\hbar k_x}{eB_z} \right)^2 \right] \eta(y) = E \eta(y) \quad (5.7)$$

with $\omega_c = eB/m^*$ as the cyclotron frequency. As apparent from equation 5.7 the k_x -dependent center coordinate is

$$y_0 = \frac{\hbar k_x}{eB} \quad (5.8)$$

and the eigenenergies are,

$$E_n = \hbar \omega_c \left(n + \frac{1}{2} \right) \quad (5.9)$$

independent of k_x . An important implication of equation 5.9 is that the states of different quantum number k_x but same quantum number n , are energetically degenerate. These states are called Landau levels. The energy of the Landau levels according to the equation 5.9

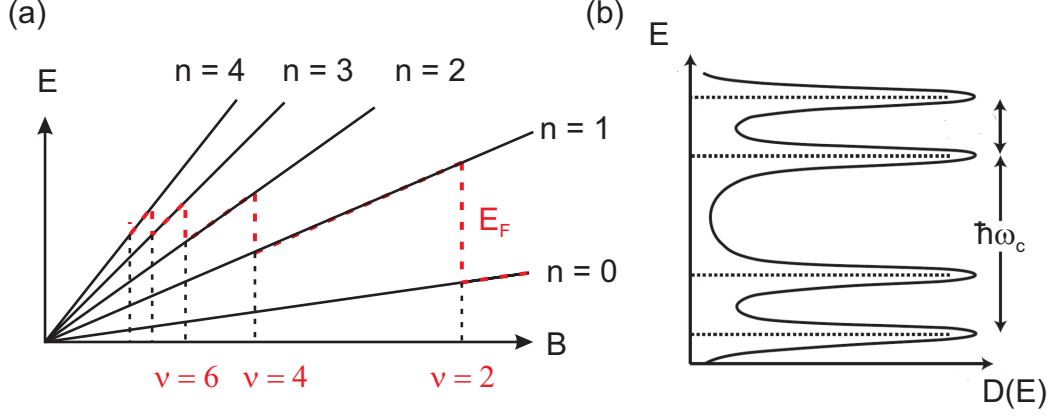


Figure 5.3 – (a) Landau fan diagram, showing the energy levels for electrons in a magnetic field and (b) density of states for electrons in a magnetic field, broadened in the presence of the scattering centers.

increases with increasing the magnetic field leading to the formation of the so-called Landau fan, as depicted in Figure 5.3a. The degeneracy of a Landau level can be determined based upon the information about the center coordinate y_0 and the fact that it should be in the width of the 2D electron gas, $0 \leq \hbar k_x / eB \leq W$. The density of k_x states in a 2D electron gas of length L is $L/2\pi$; as a result the allowed k_x values obey the relation $0 \leq k_x L / 2\pi \leq eB / hA$ with $A = WL$ being the sample area. Consequently, the number n_L of allowed states per unit area is,

$$n_L = \frac{eB}{h}. \quad (5.10)$$

For a 2D electron gas with the electron density of n_s in a given magnetic field, the integer $\nu = n_s / n_L$ indicates the number of the Landau levels that are filled at zero temperature. The value, $\nu = \hbar n_s / eB$ is called the filling factor corresponding to the magnetic field B . The Fermi energy of a 2D electron gas with density of state of n_s oscillates with ν with a period of $1/B$. If the Zeeman splitting is negligible in comparison to the Landau level splitting, $\hbar\omega_c$, each level will be doubly degenerate and the Fermi level jumps between Landau levels of even numbers. However, in real samples the degeneracy of the Landau levels is lifted by spatial potential fluctuations arising from the scattering centers. The scattering limits the lifetime of the electrons in a certain Landau level, leading to the broadening of the states as illustrated in Figure 5.3b.

It was shown by Tsuneya Ando in 1974 that the envelope function of the oscillation in resistance

(R_L) is well described in terms of,[57]

$$\frac{\Delta R_{xx}(T)}{R_{xx}(0)} = \frac{4\lambda(T)}{\sinh(\lambda(T))} e^{\frac{-\pi}{\omega_c \tau_Q}}, \lambda(T) = \frac{2\pi^2 K_B T}{\hbar e B} m_{cyc} \quad (5.11)$$

the so-called Ando formula. Here, τ_Q is the total scattering time and ΔR_{xx} is the difference between R_0 and R_L at the resistance oscillation extrema. Using equation 5.11, information about the effective mass and scattering time of the 2DEG can be gained.

5.3.2 Magnetotransport of BTS on hBN

In Figure 5.4a, the sheet resistance of a 10 nm thick BTS nanoplatelet on hBN is shown as a function of perpendicular B-field at base temperature. At higher B-fields, pronounced SdH oscillations become visible. The oscillatory nature of the MR with period of $1/B$ is illustrated in Figure 5.4b for different temperatures.

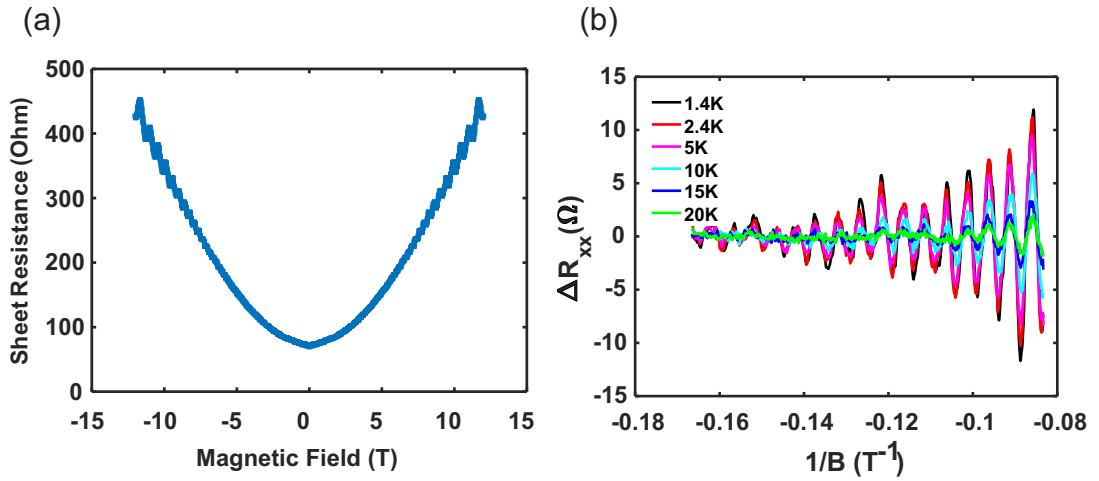


Figure 5.4 – (a) Sheet resistance of BTS/hBN nanosheet revealing prominent Shubnikov de Haas oscillations at $B = 10$ T, (b) the ΔR_{xx} vs inverse of the magnetic field indicating the periodic nature of this oscillation.

The values of $1/B$ for the extrema in Figure 5.4 b can be assigned to different filling factors. Figure 5.5a shows the corresponding plot together with the filling factor assignment. Using the formula $\Delta v = \frac{\hbar n}{e} \cdot \Delta \frac{1}{B}$ a surface carrier density of $n_{2D} = 4.4 \cdot 10^{16} \text{ cm}^{-2}$ is obtained. The relation between the Fermi surface area and the carrier density in the presence of a magnetic field can be expressed by,[58]

$$2\pi n = A_F \frac{\hbar}{eB}, A_F = \pi K_F^2 \quad (5.12)$$

Using the plot in Figure 5.5a and the above equation, the value of $K_F = 0.075 \text{ \AA}^{-1}$ is obtained. To further calculate the Fermi velocity, the information about the cyclotron mass is needed, as apparent from

$$v_F = \frac{\hbar K_F}{m_{cyc}}. \quad (5.13)$$

The cyclotron mass can be gained using the temperature smearing factor in Ando formula by evaluating the amplitude of the resistance oscillations at different temperatures. The resulting plot in Figure 5.14b yields the value of $m_{cyc} = 0.2m_0$.

The scattering time of a 2DEG is accessible from the logarithmic form of equation 5.11,

$$\ln\left(\frac{\Delta R}{R_0} \cdot \frac{\sinh \lambda}{4\lambda}\right) = -\frac{\pi}{\omega_c \tau} \frac{1}{B}. \quad (5.14)$$

The dependence of $\ln\left(\frac{\Delta R}{R_0} \cdot \frac{\sinh \lambda}{4\lambda}\right)$ vs. $1/B$ is called Dingle plot.[51] The Dingle plot in Figure 5.5c yields the scattering time $\tau = 80 \text{ fs}$.

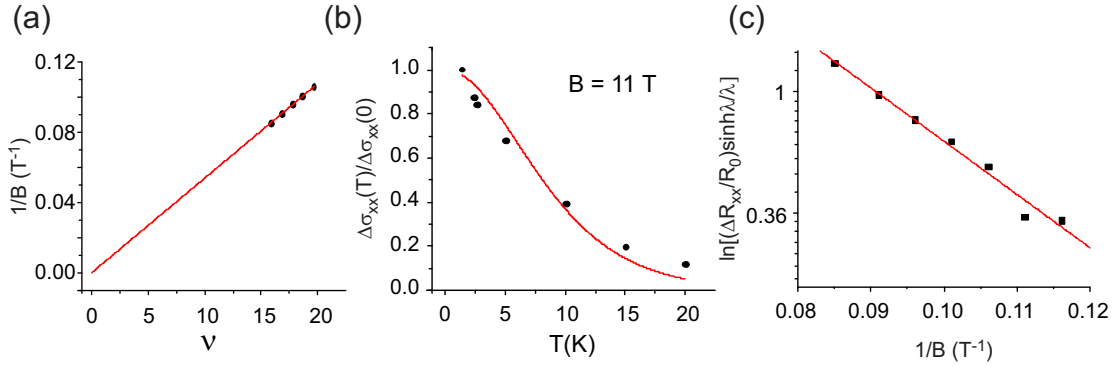


Figure 5.5 – (a). The indices of magnetoresistance minima are plotted on the horizontal axis, the corresponding values of $1/B$ are plotted on the vertical axis. The slope of the line $2|e|/\hbar n$ determines the electron density. (b) Ando plot for different temperatures at 11 T, (c) the Dingle plot, yielding a quantum scattering time of 80 fs.

Since the mobility and the scattering time are closely related through the relation $\mu = e\tau/m^*$, the surface carrier mobility of $700 \text{ cm}^2/\text{Vs}$ is calculated. Remarkably, the bulk carrier mobility, as determined from the Hall measurements, is $\mu = 17170 \text{ cm}^2/\text{Vs}$, much larger than for the case of BTS grown directly on SiO_x/Si substrates.

Figure 5.6 a and b demonstrate that the as-grwon BTS/hBN nanosheets can be electrostatically gated. The nonlinearity of the Hall resistance arises from the contribution of the different bands in the conduction (i.e., bulk and surface states).

Similar measurements were done on the nanosheets of Sb_2Te_3 grown on hBN, See Figure 5.7a and b. While the mobility of Sb_2Te_3 on SiO_x/Si was found to normally be in the order of tens of $\text{cm}^2\text{V/s}$, the Sb_2Te_3 on hBN sheets reached significantly larger values of hundreds of $\text{cm}^2\text{V/s}$.

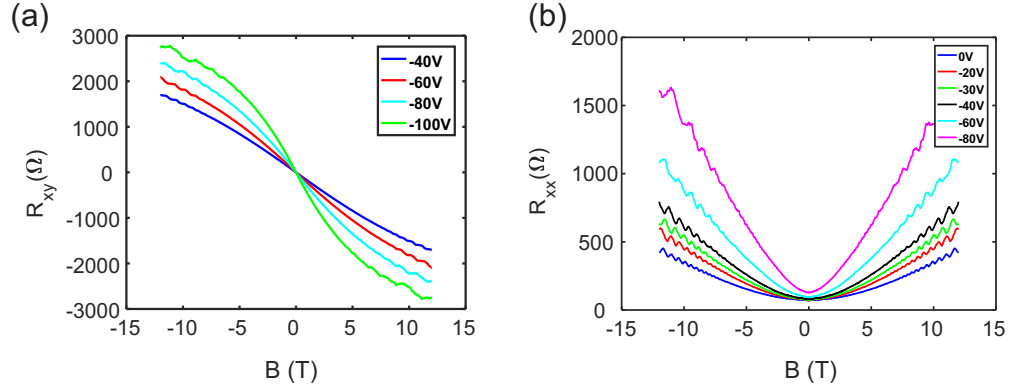


Figure 5.6 – (a) Hall (R_{xy}) and (b) longitudinal (R_{xx}) resistance vs magnetic field of BTS/hBN nanoflakes for different gating values.

However, this increase in mobility was still insufficient for the emergence of SdH oscillations.

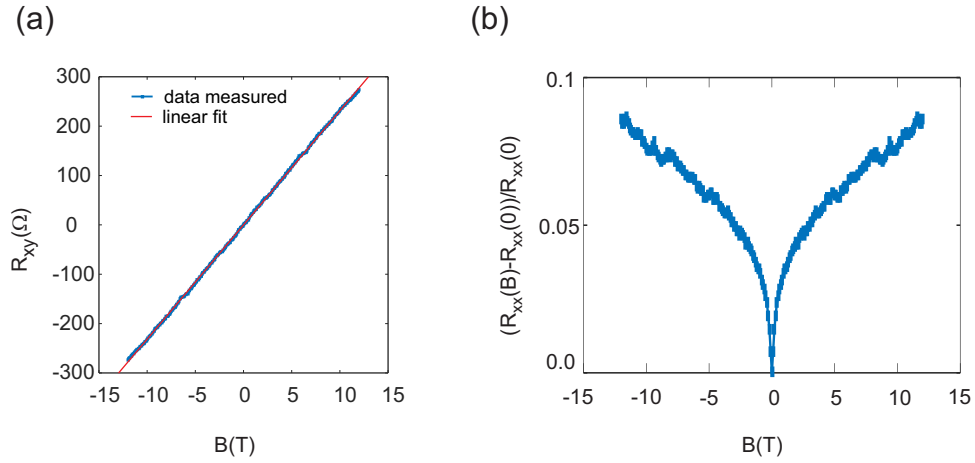


Figure 5.7 – (a) Hall (R_{xy}) and (b) relative longitudinal $(R_{xx}(B) - R_{xx}(0))/R_{xx}(0)$ resistance vs. magnetic field of Sb_2Te_3 /hBN nanoflakes, showing a pronounced WAL cusp.

5.3.3 Magnetotransport of Lateral Heterojunctions

Besides the single component TI nanoplatelets, also the magnetotransport behavior of the lateral BTS/ Sb_2Te_3 heterostructures was investigated. This behavior is of interest, since according to theory the presence of the p-n junction may generate a topologically protected 1D electronic state at the interface between the two components.[59] However, these measure-

ments provided only little new insights. The resistance across the junction in dependence of an external perpendicular B-field showed for all investigated samples a pronounced WAL cusp. As another observation, the two-terminal magnetoresistance turned out to be dependent on

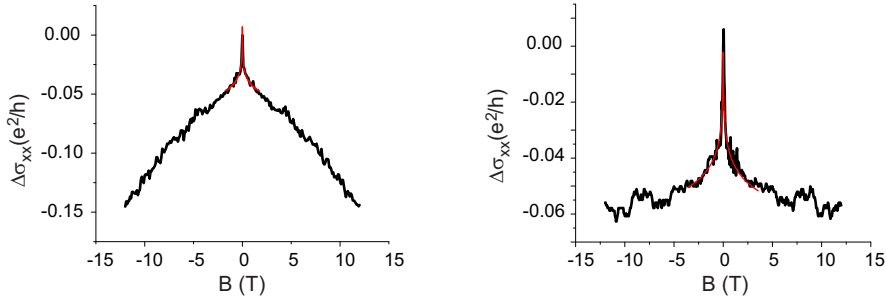


Figure 5.8 – The magnetoresistance of the same heterostructure measured in two different electrode arrangements.

the chosen electrode combination. This dependence may be due to the various electron paths through the junction being influenced by different scattering effects. Furthermore, in Hall measurements R_{xy} changed sign from sample-to-sample, indicating that the relative carrier concentrations in the BTS and Sb_2Te_3 components depend sensitively on the CVD growth conditions.

6 Scanning Photocurrent Microscopy of Lateral TI Heterostructures¹

Direct heat-to-electricity conversion has attracted great interest because the conventional energy resources are rapidly depleted and it is necessary to find more effective ways to utilize the energy available. In this sense, thermoelectricity is highly promising since it can use huge amount of otherwise wasted energy and convert it into electricity. Consequently, there is an intense effort to develop and identify efficient thermoelectric materials which can be used in a wide range of applications. Interestingly the chalcogenide binary and ternary materials such as Bi_2Te_3 , Sb_2Te_3 and $\text{Bi}_2\text{Te}_2\text{Se}_3$ compounds are among the best thermoelectric materials. Toward their device implementation, benefit can be taken from recent advances in the fabrication of novel nanomaterials and their heterostructures. An additional impetus stems from the recent development of novel types of photodetectors and photovoltaic devices which effectively convert photons to electrical currents. [60]

Compared with traditional 3D photonic materials such as gallium arsenide (GaAs) and silicon (Si), 2D materials exhibit many interesting properties. The first point is that quantum confinement in the direction perpendicular to the 2D plane leads to novel optoelectronic features, distinct from their 3D counterparts.[60, 61] Secondly, the 2D materials are suitable for integration in applicable optoelectronic devices such as waveguides and cavities.[62, 63] Moreover, it is possible to make heterostructures of 2D materials using stacking techniques without being worried about the lattice mismatching. Another issue is that although 2D materials are thin, they can nevertheless strongly interact with light. There are two major mechanisms which lead to photocurrent (PC) generation, as depicted in Figure 6.1. In semiconductors, this mainly occurs via the separation of the excited electron-hole pair by a built-in electric field, which corresponds to the so-called photovoltaic effect (Figure 6.1a and c). Another possible mechanism is photothermoelectric effect PTE. If a temperature gradient is generated by light

¹Parts of this chapter are based on our publication "Efficient Photothermoelectric Conversion in Lateral Topological Insulator Heterojunctions", publication 2 in Curriculum Vitae (page 97).

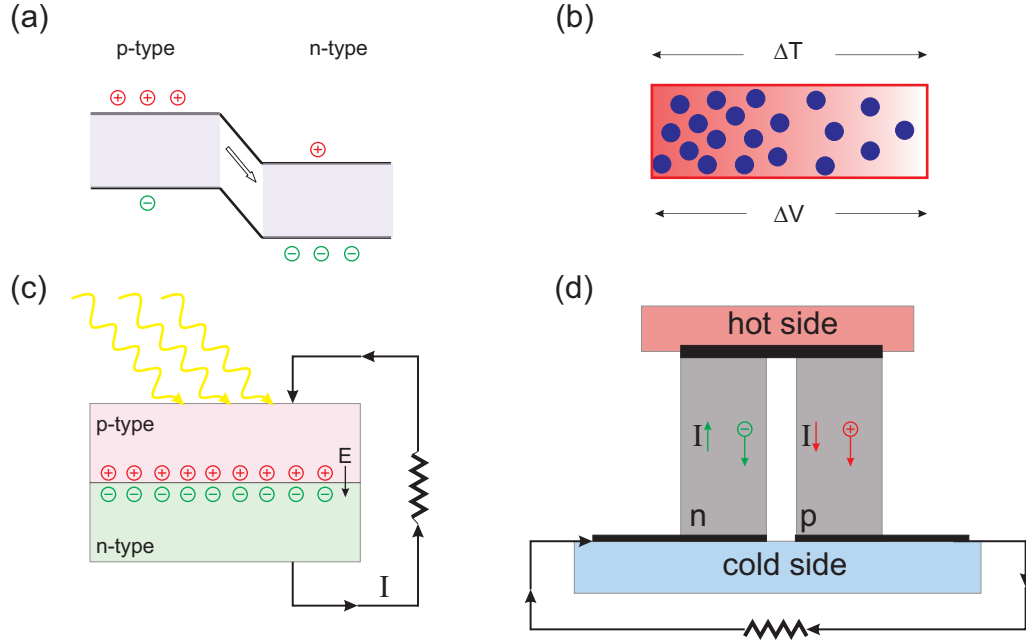


Figure 6.1 – (a) and (b) schematic of photocurrent generation mechanism in a semiconductor junction and a thermoelectric material. (c) and (d) Schematic of simple devices working with photovoltaic and thermoelectric concepts respectively.

across an interface between two materials of different thermoelectric power (S) the PC will be generated by photothermoelectric (PTE) effect. The underlying mechanism can be understood in terms of different population of electrons at the hot and cold sides of the structure leading to a voltage drop across the sample (Figure 6.1b and d). Practical devices normally are made of a number of thermocouples connected electrically in series and thermally in parallel. [64] Thermoelectric performance is typically quantified in terms of dimensionless figure of merit ZT defined as:[64]

$$ZT = \frac{S^2 \sigma T}{\kappa} \quad (6.1)$$

where S is the Seebeck coefficient or thermopower, σ is the electrical conductivity, T is the absolute temperature and κ the thermal conductivity. The Seebeck coefficient is in principle a measure of the magnitude of an induced thermoelectric voltage ΔV in response to an applied temperature difference ΔT expressed as,

$$S = \frac{\Delta V}{\Delta T} \quad (6.2)$$

Microscopically, in a conductor the Seebeck coefficient is expressed by the Mott relation,[65]

$$S = \frac{\pi^2}{3} \left(\frac{k_B}{q} \cdot k_B T \right) \frac{d(\ln[\sigma(E)])}{dE} \Big|_{E=E_F} \quad (6.3)$$

It shows that Seebeck coefficient is inversely dependent on the electrical conductivity. However, equation 6.1 indicates that the figure of merit has a direct dependency on the conductivity. This leads to an inherent problem in this field, meaning that a fine balance between these two dependencies is needed to achieve an optimal figure of merit. The Mott formula also indicates that the Seebeck coefficient primarily depends on the energy derivative of the density of states at the Fermi level. Any technique or material which increases this slope will enhance the Seebeck coefficient.[66] A major hurdle for a systematic optimization is the often highly nontrivial dependence of the material's electronic structure on its atomic structure. Several successful concepts, including nanostructuring and inclusion of loosely bound rattlers have been developed to systematically reduce the lattice thermal conductivity. Well-established thermoelectric materials such as Bi_2Te_3 display a large Seebeck coefficient of up to $150 \mu\text{V/K}$ at room temperature. Interestingly, they belong to the material class of three-dimensional (3D) topological insulators (TIs). TIs share several common features with topologically trivial thermoelectric materials, including the presence of heavy elements which impart strong spin-orbit coupling, and a small bulk band gap. Bi_2Te_3 has been known to be an excellent thermoelectric material and routinely used in devices.[65] Theory suggests that hybridization between the nontrivial (helical) surface states from the top and bottom surfaces of a 3D TI induces a band gap in the surface states which can enhance the thermoelectric performance by controlling the conductivity.[67] A positive impact of the gapped topological surface state on the thermoelectric transport has been corroborated by ab initio electronic structure calculations on Sb_2Te_3 . [68]

Experimentally, various types of 3D TI nanostructures have been investigated with respect to their thermoelectric performance. Along these lines, scanning photocurrent microscopy (SPCM) of step-terraced two-dimensional (2D) crystals of Bi_2Te_3 and Sb_2Te_3 has revealed thermoelectric conversion at monolayer steps of the same material by exploiting of the quantum nature of the material.[69] This observation has been attributed to the different derivative of the density of states at steps with different number of layers. In addition, it has been experimentally demonstrated that the excitation of spin-polarized currents by circularly polarized light leads to an enhancement of the photothermoelectric effect in Bi_2Se_3 nanoribbons.[70] Supporting evidence for the role of the spin-helical surface states in 3D TIs has recently been gained for ultrathin sheets of $(\text{Bi}_x\text{Sb}_{1-x})_2\text{Te}_2$, which display an enhanced spin Seebeck effect signal.[71] It has furthermore been demonstrated that the thermoelectric performance of ultrathin Bi_2Se_3 nanosheets can be optimized through thickness control and reducing the thermal conductivity.[72]

Although sufficient evidence on promising thermoelectric conversion efficiency of single-component 3D TI nanostructures is provided, photothermoelectric devices implementing the corresponding n- and p-type components at the nanoscale have not yet been realized. Experimentally, lateral and vertical TI p-n heterostructures have been successfully fabricated by

molecular beam epitaxy[73], solvothermal synthesis[74] or vapor phase growth[75], however only their general electrical properties have been studied.

In this chapter the photo-thermoelectric response of individual lateral heterostructures composed of two different 3D TIs, specifically $\text{Bi}_2\text{Te}_2\text{Se}$ (BTS) as n-type component and Sb_2Te_3 as the p-type component is investigated.

6.1 Structural and Compositional Analysis

In the BTS crystal, ordered hexagonal Te-Bi-Se-Bi-Te quintuple layers are stacked via van der Waals interactions, while Sb_2Te_3 is made of stacked quintuple layers of Te-Sb-Te-Sb-Te. The two tetradymite materials share the rhombohedral crystal structure of the same space group $R\bar{3}m$ rendering them suitable candidates for fabricating lateral TI heterojunctions.[27]

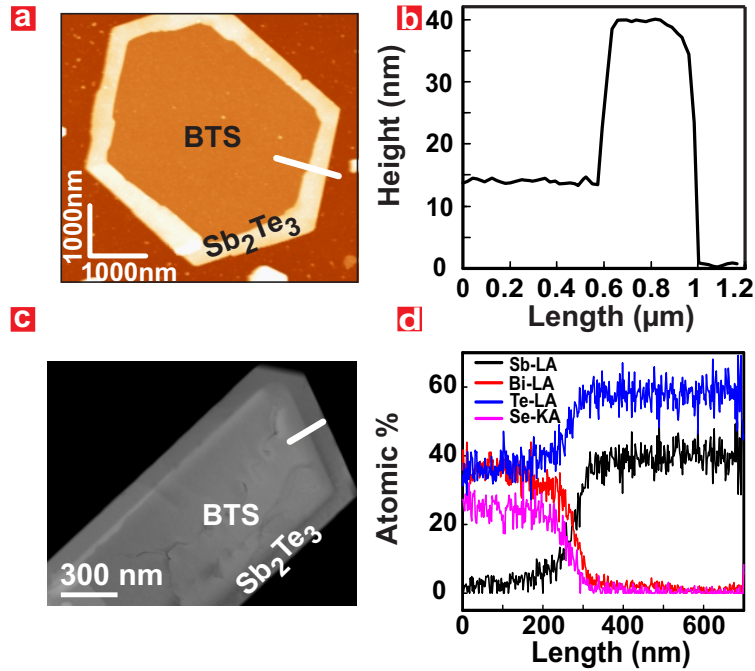


Figure 6.2 – (a) Topographic AFM image of a lateral $\text{Bi}_2\text{Te}_2\text{Se}/\text{Sb}_2\text{Te}_3$ heterostructure, obtained by two consecutive vapor solid growth steps. The central $\text{Bi}_2\text{Te}_2\text{Se}$ nanoplatform is surrounded by a significantly higher frame of Sb_2Te_3 . (b) Cross-sectional profile along the white line in the AFM image of panel a. (c) Overview TEM image of a $\text{Bi}_2\text{Te}_2\text{Se}/\text{Sb}_2\text{Te}_3$ nanoplatform. (d) Corresponding EDX profiles for Sb, Bi, Te, and Se, taken across the $\text{Bi}_2\text{Te}_2\text{Se}/\text{Sb}_2\text{Te}_3$ interface along the white line in panel c.

The CVD growth of lateral TI heterostructures is described in detail in chapter 3 (see section 3.3). An exemplary atomic force microscopy (AFM) image of a heterostructure comprising BTS and Sb_2Te_3 regions of notably different thickness is shown in Figure 6.2a. The line profile in Figure 6.2b indicates that the central platform has a thickness of 15 nm which is surrounded by a ~40 nm thick frame region of Sb_2Te_3 . The edge growth mechanism was further confirmed

by AFM characterization of individual BTS nanoplatelets before and after Sb_2Te_3 growth. After the growth of Sb_2Te_3 , the AFM measurements revealed that the thickness of BTS is largely preserved, signifying an edge-induced growth mechanism for the Sb_2Te_3 .

To further study the composition of the as-grown lateral heterostructures, transmission electron microscopy (TEM)-based energy dispersive X-ray (EDX) analysis is done as exemplified for the nanoplatelet in Figure 6.2c. The grown TI heterostructure are first transferred via a water transfer method on to a TEM grid. The SiO_x/Si growth substrates with grown TI heterostructures on were spin coated and were put in distilled water of 90°C temperature. After about one hour the hydrophobic PMMA can be easily removed and transferred on a TEM grid. The PMMA is subsequently dissolved with Acetone. Figure 6.2c shows such a TEM measurement and the corresponding EDX line profiles across the interface between the two regions of different thickness (Figure 6.2d) show that Bi is present only in the central region, whereas Sb exists only in the outer frame reaching almost zero atomic percentage in the center.

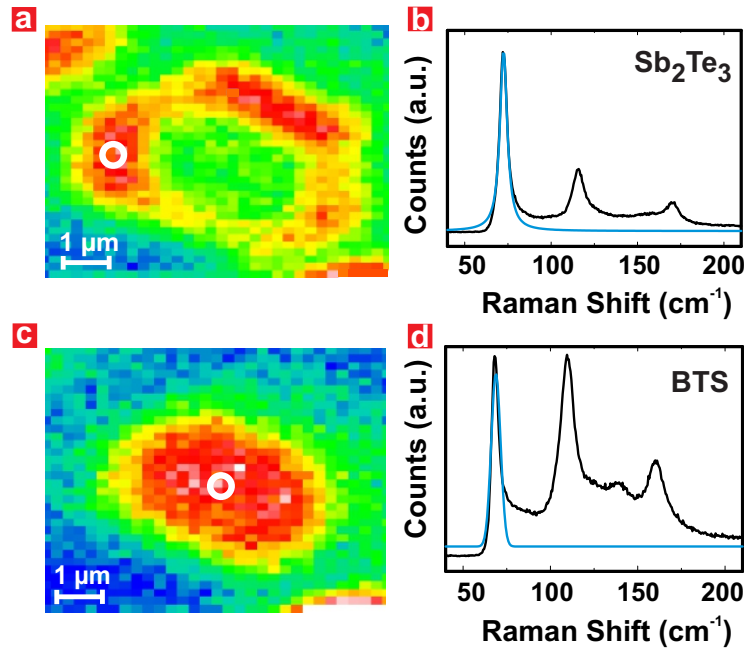


Figure 6.3 – (a) Raman map of a lateral $\text{BTS}/\text{Sb}_2\text{Te}_3$ heterostructure, displaying the scattered intensity at $\sim 71 \text{ cm}^{-1}$ associated with the A_1g^1 mode of Sb_2Te_3 . (b) Raman spectrum recorded at the position marked in panel a, which lies within the Sb_2Te_3 region at the periphery. The blue line is the Lorentzian fit of the lowest energy peak. (c) Raman map of the same nanoplatelet as in panel a, displaying the scattered intensity at $\sim 65 \text{ cm}^{-1}$ belonging to the A_1g^1 mode of $\text{Bi}_2\text{Te}_2\text{Se}$. (d) Raman spectrum collected from the center of $\text{Bi}_2\text{Te}_2\text{Se}$ region of the heterostructure (open circle). The blue line is a Lorentzian fit of the lowest energy peak. All of the above maps and spectra were acquired under ambient conditions with $\lambda = 514 \text{ nm}$.

The heterostructure composition could be further probed by confocal Raman spectroscopy (Figure 6.3). To this end the whole area of the TI heterostructure is scanned at room temperature and at each point the Raman spectrum is recorded. The Raman spectrum of BTS

consists of two isolated modes at 65 cm^{-1} and 109.5 cm^{-1} corresponding to A_{1g} and E_g modes, respectively. In addition, there are two overlapping peaks at 140 cm^{-1} and 155 cm^{-1} associated with A_{g2} mode. The Sb_2Te_3 Raman spectrum shows three peaks at 71 cm^{-1} , 115 cm^{-1} and 168 cm^{-1} , which can be assigned to the A_{1g} , E_g , A_{1g2} vibrational modes, respectively. To analyze the composition of the heterostructure, the final Raman map is plotted for the prominent peaks of the two materials. Raman maps depicted in Figure 6.3 show that the A_{1g} mode characteristic of Sb_2Te_3 (peak at $\sim 71\text{ cm}^{-1}$, see the spectrum in Figure 6.3b) appears predominantly within the frame region, while the corresponding mode belonging to BTS (peak at $\sim 65\text{ cm}^{-1}$, see Figure 6.3d) resides within the central region.

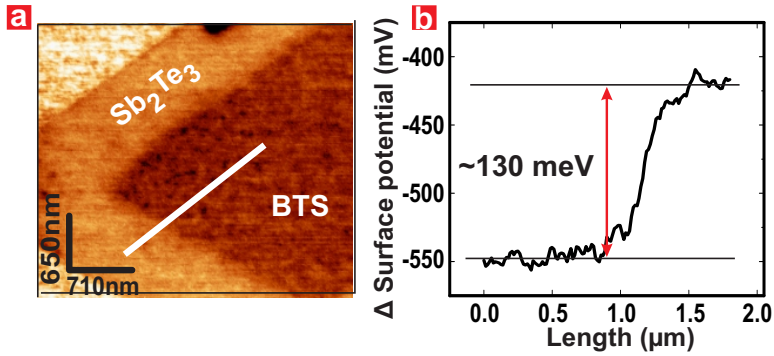


Figure 6.4 – (a) Kelvin probe force microscopy image of the periphery of a $\text{Bi}_2\text{Te}_2\text{Se}/\text{Sb}_2\text{Te}_3$ nanoplatelet. The image was taken under ambient conditions. (b) Corresponding surface potential profile along the white line in panel a. The starting point belongs to the right end of the line.

In addition, indirect proof for the chemical composition of the heterostructures was obtained by Kelvin probe force microscopy (KPFM) described in chapter 3, as illustrated in Figure 6.4. The line profile in Figure 6.4b along the white line in the KPFM image in Figure 6.4a, indicates a surface potential difference of $\sim 130\text{ mV}$ between the inner BTS and the outer Sb_2Te_3 region. The work function of BTS ($\sim 5.2\text{ eV}$ [76]) exceeds that of Sb_2Te_3 ($\sim 4.6\text{ eV}$ [77]), accordingly a lower surface potential is detected on the Sb_2Te_3 area surrounding the inner BTS.[78]

6.2 Electrical Characterization

For electrical characterization, individual $\text{BTS}/\text{Sb}_2\text{Te}_3$ nanoplatelets were contacted with two separate metal contacts on the inner BTS and the outer Sb_2Te_3 region. The contacts were defined by e-beam lithography, followed by thermal evaporation of Ti/Au . The amount of evaporated metals is dependent of the thicknesses of the both BTS and Sb_2Te_3 . In order to avoid contact between the BTS electrode and the Sb_2Te_3 , the bridging technique described in chapter 3 was used. The thickness of thermally evaporated SiO_x layer has been about 90 nm . One important observation was the linearity of the current(I)-voltage(V) characteristics measured across the p-n heterojunction, as depicted in Figure 6.5a at both high ($T = 290\text{ K}$) and low ($T = 1.4\text{ K}$) temperatures. The resistance decrease upon cooling reflects a metallic character,

which is due to the high doping degree of both heterostructure components, with the Fermi energy positioned within in the bulk conduction (valence) band for BTS (Sb_2Te_3). Similar metallic behavior has been documented for nanostructures made of the single components. Remarkably, the fully linear I/V behavior of the devices was preserved even for a large bias window of ± 1 V at $T = 1.4$ K showing no conventional diode behavior. If we assume that the

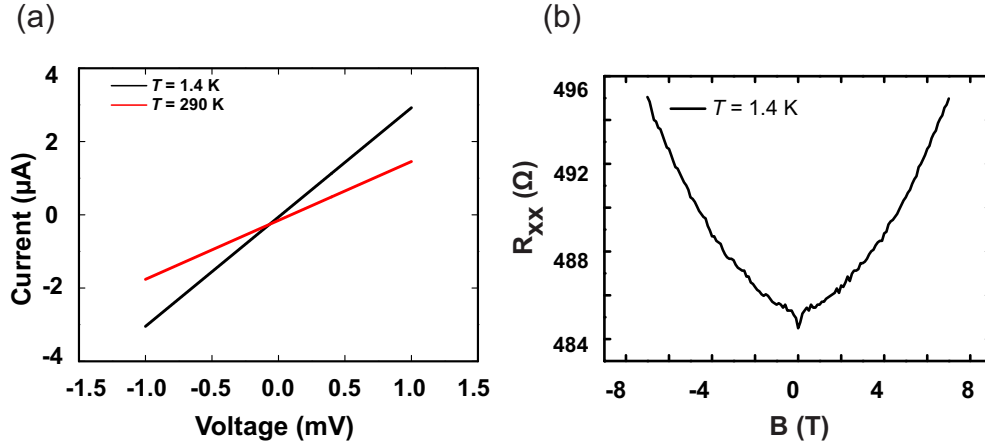


Figure 6.5 – (a) Current–voltage characteristics of a $\text{Bi}_2\text{Te}_2\text{Se}/\text{Sb}_2\text{Te}_3$ nanoplatelet at 1.4 and 290 K. The current was measured across the interface between the two components, using separate electrical contacts on the central $\text{Bi}_2\text{Te}_2\text{Se}$ region and the Sb_2Te_3 frame at the periphery. The inset shows the resistance of the same heterostructure nanoplatelet as a function of the magnetic field recorded at $T = 1.4$ K. The B-field is oriented perpendicular to the sample plane.

heterojunction is composed of two degenerately doped semiconductors, the devices would be expected to behave like an Esaki diode, exhibiting a negative differential resistance (NDR) peak in the backward bias direction. However, the presence of the topological surface states is likely to cause deviation from the NDR characteristics in the tunneling regime, which could explain the smooth, linear I-V curves observed for the present samples. In order to investigate further the properties of the junction, the vertical heterostructures of BTS and Sb_2Te_3 are fabricated using a stacking technique. Interestingly the same linearity was observed in most cases. This linearity points toward the different behaviour of topological insulator junctions in comparison to the semiconductor case. It is noteworthy that a small number of devices showed a weak rectifying behavior along with tiny wiggles, however, in all cases the origin of these features can be attributed to asymmetric Schottky barrier contacts on the two materials. Moreover, the two-probe magnetoresistance across the p-n junction (Figure 6.5b) displays a close-to-quadratic dependence for higher B-fields, along with a dip around zero B-field. The latter is due to the weak-antilocalization (WAL) effect, occurring due to the spin-orbit coupling in 3D TIs, and manifests itself also in the present heterostructure devices.[78]

6.3 Photothermoelectric Measurements

6.3.1 SPCM on Single Components

In order to get insight into the photocurrent mechanism of the lateral heterostructures, the photocurrent generation is first studied for single component BTS and Sb_2Te_3 . Figure 6.6 shows a photocurrent measurement on a 10 nm Sb_2Te_3 nanosheet. In every scanning measurement a reflection image is also recorded guiding the map of the photocurrent generated on different areas of the device. Figure 6.6a and b shows the reflection image and the photocurrent map, respectively. As it is clear from Figure 6.6c that the PC profile across the metal– Sb_2Te_3 junction

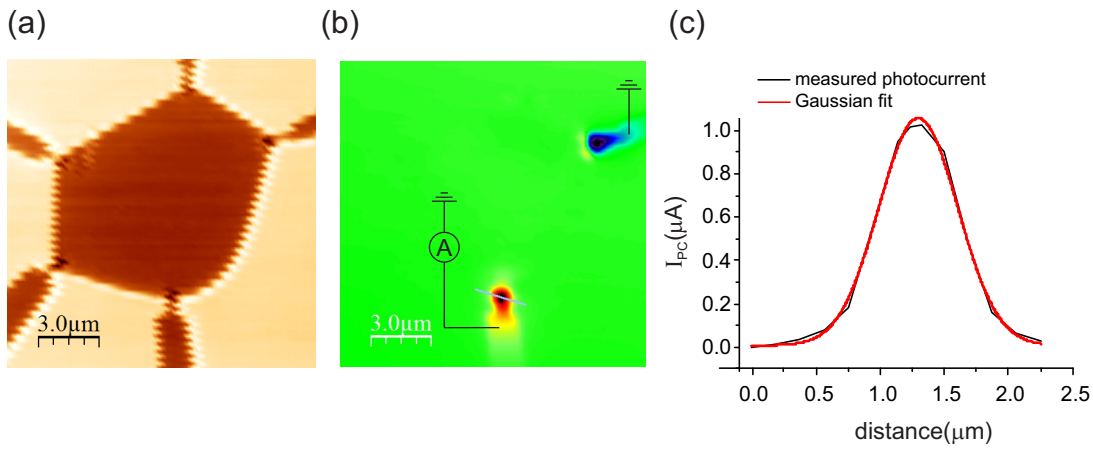


Figure 6.6 – (a) Reflection image of the Sb_2Te_3 device (b) photocurrent map of the device using two electrodes (c) the photocurrent profile across the line indicated in the PC map.

shows a Gaussian profile (the red line is the Gaussian fit). In the interpretation of the sign of photocurrent one important issue is the assignment of the drain and ground electrodes. Generally, in photocurrent measurements the electrode connected to a measurement unit is called source and the electrode used as a ground or connected to a source unit is considered as drain electrode. According to the convention flow of the electrons from the source electrode to the drain electrode, this gives a negative photocurrent. In Figure 6.6b the blue color indicates a negative and red color the positive sign of current.

Figure 6.7 is the same PC measurement on a BTS nanosheet with a the same thickness as the Sb_2Te_3 nanosheet . The comparison of Figure 6.6b and Figure 6.7b indicates that the sign of photocurrent in the same setup configuration is opposite for the two materials, in accordance with the opposite carrier sign of the two. If a photovoltaic mechanism for the photocurrent generation is to be considered, the opposite sign of the currents are expected at the metal–electrode junctions. Furthermore, the Gaussian distribution of the photocurrent hints towards the thermal photocurrent generation mechanism.

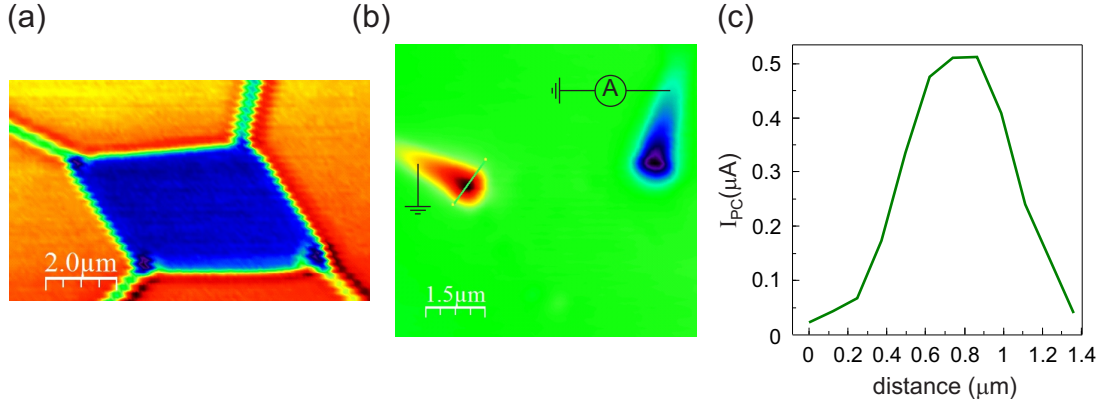


Figure 6.7 – (a) Reflection image of the BTS device (b) photocurrent map of the device using two electrodes (c) the photocurrent profile across the line indicated in the PC map.

6.3.2 SPCM on TI Lateral Heterojunctions

After studying the chemical composition and basic electrical behavior of the p-n heterojunctions, as well as investigating the PC generation mechanism at the TI–metal junction, the SPCM measurements are done on the heterojunctions. In order to gain spatially resolved infor-

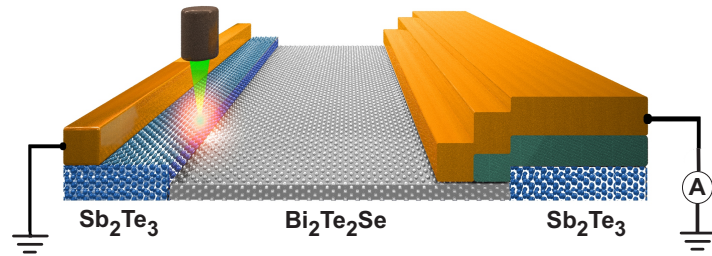


Figure 6.8 – Schematic depiction of a scanning photocurrent microscopy (SPCM) measurement, where a confocal laser spot is scanned across a $\text{Bi}_2\text{Te}_2\text{Se}/\text{Sb}_2\text{Te}_3$ device.

mation about the photo-electric behavior of the devices, scanning photocurrent microscopy (SPCM) is used, whose principle is illustrated in Figure 6.8. The SPCM set-up is operated under ambient with a focused green laser (530 nm) and a spatial resolution (laser spot size) of about ~ 400 nm. The photocurrent generated during a scan is collected through the two electrodes as a function of the laser spot position. The green color beneath the metal electrode shows the evaporated SiO_x on top of the Sb_2Te_3 region. Upon illumination of the p-n region within a lateral heterostructure (Figure 6.9) with the green laser ($\lambda = 514$ nm, laser power of $35 \mu\text{W}$), the original I-V curve (black line) is slightly down-shifted along the y-axis. This indicates

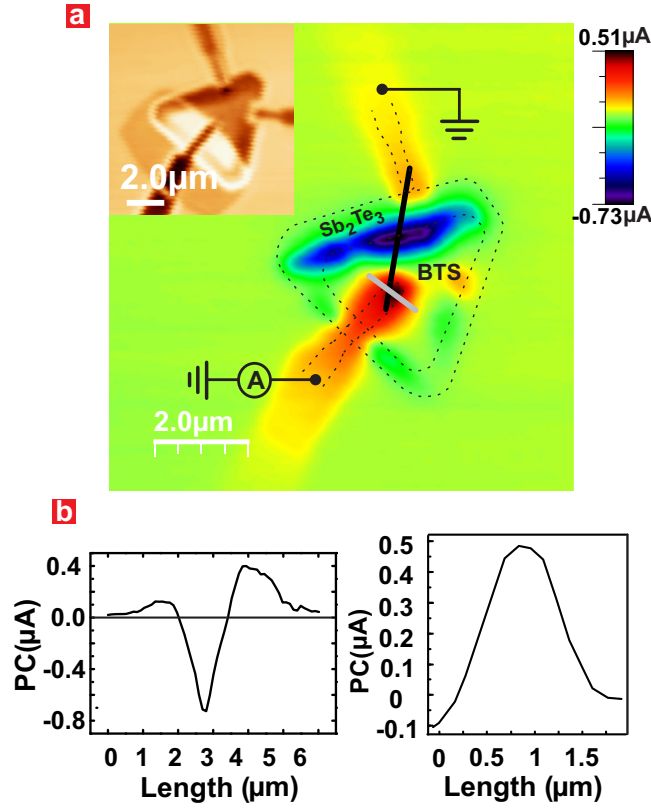


Figure 6.9 – (a) SPCM map of a $\text{Bi}_2\text{Te}_2\text{Se}/\text{Sb}_2\text{Te}_3$ nanoplatelet device with separate contacts on the two different components. The inset shows an optical image of the device. The dashed lines are drawn based on the overlap of the reflection and photocurrent image. The map was recorded under ambient conditions using $\lambda = 514\text{nm}$. (b,c) the PC line profile across the black line and the gray line, respectively.

a very small open circuit voltage V_{oc} on the order of 10 μV . Since the open circuit voltage is the potential difference of the two materials, this small V_{oc} is consistent with the lack of conventional diode like behavior.

Another observation is that upon illumination a substantial resistance increase of $\sim 230\ \Omega$ is caused which makes these devices suitable candidates for photodetectors. This prominent resistance increase under the laser illumination and applied bias indicates the coexistence of the thermoelectric and bolometric effect. The photocurrent dependence on light power, Figure 6.10b, shows a close-to-linear increase. In Figure 6.9a, the zero bias photocurrent map of a representative p-n heterojunction device is shown. It displays pronounced photocurrents at the source and drain contacts, as well as at the p-n junction. The photocurrents generated at the two contacts have identical sign, which is opposite to that of the photocurrent at the junction. In general, two major mechanisms can be responsible for photocurrent generation in such devices. The first one is the photovoltaic effect which involves the separation of photo-excited electron-hole pairs by a built-in electric field, while the second one is the photo-

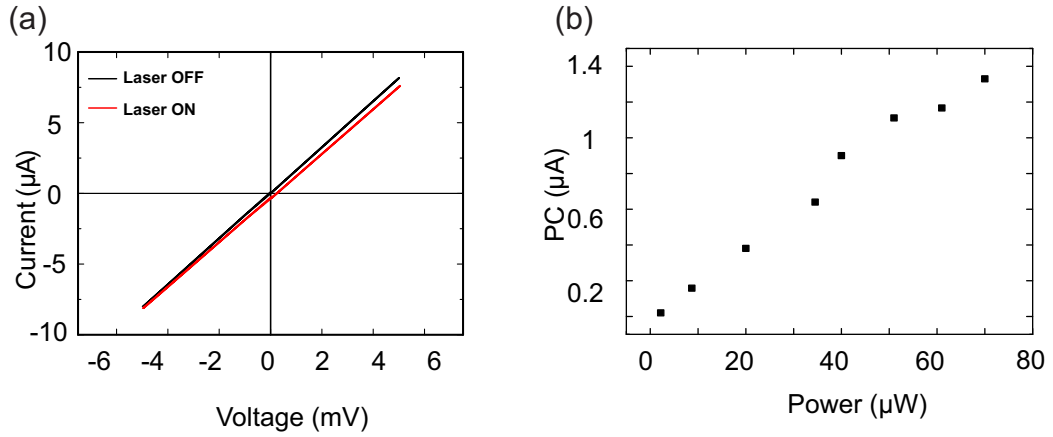


Figure 6.10 – (a) Current-voltage curves of $\text{Bi}_2\text{Te}_2\text{Se}/\text{Sb}_2\text{Te}_3$ nanoplatelets, acquired in the dark (black curve) and under laser illumination ($\lambda = 514\text{nm}$) of the interfacial region (red curve). The curves were measured using Sb_2Te_3 as the drain contact. All measurements were performed under ambient conditions. The inset is a plot of photocurrent vs laser power ($\lambda = 514\text{nm}$) for local illumination of the p–n junction.

thermoelectric effect arising from the temperature gradient across an interface between two materials with different Seebeck coefficients. To clarify the mechanism responsible for the PC generation in TI lateral heterostructure device, following points should be considered.

First, as apparent from the overlap between the photocurrent map and the reflection image in Figure 6.9a, the generated PC close to the contact regions extend several μm away from them. This behavior is in contrast to the more localized response typically detected in case of the photovoltaic effect. Second, the full linearity of the I–V curves over a wide bias range does not support the presence of sizeable Schottky barriers at the contacts as well as a built-in potential at the junction. Third, a stronger photocurrent signal at the contact to the BTS was reproducibly observed. This can be understood in accordance with the Seebeck coefficient difference between gold and BTS being larger compared to that between gold and Sb_2Te_3 . Furthermore, based upon the electron affinity of Sb_2Te_3 of between 4.1 and 4.5 eV and gold's work function of ~ 5 eV, the photovoltaic mechanism would be expected to result in an opposite sign of the photocurrent at the electrode than observed by experiment. Considering all the mentioned points, it follows that due to the laser-induced local heating, generated hot carriers are diffusing from the p-type Sb_2Te_3 to the n-type BTS, leading to a negative photocurrent in the junction of the depicted experimental setup.[78]

The photothermal current generated upon illumination at the junction is proportional to the difference between the Seebeck coefficients of the components, according to the following equation:

$$S_1 - S_2 = \frac{\Delta V}{\Delta T} \quad (6.4)$$

where S_1 (S_2) is the Seebeck coefficient of the p (n)-type material, ΔV is the generated voltage ($\Delta V = \Delta I R$ with ΔI as the induced photothermal current and R as the sample resistance), and ΔT is the temperature difference induced through local heating by the laser spot.

To estimate the temperature difference between the laser spot and the electrodes, the differential resistance change upon local heating is derived. For this purpose the BTS nanoribbons of 1.5 to 2.5 micrometers in length are grown. Laser illumination of the middle of the nanoribbon causes a resistance increase. The resistance of the same nanoribbon is measured in a cryogenic system for the temperature range of 1.4 to 300 K, Figure 6.11. Assuming a sufficiently small temperature raise, $\Delta R \approx \frac{dR}{dT} \delta T_{av}$ can be estimated. To obtain $\frac{dR}{dT}$, the temperature dependent resistance was fitted by [79]

$$R = R_0 + \alpha e^{-\frac{\theta}{T}} + \beta T^2 \quad (6.5)$$

and the derivative of this equation

$$\frac{dR}{dT} = -\alpha \theta \frac{e^{-\frac{\theta}{T}}}{T^2} + 2\beta T \quad (6.6)$$

for a temperature range 50 to 300 K. Measurements of the dark resistance of the BTS nanoribbons as a function of temperature (between 1.4 and 298 K) yielded a temperature coefficient of $dR/dT = 3.2 \Omega/K$. This approach was followed for three different nanoribbons using the same laser power, resulting in similar changes in temperature.

Assuming that the laser-induced resistance change ΔR under this condition originates from local heating, the temperature difference ΔT between the illuminated spot and the electrodes is estimated to be 0.3 ± 0.05 K for a laser power of $5.2 \mu W$ (0.4 ± 0.02 K for a power of $8.7 \mu W$) averaged over different samples. It should be emphasized that the above estimation is limited to a maximum laser power of $20 \mu W$. For higher power, the appreciable concentration of photo-excited carriers enhances the optical absorption and thereby favors further heating, which would lead to an overestimation of temperature. For the lateral heterostructure device, inserting the measured resistance R , the magnitude of the photocurrent ΔI detected at the p-n junction, and the estimated temperature ΔT difference into equation 6.4 yields a Seebeck coefficient difference of $\sim 200 \mu V/K$. This value exceeds those reported for single component bismuth chalcogenide nanostructures such as Bi_2Te_3 and Sb_2Te_3 nanowires ($\sim 150 \mu V/K$) [70, 80].

To assess the accuracy of this estimation, the Seebeck coefficient was numerically derived by a semi-classical transport approach using the BoltzTrap code. These calculations were performed by Dinh Loc Duong at Sungkyunkwan University, South Korea. The band structure and density of states (DOS) of BTS and Sb_2Te_3 were calculated using the Quantum Espresso package. The bulk structure was fully optimized until an energy and force convergence below 0.003 eV and 0.05 eV/Å were reached, respectively. The band structure of the optimized structures was calculated by including spin-orbit interaction. Moreover, $24 \times 24 \times 3$ uniform grids were used, and the exchange-correlation was estimated by the general gradient approximation (GGA) in terms of the PBE functional. The ultrasoft potential with a cut-off energy of 60 Ry was

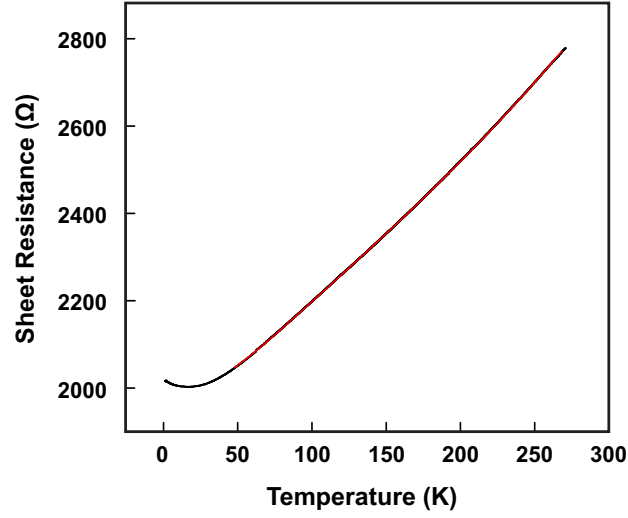


Figure 6.11 – Sheet resistance of a BTS nanoribbon measured over a temperature range of 1.4 to 300 K. The red line is the fitting curve as described in the text.

used for Sb_2Te_3 while the projector augmented wave potential with a cutoff energy of 80 Ry was implemented in case of BTS. The DOS was calculated using a denser grid with $48 \times 48 \times 6$ k-points. Thus obtained DOS was then imported into the BoltzTrap code to calculate the Seebeck coefficient.[78]

As apparent from Figure 6.12, the simulated Seebeck coefficient for both compounds shows, as expected, a strong dependence of the Fermi energy. From separate Hall measurements on individual BTS and Sb_2Te_3 nanoplatelets, an electron concentration of $n = 1.2 \times 10^{19} \text{ cm}^{-3}$ for BTS, and a hole concentration of $p = 7.4 \times 10^{20} \text{ cm}^{-3}$ for Sb_2Te_3 is derived, confirming the strong (degenerate) doping degree of both compounds. Based upon the effective mass of $0.11 m_e$ [81] for electrons in BTS and $0.78 m_e$ [82] for holes in Sb_2Te_3 , and assuming for both compounds an approximately quadratic band structure close to the Fermi level, we estimate from the equation

$$E_F = \frac{\hbar^2}{2m} (3\pi^2 n)^{(3/2)} \quad (6.7)$$

the Fermi level of BTS to be 0.17 eV above the conduction band edge, and the Fermi level of Sb_2Te_3 to be 0.23 eV below the valence band edge. Combined with the calculated data in Figure 6.12, this yields a Seebeck coefficient of about $-120 \mu\text{V/K}$ for BTS and $+65 \mu\text{V/K}$ for Sb_2Te_3 . The corresponding difference $S_2 - S_1 = 185 \mu\text{V/K}$ is in good agreement with the experimental observation.

Overall, the above measurements demonstrate that the well-defined composition and elec-

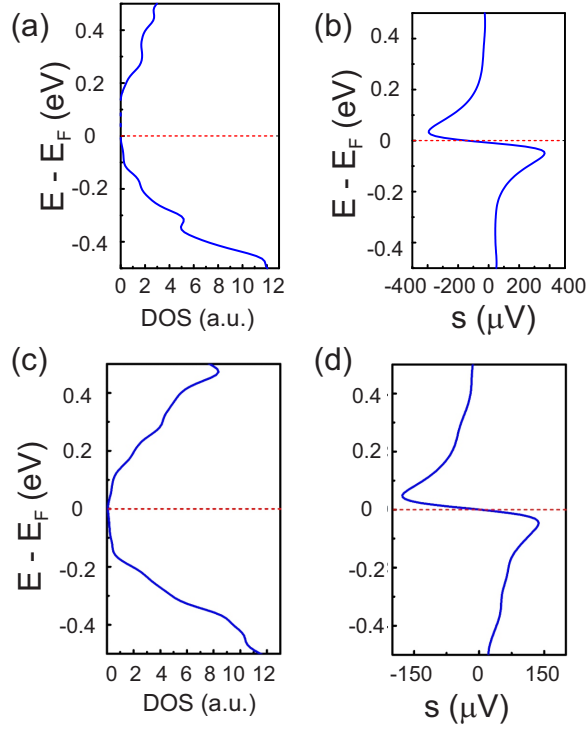


Figure 6.12 – (a) and (c) Density of states (b) and (d) Seebeck coefficient for Sb_2Te_3 and BTS.

tronic structure of the BTS/Sb_2Te_3 nanoplatelets endows them with a high thermoelectric performance. It may be possible to further improve the device performance by tuning the Fermi levels through local molecular surface doping. The heterostructures are amenable to implementation into a more elaborate device configuration that allows directly harnessing environmental temperature gradients. Moreover, it would be interesting to evaluate their performance as photodetectors. Another degree of freedom to control the PC generation is to change (reduce) the thickness of the both materials in order to hybridize bottom and top surface states to open a band gap.

7 Electronic and Magnetic studies of α -RuCl₃¹

7.1 Background on α -RuCl₃

The exactly solvable Kitaev model on the honeycomb lattice represents a class of 2D quantum spin liquids which supports fractionalized excitations.[83] It consists of a set of spin-1/2 moments \mathbf{S}_i arranged on a honeycomb lattice. However, in real materials a Heisenberg interaction is also generally expected to exist, giving rise to the Kitaev-Heisenberg (KH) Hamiltonian[1]

$$H = \sum_{ij} (K S_i^m S_j^m + J \mathbf{S}_i \cdot \mathbf{S}_j) \quad (7.1)$$

in which m is the projection of the spin along the bond connecting the spins ij . Importantly, the Hamiltonian 7.1 has proposed to precisely describe the edge shared octahedrally coordinated magnetic systems with dominant SOC.[83] Among a variety of QSL candidate compounds, the honeycomb semiconductor ruthenium(III) chloride (RuCl₃) has proven especially promising to fulfill the requirements by the Kitaev-Heisenberg (KH) model.[84, 85, 86] Two types of Majorana fermions have been predicted in Kitaev model and shown by quantum Monte-Carlo simulations based on the KH model.[87] The majorana fermions around the point of equal coupling strength ($K_x = K_y = K_z$) are itinerant and form a gapless majorana metal. However, if these coupling do not share the same strength a gapped spin liquid state will emerge. [1, 87]

Especially signatures of the gapless majorana fermions are expected to be experimentally observable due to the onset of spin-spin correlations and the emergence of fractionalized excitations in the QSL host material.[88, 89]

What makes α -RuCl₃ an interesting system to study in this field is the unusual features above the magnetic ordering temperature which has been interpreted to the proximity to the Kitaev

¹Parts of this chapter are based on our manuscript "Electrical Transport Signature of the Magnetic Fluctuation-Structure Relation in α -RuCl₃ Nanoflakes", publication 1 in Curriculum Vitae (page 97).

spin liquid.

7.1.1 Experimental Evidence

Possible fingerprints of Kitaev interactions in α -RuCl₃ have been observed in different types of experiments. Inelastic light scattering experiments revealed the existence of fermionic excitations in a broad energy and temperature range which also emphasized the importance of magnetic materials as hosts of Majorana fermions.[89] Raman measurements reveal a broad continuum as well as a significant line shape broadening of the low energy peaks below 100 K.[88] Since all the known magnets in more than 1D possess magnons as their elementary excitations, a bosonic excitation behavior is expected. As a result the deviation from bosonic distribution hints towards mixed fermionic bosonic excitations. [89]

Another important experimental feature has been observed in the magnetic scattering observed in inelastic neutron scattering. At low energies the scattering is consistent with the spin waves on a zig-zag ordered background, however, at higher temperatures a broad scattering continuum was observed. The analytical calculations based on Kitaev-Heisenberg Hamiltonian has produced similar features.[34, 90]

7.1.2 Structure and Magnetism

X-ray diffraction data has indicated that the crystal structure at low temperatures is described by C2/m space group with some degree of stacking faults (see Figure 7.1).[6] The STEM and

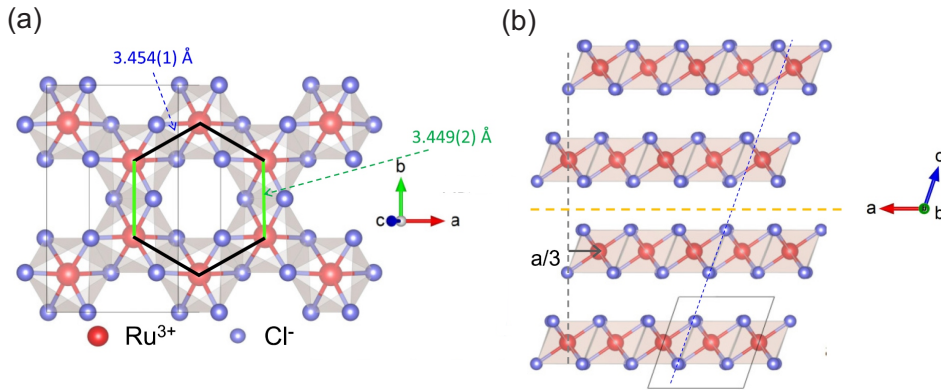


Figure 7.1 – (a) Schematic depiction of the in-plane α -RuCl₃ crystal structure in C2/m space group symmetry, (b) ABAB stacking along the c direction, perpendicular to the honeycomb in-plane structure. The blue dashed lines indicate slight shift of the layers occurring after the orange dashed line. Figure adapted from [6]

neutron scattering experiments confirmed a structural transition about 150 K which also explains the kinks observed in the susceptibility measurements.[91] This high temperature feature has been observed in different experiments. A nuclear magnetic resonance (NMR) study on the spin-lattice relaxation rate T_1^{-1} of the ³⁵Cl isotope revealed a transition temperature of 160 K.[92] Furthermore, based on the deconvolution of the phononic and magnetic

contributions to the thermal conductivity, a transition temperature of 140 K was found.[93]

The α -RuCl₃ single crystals required for mechanical exfoliation were grown from commercially available powder (Roth, 99.9+ % purity) following a modified literature procedure². [94] Specifically, an evacuated quartz ampoule containing the powder was heated to 700 °C at the hot end. At the cooler end (600 °C) of the tube the crystal platelets with a size of up to 4-8 mm² were formed. The elemental composition of the crystals was verified by an energy dispersive X-ray spectrometer (Si/Li detector by Oxford Instruments) on a scanning electron microscope Vega TS 5130 MM (Tescan). The samples displayed an elemental ratio of Ru : Cl = 1 : 3. The crystal structure was confirmed by single crystal X-ray diffraction on a three circle diffractometer (Bruker AXS) equipped with SMART APEX I CCD using Mo-K α radiation. The crystals were indexed in the $C2/m$ space group with the lattice parameters $a = 5.9917(13)$ Å, $b = 10.367(2)$ Å, and $c = 6.0543(13)$ Å with the presence of approximately 4 % stacking faults, similar to crystals reported previously.[6]

The magnetic properties, evaluated by SQUID magnetometry, are consistent with previous reports on α -RuCl₃ with some degree of stacking faults.[6, 95] Three characteristic magnetic features were observed upon cooling, specifically a high temperature transition at 170 K, followed by two low temperature transitions at 7 K and 14 K, respectively. The high temperature transition at 170 K has been ascribed to a change in the stacking order as well as transition to a Kitaev-paramagnetic state,[91, 15] while the low temperature transitions at 7 and 14 K most likely arise from the stacking disorder and the emergence of the complex magnetic structure, respectively.[6]

To study the α -RuCl₃ in reduced dimension, they were mechanically exfoliated from large α -RuCl₃ crystals onto Si substrates covered by 300 nm SiO₂. The thickness of the resulting flakes ranged from a few up to 50 nm, as determined by atomic force microscopy (AFM). In order to explore the existence of the fermionic excitations in the thin sheets of α -RuCl₃, they were first investigated by temperature dependent Raman spectroscopy.

7.2 Inelastic Light Scattering of α -RuCl₃ Nanosheets

7.2.1 Laser heating and substrate background

The Raman spectroscopy measurements were done using a green laser (532 nm) with a spot size of ~400 nm and a laser power of 330 μ W. Before investigating the temperature dependent Raman spectroscopy of α -RuCl₃, two important issues should be addressed. The first one is the choice of appropriate laser power in order to avoid the extra heating effect by the laser. Secondly, since the thin sheets of the material on a substrate is measured, the substrate background contribution should be taken in account.

To find the right laser power, the Raman spectra of a thin flake of α -RuCl₃ with different laser powers are taken, (see Figure 7.2a). Upon increasing the power stepwise from 40 μ W up to 4500 μ W, at about 700 μ W the Raman peaks start to shift toward lower energy. This mode softening

²The growth of the material as well as crystal analysis was done by Daniel Weber, Lotsch Department, Max Planck Institute with the help of the institute service group.

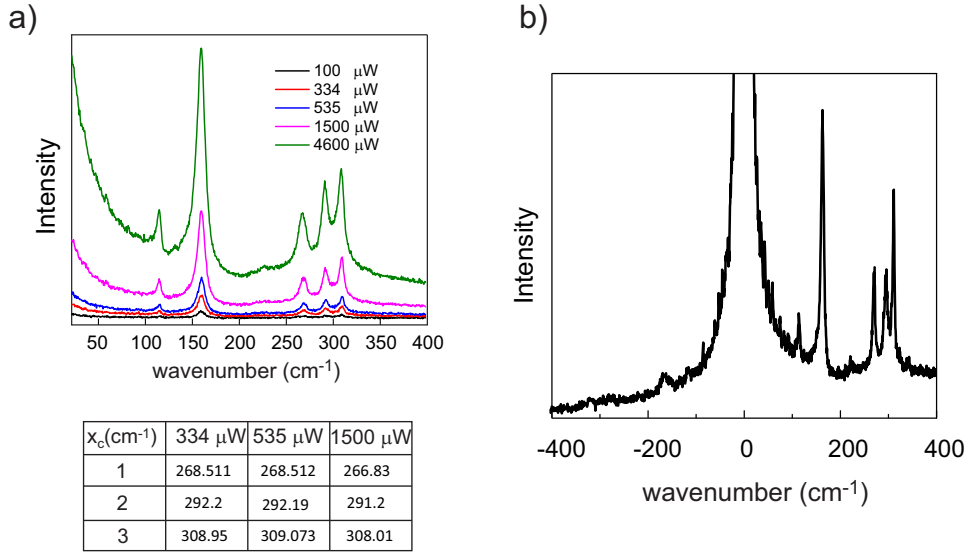


Figure 7.2 – (a) Raman spectra of a thin sheet (10 nm) of RuCl₃ measured using different laser powers, the table show the peak positions of the three Lorentzian peaks. b) Raman spectrum of the same nanosheet measured using 530 μW laser power at 70 K.

hints toward heating of the sample by the laser light, (see the Table in Figure 7.2). Furthermore, another method to detect heating of the sample is the appearance of the anti-Stoke peaks, since the anti-Stoke radiation gains energy from the lattice. To study the presence of the anti-Stoke modes a Notch filter was used. The nanoflake spectra acquired at 70 K using 530 μW laser power, as shown in figure 7.2b, display no distinguishable anti-Stoke peaks, indicating negligible heating. Generally, upto 530 μW no observable shift of the modes or presence of clear anti-Stoke peaks was noticed. Nonetheless, still lower power of 330 μW is used to safely exclude any laser heating effect which otherwise may affect the data.

Regarding the substrate subtraction, at each temperature spectra from both, the nanoflake and the bare substrate is recorded, using the same laser parameters and accumulation times. Normally with 330 μW laser power, 60 seconds exposure was required to get a high signal to noise ratio which is three times accumulated. For peak analysis, first the general background from both spectra should be subtracted. Then the substrate peak at 520 cm^{-1} can be used to find the contribution of the substrate to the spectrum. Finding the ratio of substrate Raman peak in the α -RuCl₃, this ratio is then multiplied by the substrate spectrum and finally this spectrum will be subtracted from the α -RuCl₃ Raman spectrum. Figure 7.3a shows the Raman spectra of an exemplary α -RuCl₃ nanoflake taken with both xx and xy polarizations. Both spectra show narrow phonon modes as well as a broad continuum at low energies. Measurements on the bare SiO₂/Si substrate shows that, the substrate background in the low energy region (where the broad continuum due to fermionic excitations is most pronounced is weaker for xx- than for xy-polarization. Due to this lower substrate contribution

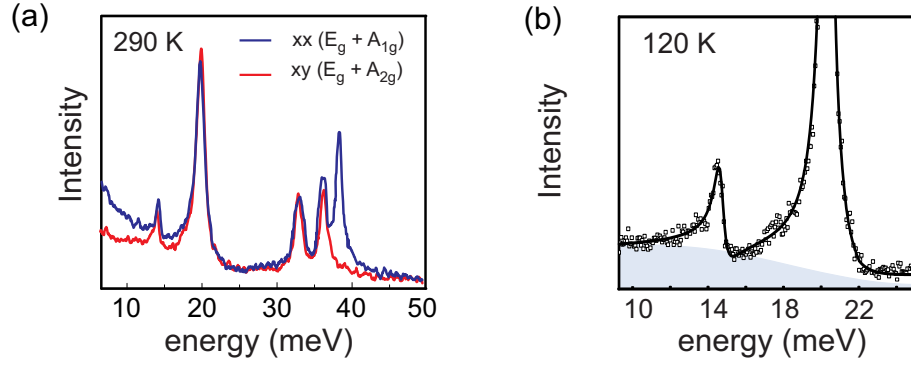


Figure 7.3 – (a,b) Schematic depiction of the crystal structure of α -RuCl₃ along the [010] and [001] direction respectively, (c) polarized Raman response of α -RuCl₃ thin sheet, (d) detail of the low energy regime of the Raman spectrum, with the blue shading added to highlight the low energy background continuum.

with xx polarization, all the temperature dependent measurements are performed using this polarization.

Figure 7.3b highlights the spectrum of the nanoflake at 120K only in the low energy regime after background subtraction. The blue area indicates the broad continuum extending upto about 20 meV.

7.2.2 Temperature Evolution of the Raman Spectrum

To see the effect of the exfoliation on the structure of the α -RuCl₃, its Raman spectra is compared with the one for bulk. Raman spectra recorded from the bulk and a 10 nm thick

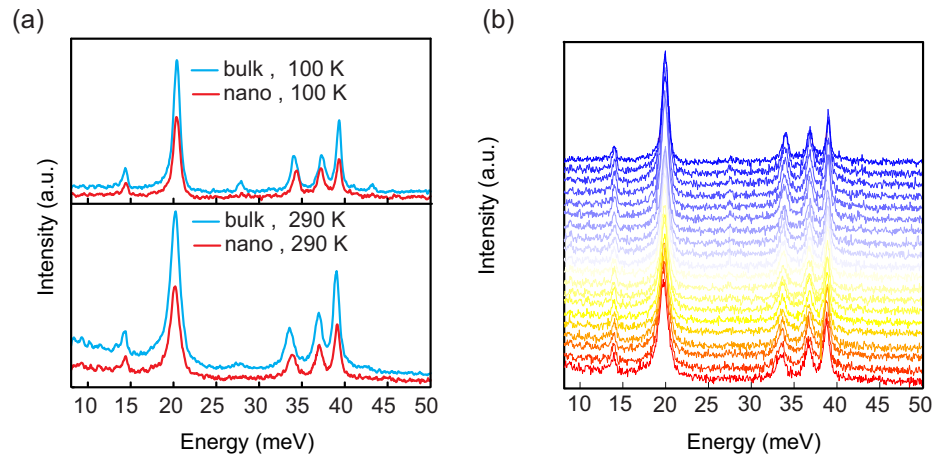


Figure 7.4 – (a) Comparison of the Raman spectra of α -RuCl₃ bulk and a 10 nm thick nanoflake at high (bottom) and low (top) temperatures, (b) Temperature dependent Raman spectra of the nanoflake from 283 to 123 K.

α -RuCl₃ nanoflake are compared as depicted in Figure 7.4a. Since the Raman intensity of the nanoflake using low laser power is in general much weaker than bulk, the minor peaks at 28 and 43 meV, although present, are difficult to distinguish from the noise level. Beside that no major change of the peak positions or shapes due to the exfoliation can be discerned at $T \sim 290$ K (top panel) and $T \sim 100$ K (bottom panel). The close agreement between the bulk and nanoflake spectra in these experiments testifies that the in-plane crystal structure is largely preserved during the mechanical exfoliation.

As it was mentioned the Raman spectra of the bulk α -RuCl₃ show a broad continuum in the low energy range (blue background in the spectrum of Figure 7.3b).

The broad continuum, which in the bulk case has been attributed to the fractionalized excitations originating from Kitaev interactions, is also observable in the nanoflake spectra. Since the two low energy lattice vibrations at 14 and 20 meV lie on the magnetic continuum, they have an asymmetric peak shape of the Fano type. The evolution of the Raman peaks upon cooling is displayed in Figure 7.4b.

For further analysis, the Raman peaks were fitted in accordance with literature procedures.[89, 15] To this end, the peaks at 14 and 20 meV, which are superimposed on a broad continuum, are fitted with a Fano-like peak shape, while the peaks at 33, 36 and 38 meV are fitted with symmetric Lorentz functions.

As apparent from Figure 7.5a the peaks at 14 and 20 meV, respectively, can be well fitted with Fano like function of the form $F(\omega) = F_0 \frac{(\varepsilon+q)^2}{1+\varepsilon^2}$ in which q is the asymmetry parameter and $\varepsilon = \frac{\omega-\omega_0}{\Gamma}$. The Fano shape of the peaks indicates the coupling between the continuum of excitations and the sharp lattice vibrations. The mode frequency, the linewidth and the Fano asymmetry parameter derived from the fitting of the 20 meV phonon mode are plotted as a function of temperature in Figure 7.5b,c and d, respectively. The errors are within the symbol size. Normally in equilibrium conditions a crystal is described within the theory of harmonic lattice. However, when crystal is subjected to temperature changes, a static lattice of ions will not apply anymore and the anharmonic model should be taken in account. While cooling results in a general decrease of the peak width, the slope of this change is seen to decrease below 200 K, deviating from the anharmonic model. The temperature dependence of the phonon frequency and self-energies are generally determined by the lattice anharmonicity which is a monotonic function of the form:

$$\Gamma(T) = \Gamma_0 + A[1 + 2n(\omega_0/2)] \quad (7.2)$$

in which $n(E) = 1 / (e^{E/K_B T} - 1)$ is the thermal bosonic factor, and Γ_0 and ω_0 are the FWHM and frequency, respectively, at zero Kelvin. First the frequency temperature evolution is fitted, with the frequency value at $T = 0$ K obtained by extrapolation. Using this value it is possible to fit the FWHM with the anharmonicity model for the temperature range $200\text{ K} < T < 300\text{ K}$ and gained the values for Γ_0 and ω_0 . The anharmonicity function is monotonic down to very low temperatures as confirmed by the calculations as well. The deviation from this monotonic behavior can be clearly observed.

Such deviation from the anharmonic model has also been observed in bulk α -RuCl₃ near $T =$

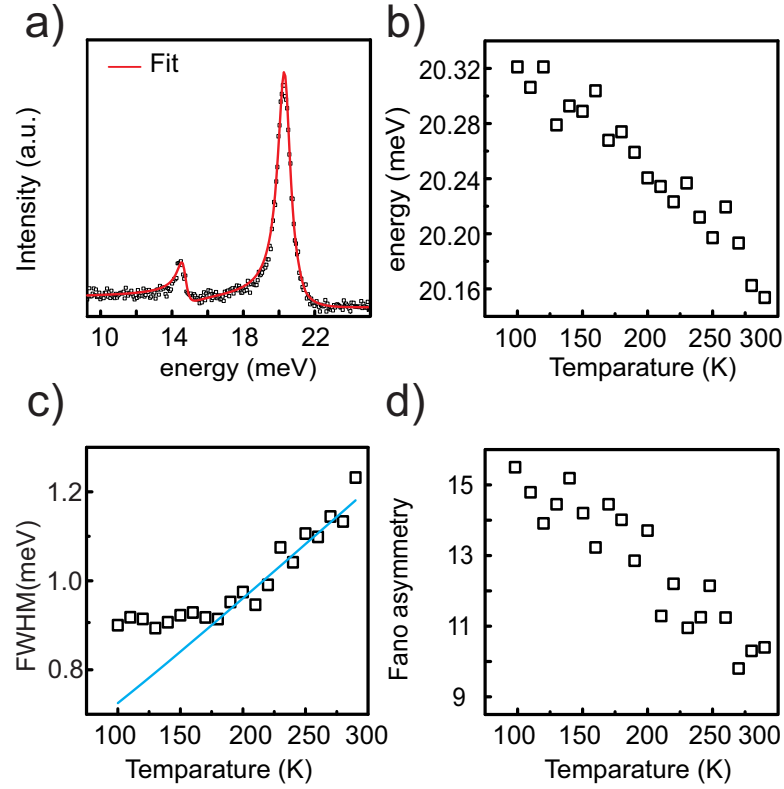


Figure 7.5 – (a) Raman spectrum and corresponding Fano function fit of the low energy range, (b) , (c) and (d) temperature evolution of the energy, linewidth and the Fano asymmetry parameter of the 20 meV peak, respectively.

140 K and attributed to the emergence of the fractionalized excitations with mixed bosonic and fermionic character, leading to spin-phonon scattering.[15, 88] Also similar observations were reported for harmonic-honeycomb iridates β - and γ -Li₂IrO₃. [9] The 14 meV phonon mode shows essentially the same behavior upon cooling like the 20 meV phonon. Figure 7.6 shows the time evolution of the remaining peaks.

It is furthermore noteworthy that upon cooling, the spectral weight of all these peaks first decreases and then increases again (Figure 7.7). A similar trend has been reported for α -RuCl₃ bulk samples as well as a recent work on few layer α -RuCl₃ as a fingerprint of the structural phase transition, influencing the bond directional Kitaev interactions. [89, 96]

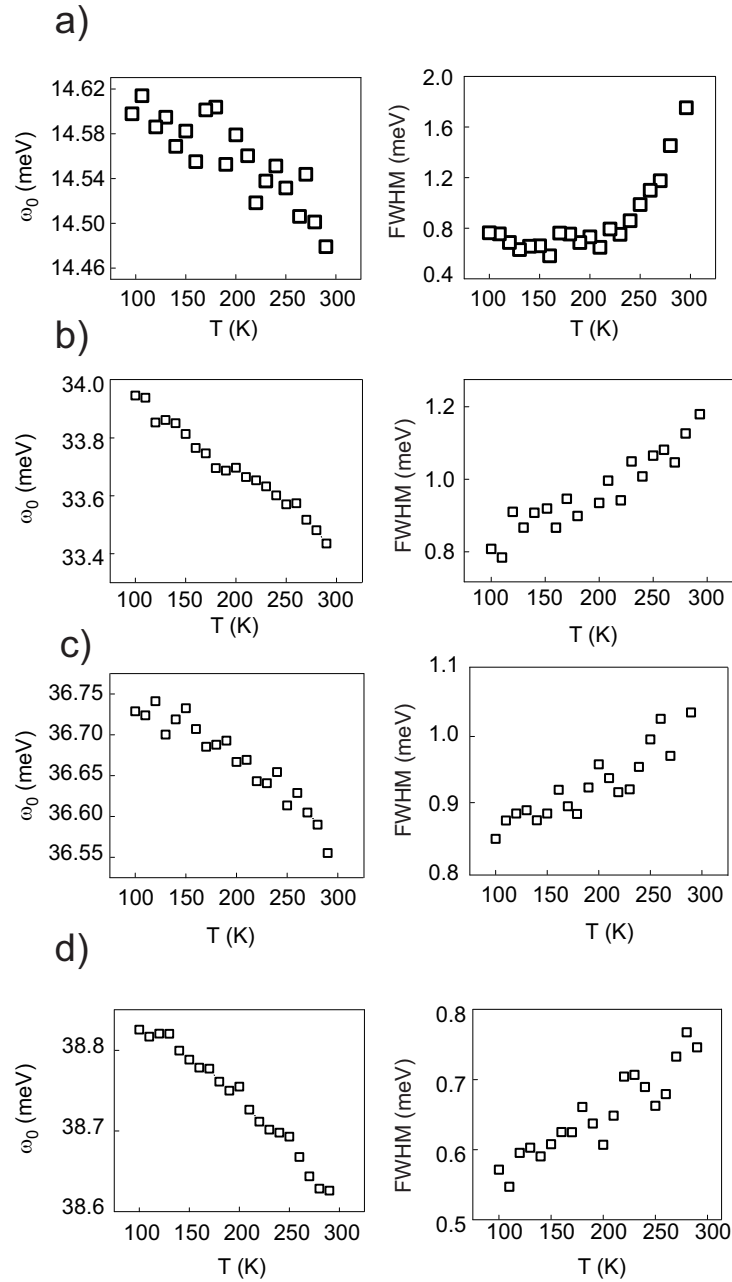


Figure 7.6 – Temperature dependent evolution of frequency and FWHM of the (a) 14 (b) 34 (c) 37 and (d) 38 meV Raman modes of α -RuCl₃ nanoflake of 10 nm thickness with substrate subtraction.

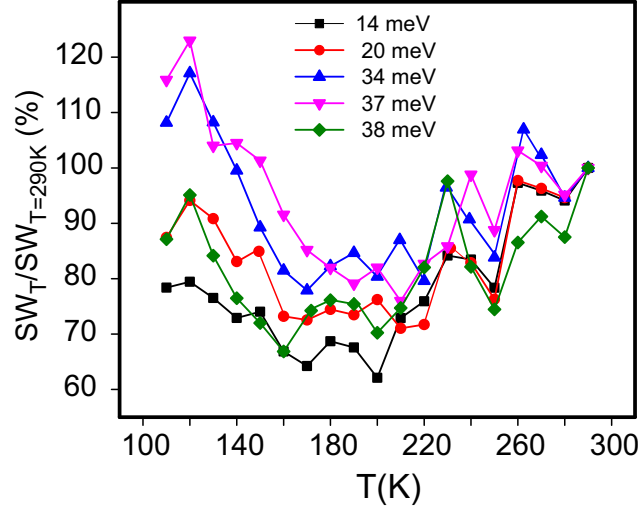


Figure 7.7 – Change of the integrated Raman intensity I_T relative to $I_{T=283K}$ of the Eg peaks at 14, 20, 33 and 36 meV as well as the A1g peak at 38 meV in the nanoflake.

7.3 Electrical Transport Measurements of α -RuCl₃ Nanosheets

7.3.1 Contact resistance

Despite the notable progress on this material, the onset of Kitaev interactions in α -RuCl₃ has not yet been addressed by charge transport experiments and only little is known about how these interactions are influenced when the sample dimensions are reduced. To study α -RuCl₃ nanosheets, it is essential to fabricate low resistance electrode contacts to the material. A reliable electrical contacting procedure which yields high quality metal contacts on individual α -RuCl₃ nanosheets with a thickness down to ~ 10 nm is reported in this chapter. Having demonstrated the onset characteristic of the Kitaev interactions in the nanoflakes by spectroscopic means, they are further investigated by electrical transport measurements. In early electrical experiments on bulk crystals of α -RuCl₃, a band gap of ~ 0.25 eV was determined.[97, 91] More recent bulk charge transport studies did not yield information about the potential onset of Kitaev interactions in α -RuCl₃, as the electrical resistance became immeasurably high already above the expected transition temperature.[98] A major issue in such experiments is the difficulty to achieve reliable electrical contacts to them.

In this thesis the temperature dependent electrical resistivity of α -RuCl₃ nanoflakes with a thickness down to ~ 10 nm is measured. Based upon the thickness of 0.57 nm for a single slabs of α -RuCl₃, [99, 6] it follows that a 10 nm thick nanoflake comprises approximately 18 slabs. As an essential prerequisite for the charge transport measurements, a contact resistance (R_c) below 10 k Ω through an Ar milling pretreatment of the contact regions is achieved.

Individual nanoflakes were electrically contacted by a standard e-beam lithography process, followed by an Ar milling step (300 mW, 10 s) to clean the contact region, and subsequent thermal evaporation of Ti/Au (2/40 nm) under a pressure of 10^{-8} mbar. It is noteworthy that

Ar milling has no destructive effect on the area of the material under measurement.

7.3.2 Temperature Dependent Resistance Measurements

Both DC and AC measurement methods can be used to measure the resistivity in a wide temperature range. However, since the sample undergoes a Mott transition and becomes insulating, a DC or semi DC measurements yields more accurate results. The DC electrical measurements were performed in a liquid helium cryostat (Oxford) by recording I-V curves using slow sweep rates ($\sim 1 \text{ K min}^{-1}$) within a small bias voltage (few mV) in order to maintain equilibrium conditions. In total more than 20 samples were measured with both DC and AC techniques.

An exemplary α -RuCl₃ nanoflake device is shown in Figure 7.8a, with a thickness of $\sim 14 \text{ nm}$, as concluded from the corresponding AFM section profile in Figure 7.8b.

The temperature dependent resistivity of the device is measured with different cooling rates. Figure 7.8c shows such a measurement along with the same curve measured with 1 and 3 K min^{-1} (inset). At room temperature, the resistivity is on the order of $10^{-1} \Omega \text{ cm}$. The resistance

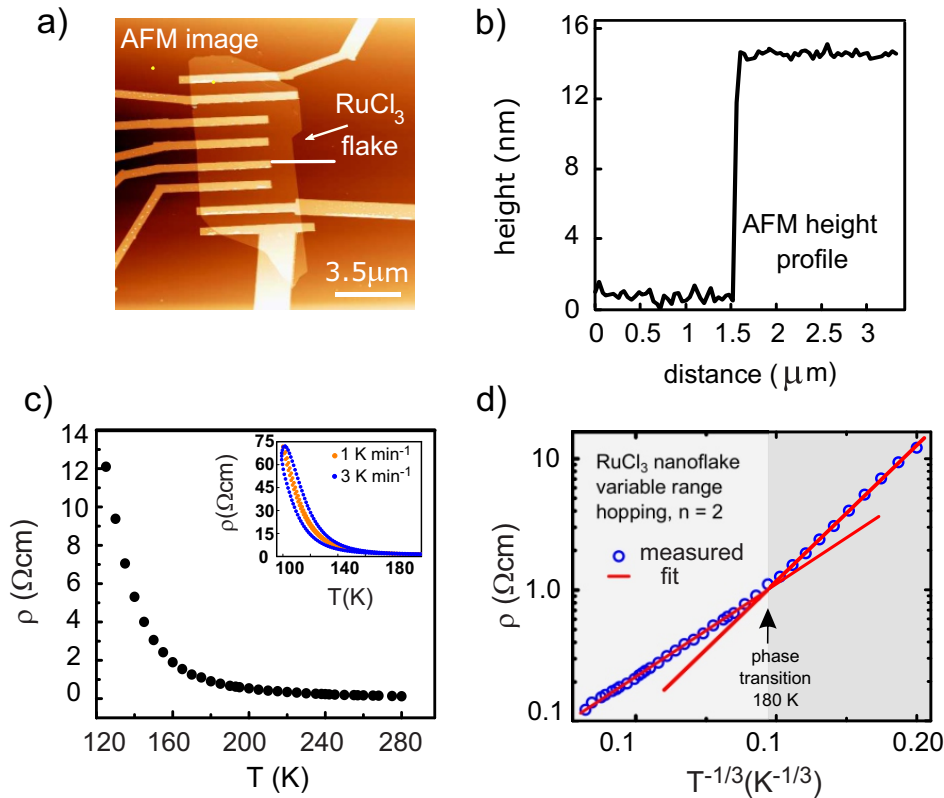


Figure 7.8 – (a) AFM image of a typical device (b) height profile of the α -RuCl₃ sheet in the device, (c) Resistivity ρ vs. T of a nanoflake with a thickness of 14 nm; the inset shows full temperature cycles for two different rates, (d) Semi-logarithmic plot of the resistivity ρ vs. $T^{-1/3}$ with linear fits (red lines) of a typical heating/cooling cycle, based on the VRH model.

of the nanoflake rapidly increases by cooling, as expected for a Mott insulator. For all of the devices an insulating behavior was observed below approximately 120 K and the resistance was not measurable. In all temperature regimes the resistance of the sample upon cooling always increases indicating an insulating behavior. The conduction in this material happens by hopping of electrons between neighboring impurities. At sufficiently low temperatures, hopping conduction occurs due to the states whose energies are in a narrow band near the Fermi level. [100] The thermally activated electrical conduction behavior can be accounted for in the framework of the two-dimensional variable range hopping (2D VRH) model, which predicts the following dependence:

$$\rho = \rho_0 \exp(T_0/T)^{1/n+1} \quad (7.3)$$

where n is the transport dimensionality, and T_0 is the characteristic temperature given by:

$$T_0 = \frac{21.2}{k_B N(E_F) \xi^3} \quad (7.4)$$

where k_B is the Boltzmann constant, $N(E_F)$ is the density of states at the Fermi level and ξ is the localization length. The linearity of the semi-logarithmic plot of ρ vs. $T^{-1/3}$ in Figure 7.8d indicates $n = 2$, confirming the 2D nature of the in-plane conduction.

However, in the plot of Figure 7.8d two different regions of slightly different slope can be distinguished, with a transition temperature of approximately 180 K. The same measurements were performed on a series of nanoflakes with thickness as small as 7 nm; all revealing the same change of slope occurring between 170 and 180 K.

This temperature range is remarkably close to the expected structural transition temperature of α -RuCl₃ which is intimately coupled to the onset of Kitaev interactions. The individual linear fits using equation 7.3 yielded $T_0 = 5.3 \cdot 10^5$ for the temperature range of $180 \text{ K} < T < 284 \text{ K}$, and $T_0 = 1.58 \cdot 10^6$ for the range of $125 \text{ K} \leq T \leq 180 \text{ K}$. Both these values are in reasonable agreement with those reported for other Mott insulators. [101, 102] Assuming a constant density of states at E_F , it would follow that the localization length increases by a factor of 1.4 at higher temperatures, which in turn decreases the sample resistance. Such variations in localization length is suggestive of enhanced electron-electron correlations as a consequence of the change in the lattice structure. As a result it establishes a link between the change in hopping behavior of the material and the onset of Kitaev interactions detected in the Raman experiments. According to theory such correlations can influence the electron hopping probability and hence cause a slope change in the temperature dependence of conductivity.[103] In bulk α -RuCl₃ this onset has been experimentally observed at lower temperature (between 100 and 160 K during the cooling cycle; see the literature data collected in Table 7.1). One explanation for this might be the presence of surface strain in the nanoflakes, in analogy to observations made on thin films.[104, 105].

Another relevant observation in our all devices is the small hysteresis in the temperature dependent resistivity of the α -RuCl₃ nanoflakes. This observation is in contrast to the pronounced hysteretic behaviour of α -RuCl₃ bulk samples as observed by various experimental

Table 7.1 – High temperature transitions in bulk α -RuCl₃, hysteresis and method of determination.

Onset	Hysteresis	Method of
T_t [K]	ΔT [K]	determination
100	not given	Raman scattering[88]
140	25	Neutron diffraction[91]
115	50	Neutron diffraction[106]
70	100	Raman scattering[15]
115	50	Reflectivity[107]
160	not given	³⁵ Cl NMR
100	not given	Heat capacity[14]
150	not given	THz spectroscopy[98]
100	not given	Thermal conductivity[93]

methods (see the literature data collected in Table 7.1). However, it should also be taken into account that the material does not go under a metal insulating transition.

In general, a structural transition occurring between a low-temperature insulating phase and a high-temperature hopping conduction phase exhibits a hysteresis whose width depends on the density of defects acting as nucleation sites for the transition. A higher defect density is correlated with a wider temperature range over which the two phases coexist. Accordingly, sample annealing that improves the crystal perfection has been shown to lead to a steeper transition and larger hysteresis, as a consequence of the reduced number of defects within the volume. [108, 109] In the transport measurements of α -RuCl₃ nanoflakes the small resistivity hysteresis in Figure 7.8c is characteristic of an enhanced defect density which increases the coexistence range of the two different phases. Similar observations have been made for the magnetic susceptibility of bulk α -RuCl₃, in which case the introduction of crystal stacking faults via thermal annealing resulted in significantly smaller and broader hysteresis loops.[93] The enhanced defect density in the α -RuCl₃ nanoflakes is most likely due to the shear forces generated during mechanical exfoliation, which are known to introduce stacking faults into 2D van der Waals materials. Notably, α -RuCl₃ is very easy to exfoliate, owing to the weak van der Waals interaction between the layers, which should render this layered material particularly sensitive against the mechanical forces exerted during exfoliation.

A low heating/cooling rate of 1 K min⁻¹ used in the present experiments ensures that the sample remains close to thermal equilibrium. Faster rates introduce stronger hysteresis arising from nonequilibrium conditions and were thus avoided.

According to the above results and discussion, charge transport measurements can be a complementary approach to probe the high temperature phase transition in the Kitaev spin

liquid candidate material α -RuCl₃.

The reliably low Ohmic contacts could be obtained by Ar milling of the contact regions on the mechanically exfoliated α -RuCl₃ nanoflakes prior to contact metal deposition. The onset of Kitaev interactions in the nanoflakes induces a change of the peak intensities and width in the temperature dependent Raman experiments while in the charge transport measurements it manifests itself in a slope change in the conductivity measurements. The Raman spectra furthermore enable the important confirmation that in the nanoflakes the α -RuCl₃ crystal structure is preserved, albeit the mechanical exfoliation introduces additional defects which together with surface strain slightly increase the phase transition temperature. The ability to reliably probe the electrical properties of α -RuCl₃ opens up intriguing further perspectives, for instance toward tuning the Kitaev-interactions via electrostatic gating.

8 Interfacial Exchange Field in Graphene/ α -RuCl₃ Heterostructures

Graphene continues to attract immense attention due to its unique electrical properties. Specifically, Dirac-like charge carriers with linear dispersion and zero rest mass impart high conductivity of this material. An intriguing feature of graphene is its unique band diagram which shows several degeneracies making it suitable for the observation of a diverse range of phenomena.[110] There is now ample experimental evidence that graphene's electronic characteristic can be effectively modified by exploiting the proximity with other 2D quantum materials. From a different perspective, graphene can be considered as a valuable probe of electronic phenomena occurring within the adjacent 2D material.[111, 112, 113] To provide the relevant background for the present experiments, the basic electronic properties of graphene are described in the following section.

Basic electronic properties of graphene

Graphene is a single layer of carbon atoms arranged in a hexagonal structure. The latter can be seen as a triangular lattice with a basis of two atoms per unit cell. The lattice vectors can be written as:

$$a_1 = \frac{a}{2}(3, \sqrt{3}), a_2 = \frac{a}{2}(3, -\sqrt{3}) \quad (8.1)$$

where $a \approx 1.42 \text{ \AA}$ is the distance between the carbon atoms. The reciprocal lattice vectors are given by:

$$b_1 = \frac{2\pi}{3a}(1, \sqrt{3}), b_2 = \frac{2\pi}{3a}(1, -\sqrt{3}) \quad (8.2)$$

Of particular interest are the two different corner points in the reciprocal lattice, namely K and K' . Using a tight binding Hamiltonian considering that electrons can hop between the

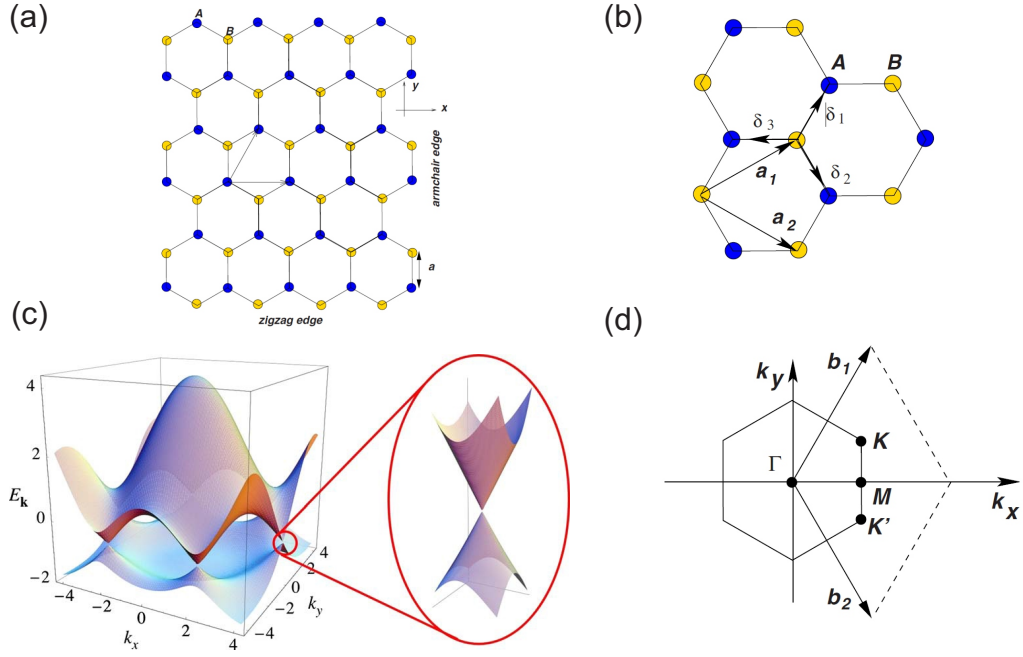


Figure 8.1 – (a) Honey comb lattice of graphene displaying zigzag and armchair edges. (b) lattice structure of graphene made out of two interpenetrating triangular lattices. (c) Electronic dispersion in graphene, the zoom shows the dispersion close to one of the Dirac points, (d) the corresponding Brillouin zone.

nearest and the next-nearest neighboring atom, the Hamiltonian can be written as

$$H = -t \sum_{\langle i,j \rangle, \sigma} (a_{\sigma,i}^\dagger b_{\sigma,j} + H.c.) - t' \sum_{\langle\langle i,j \rangle\rangle, \sigma} (a_{\sigma,i}^\dagger a_{\sigma,j} + b_{\sigma,i}^\dagger b_{\sigma,j} + H.c.) \quad (8.3)$$

where $a_{\sigma,i}$, ($a_{\sigma,i}^\dagger$) annihilates (creates) an electron with spin σ ($\sigma = \uparrow, \downarrow$) on site R_i on sublattice A, t is the nearest neighbor hopping, and t' is the next nearest neighbor hopping energy. The energy bands derived from this Hamiltonian have the form

$$E_{\pm}(\mathbf{k}) = \pm t \sqrt{3 + f(\mathbf{k})} - t' f(\mathbf{k}) \quad (8.4)$$

in which $f(\mathbf{k})$ is given by

$$f(\mathbf{k}) = 2\cos(\sqrt{3}k_y a) + 4\cos\left(\frac{\sqrt{3}}{2}k_y a\right)\cos\left(\frac{3}{2}k_x a\right) \quad (8.5)$$

where the plus sign applies to the upper (π^*) and the minus sign the lower (π) band. The dispersion relation close to the Dirac points is given by expanding the equation as $\mathbf{k} = \mathbf{K} + \mathbf{q}$,

$$E_{\pm}(\mathbf{q}) \approx \pm v_F |\mathbf{q}| \quad (8.6)$$

where \mathbf{q} is the momentum measured relative to the Dirac points and $v_F \simeq 1 \times 10^6$ is the Fermi velocity. Graphene has both, spin and valley degeneracy, with the valley degree of the freedom referring to the inequivalent pair of conical valence/conduction bands in the Brillouin zone which touch at the two Dirac points (K and K'). It is furthermore noteworthy that geometric termination of graphene results in two possible edge geometries with quite different electronic properties. Zigzag edges display a sharp density-of-states peak at the Fermi energy, endowing them with principal metallic behavior, while armchair edges can assume metallic or semiconductor behavior. From the chemical point of view, zigzag edges are more reactive than armchair edges.[110]

8.1 Nonlocality Near Graphene's Dirac Point

Nonlocal measurements have been used to probe the dynamics of population imbalance for edge modes in quantum Hall systems, as well as the spin diffusion and magnetization dynamics.[114] The main advantage of nonlocal measurements is that they allow filtering out the Ohmic contribution due to charge flow. In this manner more subtle effects that otherwise can remain unnoticed are detectable. Furthermore, the charge neutral degrees of freedom in graphene (i.e., spin and valley), which are elusive to classical electric measurements, can be accessed. Figure 8.2a displays the device geometry and electrode configuration suitable for nonlocal resistance measurements on graphene. The current flows through contacts 1 and 2 and the voltage is collected from contacts 3 and 4 leading to the resistance $R_{(NL)12,34}$. Figure 8.2c shows the nonlocal resistance of an exemplary device ($R_{(NL)12,34}$) at $B = 0$ and 12 T as a function of carrier density. At zero B-field the nonlocal resistance is about 200 Ω . However, upon applying a B-field, it strongly increases to 10 k Ω . Although the resistance magnitude varies somewhat from device-to-device and with contact geometry, nonetheless a reproducible trend was observed. In particular, The nonlocal resistance at high magnetic field generally follows the same pattern as longitudinal resistance, showing quantum Hall oscillations. However, the magnitude of the resistances at different filling factors (i.e., different carrier concentrations) are different than longitudinal resistance magnitude. This observation hints toward an additional mechanism contributing to the resistance beside the quantum Hall edge conduction channel.

As one possible explanation for the detected nonlocal resistance, a fraction of the current may flow sideways and reach the voltage electrodes. To test this assumption, using the Van der Pauw formalism it can be shown that this contribution is approximately proportional to $\rho_{xx} e^{-\frac{\pi L}{w}}$ for both zero and nonzero B.[115] Normally the devices fabricated here have a relatively long Hall bar shape with close voltage electrodes (typical $L/w > 2$). Consequently a value of $R_{NL} < 10^{-1} \Omega$ is estimated which is much smaller than the measured R_{NL} .

An alternative, more fitting explanation for this effect is called Flavor Hall effect (FHE), in which nonlocality is mediated by neutral excitations such as spin and valley flavors, and which can occur in both classical and quantum Hall regime.[115] The principle behind this effect is illustrated in Figure 8.2b which is explained for the relevance to the work done in this thesis for the case of spin. Under an applied B field, the Zeeman splitting shifts the Dirac cones for

opposite spin directions relative to each other. As a result, at the neutrality point there will exist two populations of electrons and holes with opposite spin projections. When an electric field is applied, the generated current will have a specific spin projection. The Lorentz force then creates two currents with spin-up and -down, flowing in opposite directions as depicted in Figure 8.2a.

This effect closely resembles the spin Hall effect (SHE), in which case it is the spin-orbit interaction that induces the spin currents. In graphene, the SHE can produce long range spin currents since the spin relaxations are very slow. With relaxation and scattering effects taken into account, R_{NL} depends on the device configuration, specifically on the distance between the current and the voltage electrodes (L). A general trend which is also intuitive is the decrease of R_{NL} with the distance (L). Likewise placing extra electrodes between the current and voltage electrodes causes a rapid decrease of the nonlocal resistance, such that in some cases no nonlocal resistance could be measured.

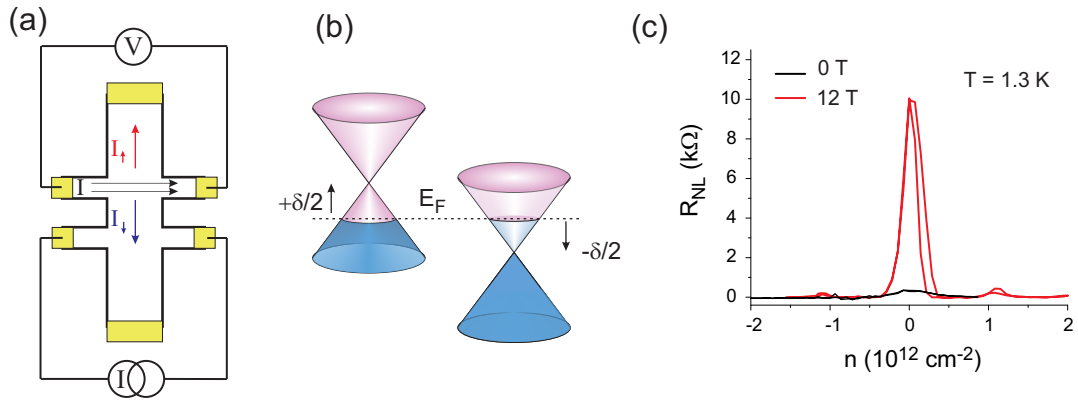


Figure 8.2 – Spin Hall effect in graphene and nonlocal transport mediated by spin diffusion. (a) Schematic of the device configuration and flow of current with different spin orientation in two different directions, (b) Zeeman spin Hall effect lifts the spin degeneracy by producing two packets of electrons and holes with different spin orientations, (c) nonlocal resistance measured in graphene.

8.1.1 Zeeman Spin Hall Effect in CVD Grown and Exfoliated Graphene

For a more detailed study of the Zeeman spin Hall effect (ZSHE) in a controlled manner, devices comprising CVD or exfoliated graphene were compared. The CVD graphene on copper, was first transferred onto SiO_x/Si substrates. Then, the clean regions of the transferred graphene is patterned into a Hall bar with desired dimensions using e-beam lithography. After patterning graphene Hall bars, another step of lithography is added to define electrodes followed by the evaporation of the metal electrodes. Figure 8.3b shows the nonlocal resistance measured from the configuration illustrated in Figure 8.3a. Without magnetic field a R_{NL} of about 1 kΩ was measured which upon applying a 12 T magnetic field increased to about 4 kΩ. That in the

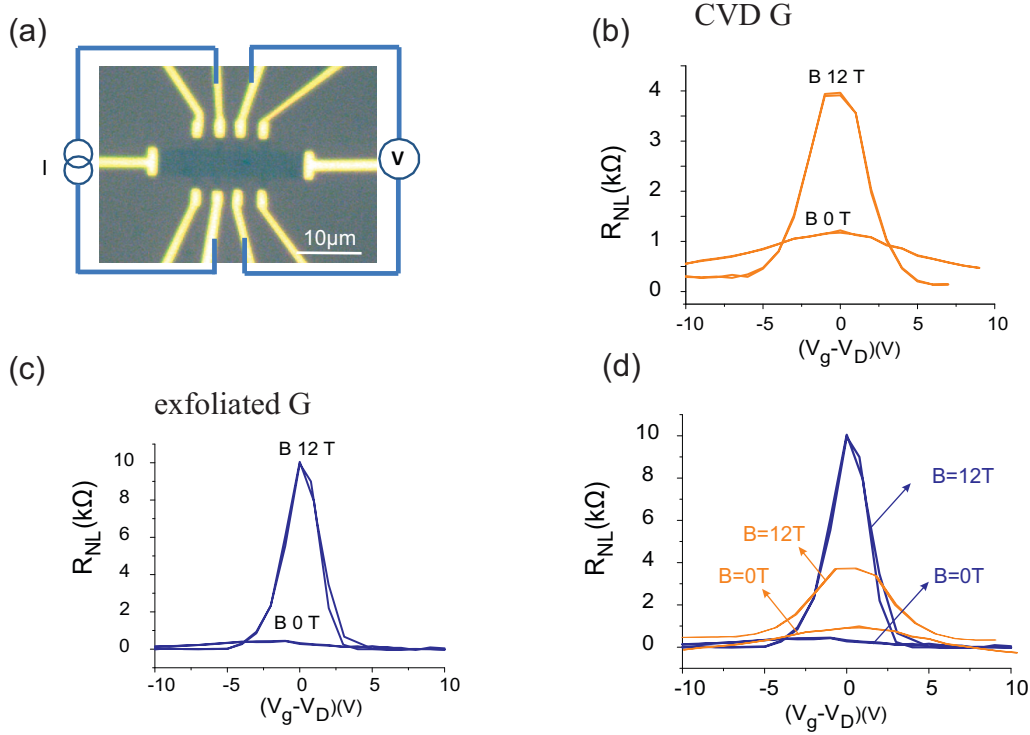


Figure 8.3 – Comparison of SHE in CVD grown and exfoliated graphene. (a) Schematic of the device configuration, (b),(c) Nonlocal resistance in CVD and exfoliated graphene, respectively, in a magnetic field and in the absence of a magnetic field, (d) comparison of the nonlocal resistances.

absence of a magnetic field, there is still a nonzero nonlocal resistance indicates the presence of the possible electron-hole puddles as well as unwanted doping in the CVD graphene. The results for analogous measurements on the exfoliated graphene are shown in (Figure 8.3c). The nonlocal resistance at zero B field is almost negligible as expected for clean graphene. Upon applying a magnetic field, a high nonlocal resistance of about 10 kΩ is reached, which is characteristic of the ZSHE. A direct comparison of the nonlocal resistances is provided by Figure 8.3d.

8.2 Magnetic Exchange Field

The spin of the electrons in graphene can be manipulated through the proximity of a magnetic material. This enables to locally modify graphene's properties without compromising its structural integrity.[116] According to the discussion in the previous section, graphene in the presence of an external magnetic field hosts the ZSHE. However, the same effect can be induced by bringing graphene in close proximity to a magnetic insulator. The magnetic exchange field (MEF) implemented in this manner allows for spatial control of spin generation, which is attractive for spintronic device applications. Vice versa, the graphene in such

heterostructures can serve as a versatile probe of the magnetic state of the interface-coupled insulator. Theoretically, the MEF can reach tens or even hundreds of Tesla. In general, owing to the short-ranged nature of the MEF, its effect will be strongest on the thinnest materials (i.e., single layers).

8.3 Graphene/ α -RuCl₃ Heterostructures

As detailed in Chapter 6, α -RuCl₃, although a spin liquid material candidate, undergoes a magnetic transition at about 7 K. Moreover, it undergoes a Mott insulator transition, such that its electrical conductivity below 80 K is negligible and the material becomes effectively insulating. These properties render α -RuCl₃ into a promising magnetic insulator to be combined with graphene. One important issue in these experiments is the cleanness of the interface and generally the quality of the underlying graphene. The first measurements were carried with CVD graphene, which later on was substituted by mechanically exfoliated graphene.

To perform the measurements in a controlled manner, always two identical CVD graphene Hall bars were fabricated (from the same CVD batch). In the next step, the α -RuCl₃ nanoflakes were exfoliated from the bulk crystal on top of a PDMS stamp. Having the final graphene

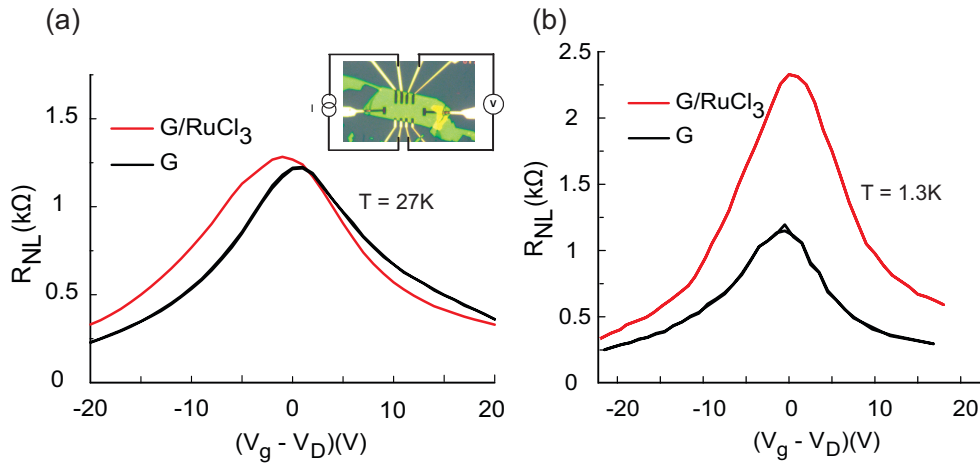


Figure 8.4 – (a) The nonlocal resistance of both CVD graphene and G/ α -RuCl₃ Hall bars at 27 K. The inset shows the device configuration for both Hall bars. (b) The nonlocal resistance in CVD graphene and G/RuCl₃ at 1.3 K, below the RuCl₃ magnetic transition temperature.

Hall bar, the exfoliated α -RuCl₃ flakes are transferred on top of the Hall bar using a transfer stage. The home-built transfer stage used for this purpose comprises a micromanipulator with piezoelectric stages for positioning. The optical microscope the position of both graphene Hall bar and the exfoliated α -RuCl₃ is determined and a heating system gives the ability to control the adhesion of the PDMS stamp. By Raman spectroscopy, the integrity of the underlying graphene could be confirmed. The exfoliated α -RuCl₃ nanosheet was transferred only on top of one of the CVD graphene Hall bars while the other Hall bar on the same substrate remained intact. Figure 8.4a compares the measured nonlocal resistance of both Hall bars without

magnetic field at $T = 27$ K, above the magnetic ordering temperature of the α -RuCl₃. There is no clear enhancement of the nonlocal resistance in the G/ α -RuCl₃ heterostructures. By contrast, as depicted in Figure 8.4b, upon further cooling the sample, the nonlocal resistance of the latter exceeds that of graphene. The same observation was reproducibly made on several devices.

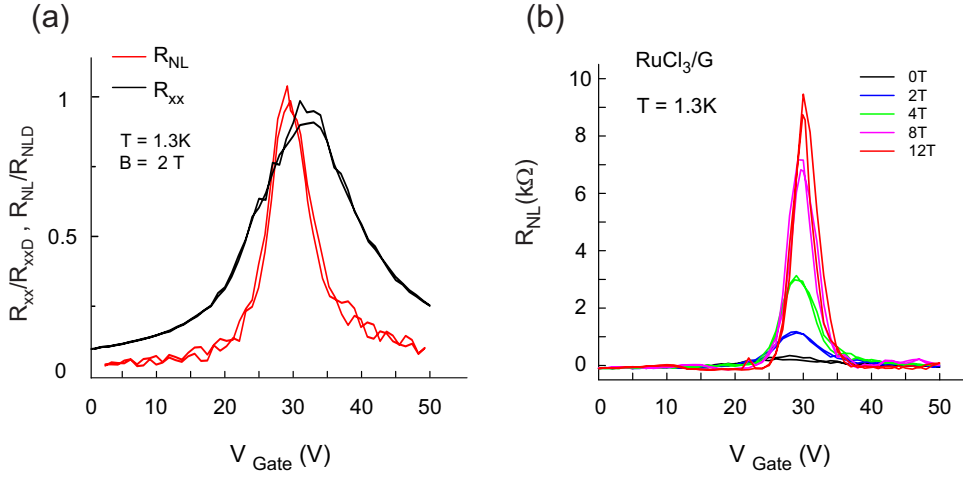


Figure 8.5 – (a) The normalized R_{NL} and R_{xx} of a G/ α -RuCl₃ at 1.3 K and in the presence of a 2 T magnetic field. (b) The nonlocal resistance evolution in the presence of an external magnetic field at base temperature.

From the normalized resistance in Figure 8.5a, a narrower curve is seen for the nonlocal vs. longitudinal resistance, indicating a negligible contribution of the contact resistances in the nonlocal resistance. According to Ohm's law, the nonlocal resistance is proportional to R_{xx} and the relation between the two is given by:[115]

$$R_{nl,\Omega} \sim R_{xx} \frac{w}{\pi l} \ln \left[\frac{\cosh(\frac{\pi l}{w} + 1)}{\cosh(\frac{\pi l}{w} - 1)} \right] \quad (8.7)$$

where w is the channel width and l is the distance between the current and voltage probes. For the device in Figure 8.7, $w/l = 1/2$. Inserting this value into equation 8.7, at $B = 2$ T $R_{nl} \sim 70 \Omega$, which is much smaller compared to $R_{nl} = 2$ kΩ. Figure 8.7b displays the magnetic field evolution of the nonlocal resistance at 1.3 K. By increasing the magnetic field R_{NL} increases as expected from the ZSHE.

The above measurements were repeated on the graphene/RuCl₃ heterostructure comprising mechanically exfoliated graphene which is expected to have a better quality and hence higher mobility.

As exemplified from Figure 8.6a for such a sample, a significant enhancement of the nonlocal resistance is observed already in the absence of an external magnetic field. Moreover, the R_{NL}

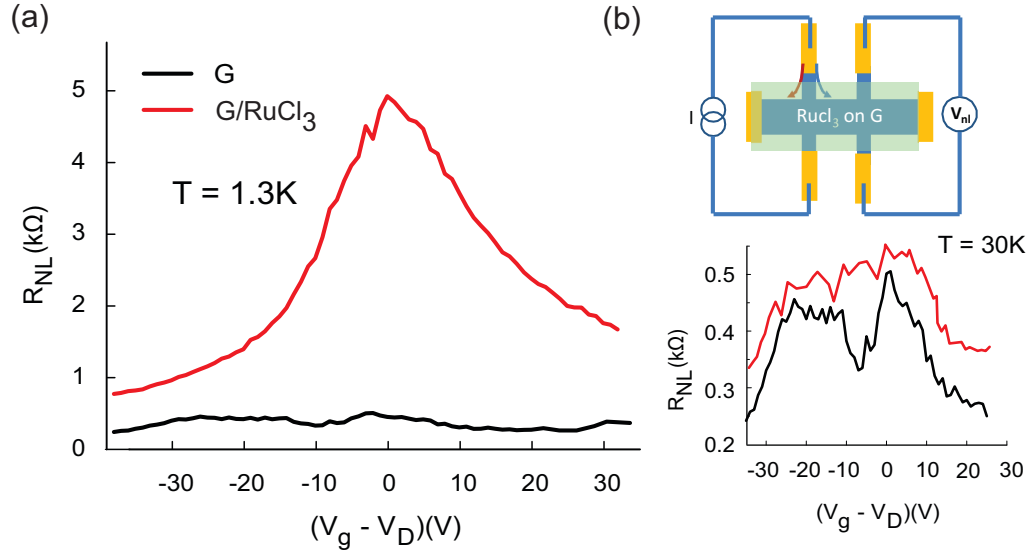


Figure 8.6 – (a) The nonlocal resistance of exfoliated graphene and G/ α -RuCl₃ Hall bars at 1.3 K. (b) The schematic of the device and the nonlocal resistance for both Hall bars at 30 K.

for the bare graphene at zero magnetic field now is almost zero indicative of less scattering centers in graphene. Upon increasing the temperature to $T = 30$ K, the nonlocal resistance of the heterostructure device almost completely vanishes, (Figure 8.6b). In Figure 8.7, the B-field dependency between the two different types of bare graphene, as well as the corresponding heterostructures are compared. Generally, by increasing the magnetic field, the nonlocal resistance increases much stronger in the heterostructure than the case of pristine graphene.

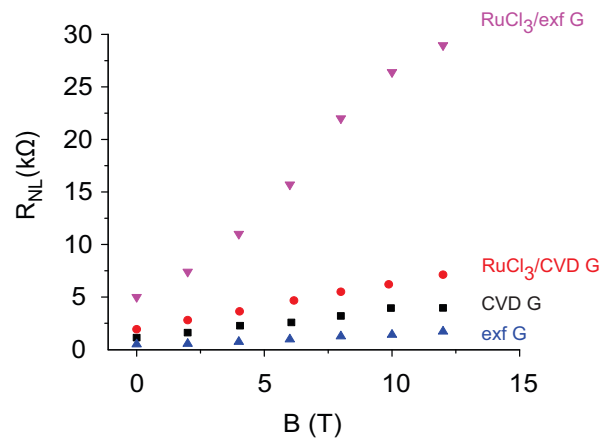


Figure 8.7 – The magnetic field evolution of the nonlocal resistance of the G/ α -RuCl₃ at the Dirac point for CVD and exfoliated graphene.

In the quantum Hall regime the exfoliated graphene shows pronounced oscillations of R_{xx} with values approaching zero between the filled Landau levels at high B-field (see Figure 8.8).

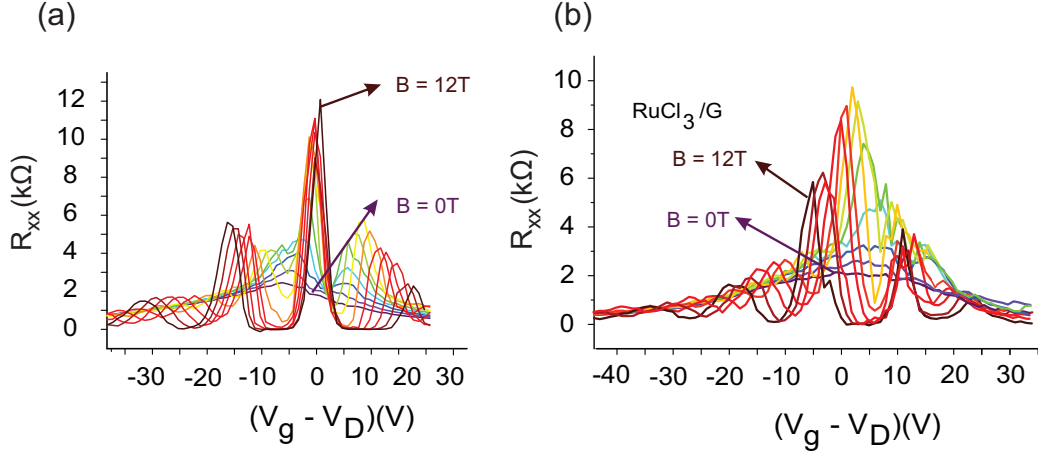


Figure 8.8 – (a) Longitudinal resistance (R_{xx}) of exfoliated graphene at different magnetic fields. (b) R_{xx} of $G/\alpha\text{-RuCl}_3$ at $T = 1.3\text{ K}$ for different magnetic fields.

As an important difference, the corresponding heterostructure displays a reduced R_{xx} at the charge neutrality point (see Figure 8.9a). This decrease becomes stronger with increasing B -field, in sharp contrast to the pristine graphene, for which $R_{xx,D}$ slightly increases with B -field due to the magnetically induced energy gap and as a result absence of a conducting channel. However, in the case of the graphene/ $\alpha\text{-RuCl}_3$ heterostructures, the reduction of the $R_{xx,D}$ with magnetic field points toward the existence of a conducting channel at the Fermi level.

An explanation for this effect is provided in Figure 8.9b and c. In principle, the insulating behavior of the graphene at the neutrality point ($\nu = 0$) can have two possible reasons. One option is that the valley energy exceeds the Zeeman splitting with the resulting valley polarization opening a gap at the Fermi level. Toward the sheet edges, the valley polarized states would separate even further in energy, such that insulating behavior emerges within the entire sheet including the edges. In the second option, the Zeeman splitting would be so strong that it exceeds the valley splitting, and as a consequence the Dirac cones of opposite spin would shift in respect to the Fermi energy. As depicted in Figure 8.9c, this leads to the crossing of the states near the graphene's sheet edges, which in turn would make the edge states available for conduction. This second option is in agreement with the experimentally observed reduction of R_{xx} in the exfoliated graphene/ $\alpha\text{-RuCl}_3$ heterostructures.

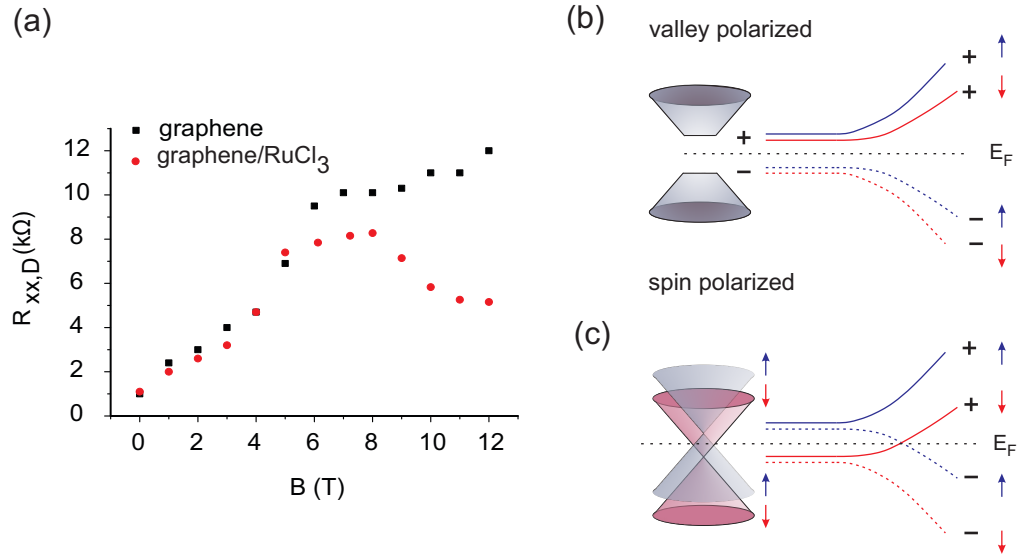


Figure 8.9 – (a) Magnetic field evolution of the R_{xx} at the Dirac point for both pristine graphene and G/ α -RuCl₃. In the case of graphene the nonlocal resistance at the Dirac point continues to increase while for G/ α -RuCl₃ at about 7 T decreases, (b) schematic of valley and (c) spin polarization of the Dirac cone.

9 Summary and Outlook

In this thesis, two different types of spin-orbit coupled materials, namely 3D topological insulators (3D TIs) in the weak correlation regime and the magnetic Mott insulator α - RuCl_3 in the strong correlation regime, were investigated. The strong spin-orbit coupling in TIs as an example of Dirac materials gives rise to topologically protected surface states. The suppression of back scattering in the edge or surface states renders these materials promising for novel and exciting spintronic device applications. This includes intriguing perspectives for optospintronic, as helical light can be used to generate spin-polarized currents in TIs. Furthermore, owing to their unique energy band structure they are of interest to be implemented in thermoelectric applications. In fact, bismuth chalcogenide-based 3D TIs are among the best thermoelectric materials. TIs share this interesting character with other Dirac materials like graphene, which has been shown to have a higher electronic temperature than lattice temperature under optical excitations, thus rendering it suitable for hot carrier generation and thermoelectrics.

In the weak correlation regime, materials like α - RuCl_3 have attracted great attention due to their exotic low energy excitations including chargeless spinons emergent from spin fractionalization. α - RuCl_3 is particularly appealing as its exactly solvable Kitaev model on the honeycomb lattice enables a detailed study of possible topological spin liquids and fractional quasiparticles. In addition, quantum spin liquid states have been suggested to play a crucial role in high-temperature superconductivity. Furthermore, by implementing thin sheets of such type of material into van der Waals heterostructures novel interfacial coupling phenomena could be explored.

The first part of this thesis was devoted to the fabrication and characterization of nanoplatelets made of $\text{Bi}_2\text{Te}_2\text{Se}$ as n-type and Sb_2Te_3 as p-type 3D TI. After their successful CVD growth, individual $\text{Bi}_2\text{Te}_2\text{Se}$ and Sb_2Te_3 nanoplatelets were studied mainly by magnetotransport measurements. Furthermore, with the aim of achieving high quality TIs with high carrier mobility and reduced bulk charge carriers, the two compounds were grown on hBN nanosheets instead of the Si/SiO₂ substrates.

Building upon the above results on the single component devices, also heterostructures composed of BTS and Sb_2Te_3 were investigated. Since the thermoelectric efficiency of devices is limited by the thermoelectric power of the materials incorporated, the need for designing more sophisticated materials and incorporating them in heterostructures is apparent. To this end, lateral BTS/ Sb_2Te_3 heterostructures were grown using specifically adjusted CVD growth parameters to control the relative lateral extensions and thicknesses. The controlled growth of the TI lateral heterostructures enables tuning the thermoelectric response of the devices. Investigation of the photoresponse of the heterostructure devices by scanning photocurrent microscopy revealed pronounced photocurrents of hundreds of μA . This response exceeds that reported for lateral p-n heterojunctions of gated graphene by about three orders of magnitude. Moreover, the TI lateral heterostructures show an enhanced photothermoelectric response with Seebeck coefficients exceeding $230 \mu\text{V/K}$.

Besides the efficient thermoelectric power generation of such heterojunctions, they could be used as coolers in integrated circuits. It is known that the efficiency of solar cells degrades with an increase of the local temperature and hence under strong sunshine a cooling mechanism is necessary. In thermoelectric power generation, diffusive heat flow and the Peltier effect are additive. Both these effects reduce the temperature difference between the hot and cold zone. Integrating the TI p-n junctions fabricated and studied in this thesis into photovoltaic solar cells not only could enhance the efficiency of the solar cells, but at the same time the extra heat could be converted into electricity. Further improvement may be achieved by growing the TI p-n junctions on hBN sheets. The advantage of such a configuration is the simultaneous increase of electrical and thermal conductivity which is expected to lead to a better cooler through an enhanced Peltier effect. In addition, by tuning the Fermi level of the constituent TIs in the heterostructure, the electronic properties of the surface states could be exploited to achieve even higher efficiencies.

The second part of this thesis focused on the electrical properties of the Kitaev material $\alpha\text{-RuCl}_3$. Theoretical studies indicate that due to its close-to-perfect 2D honeycomb lattice structure, it harbors the Kitaev interactions. Substantial experimental evidence for fractionalized excitations in the bulk of this material has been gained by neutron scattering experiments as well as Raman experiments. Specifically, an unusual temperature evolution of the width of certain Raman peaks, which deviates from conventional bosonic behavior has been reported. In this thesis, the aim was to explore this phenomenon in mechanically exfoliated thin sheets of $\alpha\text{-RuCl}_3$. The recorded Raman spectra exhibited the same signatures of fractionalized excitations like for the bulk. However, the onset of the deviation from the bosonic behavior occurred at somewhat higher temperature.

Furthermore, a reliable method was developed to electrically contact individual $\alpha\text{-RuCl}_3$ thin sheets, which enabled evaluating subtle changes of their resistivity with temperature. In agreement with theory, a Mott insulator behavior was observed, with a change of the hopping transport characteristic occurring at approximately the same temperature as the onset of spin-phonon interactions in the Raman spectra. These observations hint toward the

entanglement between the structure and magnetism in α -RuCl₃. The ability to electrically contact this material opens up the opportunity to incorporate it in nanodevices, and exploit its fundamental fractionalized spinons for future device applications.

As another perspective, the competition between the spin-orbit coupling and electronic correlation may provide access to an unconventional high temperature type of superconductivity in α -RuCl₃. In fact in 1987, Laughlin et al. showed that the ground state of the frustrated Heisenberg antiferromagnet in two dimensions and the fractional quantum Hall state for bosons can be adiabatically evolved into each other without crossing a phase boundary. Laughlin argued that a gas of particles obeying 1/2 statistics might actually be a superconductor with a charge-2 order parameter. This possibility gains support by the recent observation of a superconductive phase in Sr₂RuO₄, which likewise is a candidate to feature a spin liquid ground state. For α -RuCl₃, this task may be achieved by tuning the electron correlation strength via electrostatic gating. In future experiments, a sufficiently strong carrier modulation might be reached by polymer electrolyte gating. Thus, by bringing the α -RuCl₃ in close proximity to the spin liquid ground state, it may enter the superconductivity regime.

The α -RuCl₃ nanosheets were furthermore combined with graphene into a novel type of vertical van der Waals heterostructure. Here, the major objective was to test whether an interfacial magnetic exchange coupling can be imparted onto the graphene. Such effect could indeed be observed in low-temperature magnetotransport measurement on individual graphene/ α -RuCl₃ heterostructures. It manifests itself in the generation of spin currents even in the absence of an external magnetic field. This achievement opens the door for novel spintronic devices where spin generation occurs in the absence of an external magnetic field by an all-electrical means. Another motivation to investigate the graphene/ α -RuCl₃ heterostructures was to gain information about the spin arrangement not in the bulk, but at the terminated surface of α -RuCl₃, as inferred from the magnetotransport properties of such devices. For heterostructure devices comprising either CVD or exfoliated graphene, the strength of the magnetic exchange field was found to sensitively depend on the quality of the interface. The demonstration that the magnetic insulator α -RuCl₃ can induce appreciable spin interactions in graphene provides a valuable basis for exploring a similar effect in combination with other 2D quantum materials. An exciting future option would be to achieve a sufficiently strong interfacial spin-orbit coupling between graphene and α -RuCl₃. This represents a promising strategy to increase the minute band gap in graphene and at the same time render its 1D topological edge states robust. The successful conversion of graphene into a robust quantum spin Hall insulator would hold great promise for novel spintronic applications.

Bibliography

- [1] Simon Trebst. Kitaev Materials. *arXiv preprint arXiv:1701.07056*.
- [2] K. v. Klitzing, G. Dorda, and M. Pepper. New method for high-accuracy determination of the fine-structure constant based on quantized hall resistance. *Phys. Rev. Lett.*, 45:494–497, Aug 1980.
- [3] Liang Fu and C. L. Kane. Topological insulators with inversion symmetry. *Phys. Rev. B*, 76:045302, Jul 2007.
- [4] Markus König, Steffen Wiedmann, Christoph Brüne, Andreas Roth, Hartmut Buhmann, Laurens W. Molenkamp, Xiao-Liang Qi, and Shou-Cheng Zhang. Quantum spin hall insulator state in hgte quantum wells. *Science*, 318(5851):766–770, 2007.
- [5] M Z Hasan and C L Kane. Colloquium : Topological insulators. *Reviews of Modern Physics*, 82(4):3045–3067, 2010.
- [6] Huibo B Cao, A Banerjee, J-Q Yan, C A Bridges, M D Lumsden, D G Mandrus, D A Tennant, B C Chakoumakos, and S E Nagler. Low-temperature crystal and magnetic structure of α -RuCl₃. *Physical Review B*, 93(13):134423, 2016.
- [7] M. Z. Hasan and C. L. Kane. Colloquium: Topological insulators. *Rev. Mod. Phys.*, 82:3045–3067, Nov 2010.
- [8] B Keimer and J E Moore. The physics of quantum materials. *Nature Physics*, 13:1045, oct 2017.
- [9] A Glamazda, P Lemmens, S H. Do, Y S Choi, and K Y. Choi. Raman spectroscopic signature of fractionalized excitations in the harmonic-honeycomb iridates β - and γ -Li₂IrO₃. *Nature Communications*, 7:12286, jul 2016.
- [10] Luke J. Sandilands, Yao Tian, Kemp W. Plumb, Young-June Kim, and Kenneth S. Burch. Scattering continuum and possible fractionalized excitations in α -rucl₃. *Phys. Rev. Lett.*, 114:147201, Apr 2015.
- [11] Xiaoqing Zhou, Haoxiang Li, J. A. Waugh, S. Parham, Heung-Sik Kim, J. A. Sears, A. Gomes, Hae-Young Kee, Young-June Kim, and D. S. Dessau. Angle-resolved photoemission study of the kitaev candidate α – rucl₃. *Phys. Rev. B*, 94:161106, Oct 2016.

Bibliography

- [12] R.B. Laughlin. Primitive and composite ground states in the fractional quantum hall effec. *Surface Science*, 142(1):163 – 172, 1984.
- [13] William Witczak-Krempa, Gang Chen, Yong Baek Kim, and Leon Balents. Correlated quantum phenomena in the strong spin-orbit regime. *Annual Review of Condensed Matter Physics*, 5(1):57–82, 2014.
- [14] Seung-Hwan Do, Sang-Youn Park, Junki Yoshitake, Joji Nasu, Yukitoshi Motome, Yong Seung Kwon, D T Adroja, D J Voneshen, Kyoo Kim, T-H Jang, and Others. Incarnation of Majorana Fermions in Kitaev Quantum Spin Lattice. *arXiv preprint arXiv:1703.01081*, 2017.
- [15] A Glamazda, P Lemmens, S-H Do, Y S Kwon, and K-Y Choi. Relation between kitaev magnetism and structure in α - RuCl₃. *Physical Review B*, 95(17):174429, 2017.
- [16] Xiao-Gang Wen. Topological order and edge structure of $\nu=1/2$ quantum hall state. *Phys. Rev. Lett.*, 70:355–358, Jan 1993.
- [17] Shun-Qing Shen. *Topological Insulators*. Springer-Verlag Berlin Heidelberg, 2012.
- [18] R. B. Laughlin. Quantized hall conductivity in two dimensions. *Phys. Rev. B*, 23:5632–5633, May 1981.
- [19] Marcel Franz and Molenkamp Laurens. *Chemical vapor deposition*. Elsevier, 2013.
- [20] J. Zak. Berry's phase for energy bands in solids. *Phys. Rev. Lett.*, 62:2747–2750, Jun 1989.
- [21] Quantal phase factors accompanying adiabatic changes. *Proceedings of the Royal Society of London A: Mathematical, Physical and Engineering Sciences*, 392(1802):45–57, 1984.
- [22] F. D. M. Haldane. Model for a quantum hall effect without landau levels: Condensed-matter realization of the "parity anomaly". *Phys. Rev. Lett.*, 61:2015–2018, Oct 1988.
- [23] Roger S. K. Mong and Vasudha Shivamoggi. Edge states and the bulk-boundary correspondence in dirac hamiltonians. *Phys. Rev. B*, 83:125109, Mar 2011.
- [24] R. B. Laughlin. Anomalous quantum hall effect: An incompressible quantum fluid with fractionally charged excitations. *Phys. Rev. Lett.*, 50:1395–1398, May 1983.
- [25] C. L. Kane and E. J. Mele. Quantum spin hall effect in graphene. *Phys. Rev. Lett.*, 95:226801, Nov 2005.
- [26] B. Andrei Bernevig, Taylor L. Hughes, and Shou-Cheng Zhang. Quantum spin hall effect and topological phase transition in hgte quantum wells. *Science*, 314(5806):1757–1761, 2006.
- [27] Haijun Zhang, Chao-Xing Liu, Xiao-Liang Qi, Xi Dai, Zhong Fang, and Shou-Cheng Zhang. Topological insulators in Bi₂Se₃, Bi₂Te₃ and Sb₂Te₃ with a single Dirac cone on the surface. *Nat Phys*, 5(6):438–442, 2009.

-
- [28] Yi Zhou, Kazushi Kanoda, and Tai-Kai Ng. Quantum spin liquid states. *Rev. Mod. Phys.*, 89:025003, Apr 2017.
- [29] Stephen M Winter, Alexander A Tsirlin, Maria Daghofer, Jeroen van den Brink, Yogesh Singh, Philipp Gegenwart, and Roser Valentí. Models and materials for generalized kitaev magnetism. *Journal of Physics: Condensed Matter*, 29(49):493002, 2017.
- [30] I. I. Mazin, S. Manni, K. Foyevtsova, Harald O. Jeschke, P. Gegenwart, and Roser Valentí. Origin of the insulating state in honeycomb iridates and rhodates. *Phys. Rev. B*, 88:035115, Jul 2013.
- [31] G. Jackeli and G. Khaliullin. Mott insulators in the strong spin-orbit coupling limit: From heisenberg to a quantum compass and kitaev models. *Phys. Rev. Lett.*, 102:017205, Jan 2009.
- [32] Jiří Chaloupka, George Jackeli, and Giniyat Khaliullin. Kitaev-heisenberg model on a honeycomb lattice: Possible exotic phases in iridium oxides $A_2\text{IrO}_3$. *Phys. Rev. Lett.*, 105:027204, Jul 2010.
- [33] Dorota Gotfryd, Juraj Rusnačko, Krzysztof Wohlfeld, George Jackeli, Jiří Chaloupka, and Andrzej M. Oleś. Phase diagram and spin correlations of the kitaev-heisenberg model: Importance of quantum effects. *Phys. Rev. B*, 95:024426, Jan 2017.
- [34] A Banerjee, C A Bridges, J-Q Yan, A A Aczel, L Li, M B Stone, G E Granroth, M D Lumsden, Y Yiu, J Knolle, and Others. Proximate Kitaev quantum spin liquid behaviour in a honeycomb magnet. *Nature materials*, 15(7):733–740, 2016.
- [35] Yuriy Sizyuk, Craig Price, Peter Wölfle, and Natalia B. Perkins. Importance of anisotropic exchange interactions in honeycomb iridates: Minimal model for zigzag antiferromagnetic order in Na_2IrO_3 . *Phys. Rev. B*, 90:155126, Oct 2014.
- [36] T. Takayama, A. Kato, R. Dinnebier, J. Nuss, H. Kono, L. S. I. Veiga, G. Fabbri, D. Haskel, and H. Takagi. Hyperhoneycomb iridate $\beta\text{-Li}_2\text{IrO}_3$ as a platform for kitaev magnetism. *Phys. Rev. Lett.*, 114:077202, Feb 2015.
- [37] Yogesh Singh and P. Gegenwart. Antiferromagnetic mott insulating state in single crystals of the honeycomb lattice material Na_2IrO_3 . *Phys. Rev. B*, 82:064412, Aug 2010.
- [38] R. Comin, G. Levy, B. Ludbrook, Z.-H. Zhu, C. N. Veenstra, J. A. Rosen, Yogesh Singh, P. Gegenwart, D. Stricker, J. N. Hancock, D. van der Marel, I. S. Elfimov, and A. Damascelli. Na_2IrO_3 as a novel relativistic mott insulator with a 340-meV gap. *Phys. Rev. Lett.*, 109:266406, Dec 2012.
- [39] Jiří Chaloupka, George Jackeli, and Giniyat Khaliullin. Zigzag magnetic order in the iridium oxide Na_2IrO_3 . *Phys. Rev. Lett.*, 110:097204, Feb 2013.

Bibliography

- [40] Vamshi M Katukuri, S Nishimoto, V Yushankhai, A Stoyanova, H Kandpal, Sungkyun Choi, R Coldea, I Rousochatzakis, L Hozoi, and Jeroen van den Brink. Kitaev interactions between $j = 1/2$ moments in honeycomb Na_2IrO_3 are large and ferromagnetic: insights from ab initio quantum chemistry calculations. *New Journal of Physics*, 16(1):013056, 2014.
- [41] Yogesh Singh, S. Manni, J. Reuther, T. Berlijn, R. Thomale, W. Ku, S. Trebst, and P. Gegenwart. Relevance of the heisenberg-kitaev model for the honeycomb lattice iridates A_2IrO_3 . *Phys. Rev. Lett.*, 108:127203, Mar 2012.
- [42] Sae Hwan Chun, Jong-Woo Kim, Jungho Kim, H Zheng, Constantinos C. Stoumpos, C. D. Malliakas, J. F. Mitchell, Kavita Mehlawat, Yogesh Singh, Y Choi, T Gog, A Al-Zein, M. Moretti Sala, M Krisch, J Chaloupka, G Jackeli, G Khaliullin, and B J Kim. Direct evidence for dominant bond-directional interactions in a honeycomb lattice iridate Na_2IrO_3 . *Nature Physics*, 11:462, may 2015.
- [43] S. K. Choi, R. Coldea, A. N. Kolmogorov, T. Lancaster, I. I. Mazin, S. J. Blundell, P. G. Radaelli, Yogesh Singh, P. Gegenwart, K. R. Choi, S.-W. Cheong, P. J. Baker, C. Stock, and J. Taylor. Spin waves and revised crystal structure of honeycomb iridate Na_2IrO_3 . *Phys. Rev. Lett.*, 108:127204, Mar 2012.
- [44] I. Pollini. Electronic properties of the narrow-band material $\alpha\text{-RuCl}_3$. *Phys. Rev. B*, 53:12769–12776, May 1996.
- [45] Luke J. Sandilands, Yao Tian, Anjan A. Reijnders, Heung-Sik Kim, K. W. Plumb, Young-June Kim, Hae-Young Kee, and Kenneth S. Burch. Spin-orbit excitations and electronic structure of the putative kitaev magnet $\alpha\text{-RuCl}_3$. *Phys. Rev. B*, 93:075144, Feb 2016.
- [46] Jong-Hee Park. *Topological Insulators*. Materials Park, 2001.
- [47] X.-T. Yan and Y. Xu. *Chemical Vapour Deposition, An Integrated Engineering Design for Advanced*. Springer, 2010.
- [48] Daniel Dobkin and M.K. Zuraw. *Principles of Chemical Vapor Deposition*. Springer Netherlands, 2003.
- [49] Ewen Smith and Geoffrey Dent. *Modern Raman Spectroscopy: A Practical Approach*. Wiley, 2013.
- [50] J. Volger. Note on the hall potential across an inhomogeneous conductor. *Phys. Rev.*, 79:1023–1024, Sep 1950.
- [51] Thomas Ihn. *Semiconductor Nanostructures*. Springer, 2009.
- [52] Madhab Neupane, Su-Yang Xu, Yukiaki Ishida, Shuang Jia, Benjamin M. Fregoso, Chang Liu, Ilya Belopolski, Guang Bian, Nasser Alidoust, Tomasz Durakiewicz, Victor Galitski, Shik Shin, Robert J. Cava, and M. Zahid Hasan. Gigantic surface lifetime of an intrinsic topological insulator. *Phys. Rev. Lett.*, 115:116801, Sep 2015.

-
- [53] C. Pauly, G. Bihlmayer, M. Liebmann, M. Grob, A. Georgi, D. Subramaniam, M. R. Scholz, J. Sánchez-Barriga, A. Varykhalov, S. Blügel, O. Rader, and M. Morgenstern. Probing two topological surface bands of Sb_2Te_3 by spin-polarized photoemission spectroscopy. *Phys. Rev. B*, 86:235106, Dec 2012.
- [54] Yao Tian, Gavin B. Osterhoudt, Shuang Jia, R. J. Cava, and Kenneth S. Burch. Local phonon mode in thermoelectric Bi_2Te_3 from charge neutral antisites. *Applied Physics Letters*, 108(4):041911, 2016.
- [55] Ana Akrap, Michaël Tran, Alberto Ubaldini, Jérémie Teyssier, Enrico Giannini, Dirk van der Marel, Philippe Lerch, and Christopher C. Homes. Optical properties of Bi_2Te_3 at ambient and high pressures. *Phys. Rev. B*, 86:235207, Dec 2012.
- [56] Shinobu Hikami, Anatoly I. Larkin, and Yosuke Nagaoka. Spin-orbit interaction and magnetoresistance in the two dimensional random system. *Progress of Theoretical Physics*, 63(2):707–710, 1980.
- [57] Tsuneya Ando. Theory of quantum transport in a two-dimensional electron system under magnetic fields. iv. oscillatory conductivity. *Journal of the Physical Society of Japan*, 37(5):1233–1237, 1974.
- [58] Dong-Xia Qu, Y. S. Hor, Jun Xiong, R. J. Cava, and N. P. Ong. Quantum oscillations and hall anomaly of surface states in the topological insulator Bi_2Te_3 . *Science*, 329(5993):821–824, 2010.
- [59] Jing Wang, Xi Chen, Bang-Fen Zhu, and Shou-Cheng Zhang. Topological p - n junction. *Phys. Rev. B*, 85:235131, Jun 2012.
- [60] Fengnian Xia, Han Wang, Di Xiao, Madan Dubey, and Ashwin Ramasubramaniam. Two-dimensional material nanophotonics. *Nat Photon*, 8(12):899–907, 2014.
- [61] Kin Fai Mak, Changgu Lee, James Hone, Jie Shan, and Tony F. Heinz. Atomically thin MoS_2 : A new direct-gap semiconductor. *Phys. Rev. Lett.*, 105:136805, Sep 2010.
- [62] Xiaomu Wang, Zhenzhou Cheng, Ke Xu, Hon Ki Tsang, and Jian-Bin Xu. High-responsivity graphene/silicon-heterostructure waveguide photodetectors. *Nature Photonics*, 7:888, sep 2013.
- [63] Ali Sobhani, Adam Lauchner, Sina Najmaei, Ciceron Ayala-Orozco, Fangfang Wen, Jun Lou, and Naomi J. Halas. Enhancing the photocurrent and photoluminescence of single crystal monolayer MoS_2 with resonant plasmonic nanoshells. *Applied Physics Letters*, 104(3):031112, 2014.
- [64] H. Julian Goldsmid. *Introduction to Thermoelectricity*. Springer-Verlag Berlin Heidelberg, 2010.
- [65] Kunihiro Koumoto and Takao Mori. *Thermoelectric Nanomaterials*. Springer-Verlag Berlin Heidelberg, 2013.

- [66] Joseph P. Heremans, Vladimir Jovovic, Eric S. Toberer, Ali Saramat, Ken Kurosaki, Anek Charoenphakdee, Shinsuke Yamanaka, and G. Jeffrey Snyder. Enhancement of thermoelectric efficiency in pbte by distortion of the electronic density of states. *Science*, 321(5888):554–557, 2008.
- [67] Pouyan Ghaemi, Roger S. K. Mong, and J. E. Moore. In-plane transport and enhanced thermoelectric performance in thin films of the topological insulators bi_2te_3 and bi_2se_3 . *Phys. Rev. Lett.*, 105:166603, Oct 2010.
- [68] Nicki F. Hinsche, Sebastian Zastrow, Johannes Gooth, Laurens Pudewill, Robert Zierold, Florian Rittweger, Tomáš Rauch, Jürgen Henk, Kornelius Nielsch, and Ingrid Mertig. Impact of the topological surface state on the thermoelectric transport in sb_2te_3 thin films. *ACS Nano*, 9(4):4406–4411, 2015. PMID: 25826737.
- [69] Ji Ho Sung, Hoseok Heo, Inchan Hwang, Myungsoo Lim, Donghun Lee, Kibum Kang, Hee Cheul Choi, Jae-Hoon Park, Seung-Hoon Jhi, and Moon-Ho Jo. Atomic Layer-by-Layer Thermoelectric Conversion in Topological Insulator Bismuth/Antimony Tellurides. *Nano Letters*, 14(7):4030–4035, 2014.
- [70] Yuan Yan, Zhi-Min Liao, Xiaoxing Ke, Gustaaf Van Tendeloo, Qincheng Wang, Dong Sun, Wei Yao, Shuyun Zhou, Liang Zhang, Han-Chun Wu, and Da-Peng Yu. Topological Surface State Enhanced Photothermoelectric Effect in Bi_2Se_3 Nanoribbons. *Nano Letters*, 14(8):4389–4394, 2014.
- [71] Zilong Jiang, Cui-Zu Chang, Massoud Ramezani Masir, Chi Tang, Yadong Xu, Jagadeesh S Moodera, Allan H MacDonald, and Jing Shi. Enhanced spin Seebeck effect signal due to spin-momentum locked topological surface states. *Nature Communications*, 7:11458, 2016.
- [72] Yang L. Han G. Zou J. Hong M., Chen Zhi-Gang. Enhanced Thermoelectric Performance of Ultrathin Bi_2Se_3 Nanosheets through Thickness Control. *Advanced Electronic Materials*, 1(6):1500025.
- [73] Martin Lanius, Jörn Kampmeier, Christian Weyrich, Sebastian Kölling, Melissa Schall, Peter Schüffelgen, Elmar Neumann, Martina Luysberg, Gregor Mussler, Paul M Koenraad, Thomas Schäpers, and Detlev Grützmacher. P–N Junctions in Ultrathin Topological Insulator $\text{Sb}_2\text{Te}_3/\text{Bi}_2\text{Te}_3$ Heterostructures Grown by Molecular Beam Epitaxy. *Crystal Growth & Design*, 16(4):2057–2061, 2016.
- [74] Yuho Min, Gyeongbae Park, Bongsoo Kim, Anupam Giri, Jie Zeng, Jong Wook Roh, Sang Il Kim, Kyu Hyung Lee, and Unyong Jeong. Synthesis of Multishell Nanoplates by Consecutive Epitaxial Growth of Bi_2Se_3 and Bi_2Te_3 Nanoplates and Enhanced Thermoelectric Properties. *ACS Nano*, 9(7):6843–6853, 2015.
- [75] Yanbin Li, Jinsong Zhang, Guangyuan Zheng, Yongming Sun, Seung Sae Hong, Feng Xiong, Shuang Wang, Hye Ryoung Lee, and Yi Cui. Lateral and Vertical Two-Dimensional Layered Topological Insulator Heterostructures. *ACS Nano*, 9(11):10916–10921, 2015.

-
- [76] D Niesner, S Otto, Th Fauster, E V Chulkov, S V Eremeev, O E Tereshchenko, and K A Kokh. Electron dynamics of unoccupied states in topological insulators. *Journal of Electron Spectroscopy and Related Phenomena*, 195:258–262, 2014.
 - [77] Kyung-Hwan Jin, Han Woong Yeom, and Seung-Hoon Jhi. Band structure engineering of topological insulator heterojunctions. *Physical Review B*, 93(7):75308, 2016.
 - [78] Soudabeh Mashhadi, Dinh Loc Duong, Marko Burghard, and Klaus Kern. Efficient photothermoelectric conversion in lateral topological insulator heterojunctions. *Nano Letters*, 17(1):214–219, 2017. PMID: 28073269.
 - [79] W. T. Pawlewicz and J A Rayne. No Title. *Physics letters*, (5):48A, 1974.
 - [80] Jae-Hwan Kim, Jung-Yeol Choi, Jae-Man Bae, Min-Young Kim, and Tae-Sung Oh. No Title. *Materials Transactions*, 54(04):618–625, 2013.
 - [81] Yong-qing Li, Ke-hui Wu, Jun-ren Shi, and Xin-cheng Xie. Electron transport properties of three-dimensional topological insulators. *Frontiers of Physics*, 7(2):165–174, 2012.
 - [82] Yuri M Zuev, Jin Seok Lee, Clément Galloy, Hongkun Park, and Philip Kim. Diameter Dependence of the Transport Properties of Antimony Telluride Nanowires. *Nano Letters*, 10(8):3037–3040, 2010.
 - [83] G. Jackeli and G. Khaliullin. Mott insulators in the strong spin-orbit coupling limit: From heisenberg to a quantum compass and kitaev models. *Phys. Rev. Lett.*, 102:017205, Jan 2009.
 - [84] Alexei Kitaev. Anyons in an exactly solved model and beyond. *Annals of Physics*, 321(1):2–111, 2006.
 - [85] K W Plumb, J P Clancy, L J Sandilands, V Vijay Shankar, Y F Hu, K S Burch, Hae-Young Kee, and Young-June Kim. α -rucl 3: A spin-orbit assisted mott insulator on a honeycomb lattice. *Physical Review B*, 90(4):41112, 2014.
 - [86] Stephen M Winter, Alexander A Tsirlin, Maria Daghofer, Jeroen van den Brink, Yogesh Singh, Philipp Gegenwart, and Roser Valenti. Models and Materials for Generalized Kitaev Magnetism. *arXiv preprint arXiv:1706.06113*, 2017.
 - [87] Joji Nasu, Junki Yoshitake, and Yukitoshi Motome. Thermal transport in the kitaev model. *Phys. Rev. Lett.*, 119:127204, Sep 2017.
 - [88] Luke J Sandilands, Yao Tian, Kemp W Plumb, Young-June Kim, and Kenneth S Burch. Scattering Continuum and Possible Fractionalized Excitations in α - RuCl 3. *Physical review letters*, 114(14):147201, 2015.
 - [89] J Nasu, J Knolle, D. L. Kovrizhin, Y Motome, and R Moessner. Fermionic response from fractionalization in an insulating two-dimensional magnet. 12:912, jul 2016.

Bibliography

- [90] Matthias Gohlke, Ruben Verresen, Roderich Moessner, and Frank Pollmann. Dynamics of the kitaev-heisenberg model. *Phys. Rev. Lett.*, 119:157203, Oct 2017.
- [91] M Ziatdinov, Arnab Banerjee, A Maksov, Tom Berlijn, Wu Zhou, H B Cao, J-Q Yan, Craig A Bridges, D G Mandrus, Stephen E Nagler, and Others. Atomic-scale observation of structural and electronic orders in the layered compound α -RuCl₃. *Nature communications*, 7:13774, 2016.
- [92] S-H Baek, S-H Do, K-Y Choi, Y S Kwon, A U B Wolter, S Nishimoto, Jeroen van den Brink, and B Büchner. Observation of a Field-induced Quantum Spin Liquid in α -RuCl₃. *arXiv preprint arXiv:1702.01671*, 2017.
- [93] Daichi Hirobe, Masahiro Sato, Yuki Shiomi, Hidekazu Tanaka, and Eiji Saitoh. Magnetic thermal conductivity far above the néel temperature in the kitaev-magnet candidate α -rucl₃. *Phys. Rev. B*, 95:241112, Jun 2017.
- [94] Heinrich Oppermann, Marcus Schmidt, and Peer Schmidt. Autotransport oder Selbsttransport—Systeme mit Gasphasentransporten unter dem eigenen Zersetzungsdruck. *Zeitschrift für anorganische und allgemeine Chemie*, 631(2-3):197–238, 2005.
- [95] Daniel Weber, Leslie M Schoop, Viola Duppel, Judith M Lippmann, Jürgen Nuss, and Bettina V Lotsch. Magnetic properties of restacked 2D spin 1/2 honeycomb RuCl₃ nanosheets. *Nano letters*, 16(6):3578–3584, 2016.
- [96] Boyi Zhou, Yiping Wang, Gavin B Osterhoudt, Paula Lampen-Kelley, David Mandrus, Rui He, Kenneth S Burch, and Erik A Henriksen. Possible structural transformation and enhanced magnetic fluctuations in exfoliated α -RuCl₃. *Journal of Physics and Chemistry of Solids*, 2018.
- [97] L Binotto, I Pollini, and G Spinolo. Optical and transport properties of the magnetic semiconductor α -RuCl₃. *physica status solidi (b)*, 44(1):245–252, 1971.
- [98] A Little, Liang Wu, P Lampen-Kelley, A Banerjee, S Pantankar, D Rees, C A Bridges, J-Q Yan, D Mandrus, S E Nagler, and Others. Antiferromagnetic resonance and terahertz conductivity in α -RuCl₃. *arXiv preprint arXiv:1704.07357*, 2017.
- [99] Roger D Johnson, S C Williams, A A Haghighirad, J Singleton, V Zapf, P Manuel, I I Mazin, Y Li, H O Jeschke, R Valenti, and Others. Monoclinic crystal structure of α -RuCl₃ and the zigzag antiferromagnetic ground state. *Physical Review B*, 92(23):235119, 2015.
- [100] N. F. Mott. The transition to the metallic state. *The Philosophical Magazine: A Journal of Theoretical Experimental and Applied Physics*, 6(62):287–309, 1961.
- [101] N S Kini, A M Strydom, H S Jeevan, C Geibel, and S Ramakrishnan. Transport and thermal properties of weakly ferromagnetic Sr₂IrO₄. *Journal of Physics: Condensed Matter*, 18(35):8205, 2006.

-
- [102] Marcus Jenderka, José Barzola-Quiquia, Zhipeng Zhang, Heiko Frenzel, Marius Grundmann, and Michael Lorenz. Mott variable-range hopping and weak antilocalization effect in heteroepitaxial Na_2IrO_3 thin films. *Phys. Rev. B*, 88:045111, Jul 2013.
- [103] N F Mott. The effect of electron interaction on variable-range hopping. *Philosophical Magazine*, 34(4):643–645, 1976.
- [104] Pengfa Xu, Jun Lu, Lin Chen, Shuai Yan, Haijuan Meng, Guoqiang Pan, and Jianhua Zhao. Strain-induced high ferromagnetic transition temperature of MnAs epilayer grown on GaAs (110). *Nanoscale Research Letters*, 6:125, 2011.
- [105] A. V. Pogrebnyakov, J. M. Redwing, S. Raghavan, V. Vaithyanathan, D. G. Schlom, S. Y. Xu, Qi Li, D. A. Tenne, A. Soukiassian, X. X. Xi, M. D. Johannes, D. Kasinathan, W. E. Pickett, J. S. Wu, and J. C. H. Spence. Enhancement of the superconducting transition temperature of MgB_2 by a strain-induced bond-stretching mode softening. *Phys. Rev. Lett.*, 93:147006, Sep 2004.
- [106] S-Y Park, S-H Do, K-Y Choi, D Jang, T-H Jang, J Schefer, C-M Wu, J S Gardner, J M S Park, J-H Park, and Others. *arXiv preprint arXiv:1609.05690*.
- [107] S Reschke, F Mayr, Zhe Wang, Seung-Hwan Do, K-Y Choi, and A Loidl. Electronic and phonon excitations in α - RuCl_3 . *arXiv preprint arXiv:1706.02724*, 2017.
- [108] J. Cao, E. Ertekin, V. Srinivasan, W. Fan, S. Huang, H. Zheng, J. W. L. Yim, D. R. Khanal, D. F. Ogletree, J. C. Grossman, and J. Wu. Strain engineering and one-dimensional organization of metal–insulator domains in single-crystal vanadium dioxide beams. *Nature Nanotechnology*, 4(11):732–737, 11 2009.
- [109] Giorgio Bertotti and I. D. Mayergoyz. *The science of hysteresis*. Academic, 2006.
- [110] A. H. Castro Neto, F. Guinea, N. M. R. Peres, K. S. Novoselov, and A. K. Geim. The electronic properties of graphene. *Rev. Mod. Phys.*, 81:109–162, Jan 2009.
- [111] Matthew J. Allen, Vincent C. Tung, and Richard B. Kaner. Honeycomb carbon: A review of graphene. *Chemical Reviews*, 110(1):132–145, 2010. PMID: 19610631.
- [112] M. Rodriguez-Vega, G. Schwiete, J. Sinova, and E. Rossi. Giant edelstein effect in topological-insulator–graphene heterostructures. *Phys. Rev. B*, 96:235419, Dec 2017.
- [113] Lin Du, Tam N. Nguyen, Ari Gilman, André R. Muniz, and Dimitrios Maroudas. Tuning the band structure of graphene nanoribbons through defect-interaction-driven edge patterning. *Phys. Rev. B*, 96:245422, Dec 2017.
- [114] P. L. McEuen, A. Szafer, C. A. Richter, B. W. Alphenaar, J. K. Jain, A. D. Stone, R. G. Wheeler, and R. N. Sacks. New resistivity for high-mobility quantum hall conductors. *Phys. Rev. Lett.*, 64:2062–2065, Apr 1990.

Bibliography

- [115] D. A. Abanin, S. V. Morozov, L. A. Ponomarenko, R. V. Gorbachev, A. S. Mayorov, M. I. Katsnelson, K. Watanabe, T. Taniguchi, K. S. Novoselov, L. S. Levitov, and A. K. Geim. Giant nonlocality near the dirac point in graphene. *Science*, 332(6027):328–330, 2011.
- [116] Peng Wei, Sunwoo Lee, Florian Lemaitre, Lucas Pinel, Davide Cutaia, Wujoon Cha, Ferhat Katmis, Yu Zhu, Donald Heiman, James Hone, Jagadeesh S Moodera, and Ching-Tzu Chen. Strong interfacial exchange field in the graphene/EuS heterostructure. *Nature Materials*, 15:711, mar 2016.

Curriculum Vitae

PERSONAL DETAILS

<i>Name</i>	Soudabeh Mashhadi
<i>Address</i>	Kreuzstr. 9, 70563, Stuttgart, Germany
<i>Phone</i>	(+49) 711-689 1432
<i>Mail</i>	Sh.mashhadi@fkf.mpg.de
<i>Birth</i>	March 1984

EDUCATION

<i>2014-2018</i>	Doctoral Studies (PhD). Ecole Polytechnique Federale de Lausanne, Switzerland. Supervisor: Prof. Klaus Kern
<i>2012-2014</i>	Master of Science. GPA 1.1 . Stuttgart University

PUBLICATION

1. **Electrical Transport Signature of the Magnetic Fluctuation-Structure Relation in α -RuCl₃ Nanoflakes**

Soudabeh Mashhadi, Daniel Weber, Leslie M. Schoop, Armin Schulz, Bettina V. Lotsch, Marko Burghard, and Klaus Kern, Nano Letters **2018** Article ASAP DOI: 10.1021/acs.nanolett.8b00926.

2. **Efficient Photothermoelectric Conversion in Lateral Topological Insulator Heterojunctions**

Soudabeh Mashhadi, Dinh Loc Duong, Marko Burghard, and Klaus Kern, Nano Letters **2017** 17 (1), 214-219 DOI: 10.1021/acs.nanolett.6b03851.

3. **Surface Oxidation Effect on the Electrical Behaviour of Bi₂Te₂Se Nanoplatelets**

Pascal Gehring, Frieder B Reusch, Soudabeh Mashhadi, Marko Burghard and Klaus Kern, Nanotechnology **2016** 28, 285201.